Fall 2007

Self-Organization in Cathode Boundary Layer Discharges

Nobuhiko Takano
Old Dominion University

SELF-ORGANIZATION IN CATHODE BOUNDARY LAYER DISCHARGES

by

Nobuhiko Takano
B.S. March 2000, Kyoto University, Japan
M.S. March 2002, Kyoto University, Japan

A Dissertation Submitted to the Faculty of
Old Dominion University in Partial Fulfillment of the
Requirement for the Degree of

DOCTOR OF PHILOSOPHY

ELECTRICAL ENGINEERING

OLD DOMINION UNIVERSITY
December 2007

Approved by:

_____
Karl H. Schoenbach (Director)

_____
Ravindra P. Joshi (Member)

_____
Kurt Becker (Member)

_____
Hani Elsayed-Ali (Member)

ABSTRACT

SELF-ORGANIZATION IN CATHODE BOUNDARY LAYER DISCHARGES

Nobuhiko Takano
Old Dominion University, 2007
Director: Dr. Karl H. Schoenbach

Cathode boundary layer (CBL) discharge, which has been developed as a UV light source, operates in a direct current between a planar cathode and a ring-shape anode that are separated by a dielectric with an opening of the same diameter as the anode. The nonthermal CBL discharges operate in a medium pressure range down to 30 Torr, emitting excimer radiation when operated with noble gases. The radiant excimer emittance at 172 nm in xenon reaches 1.7 W/cm^2, and a maximum excimer efficiency of 6 % has been obtained. The high excimer radiant emittance, in addition to low cost and simple geometry compared to other UV sources, makes CBL discharges an excellent choice for deep UV lamps and a candidate for integrated flat UV panels (Moselhy *et al.* 2004). It has been found that CBL discharges spontaneously give rise to regularly arranged filaments, i.e., self-organization, at a low current, e.g., less than 0.2 mA at 75 Torr (Schoenbach *et al.* 2004). In this thesis, the self-organization of direct current xenon discharges in the CBL configuration and parallel-plate geometry have been studied for a pressure range from 30 to 140 Torr and currents from 20 μA to 1 mA. Comprehensive examinations have been performed to investigate the behavior of those filaments by the use of optical, electrical, and spectral measurements. Side-on and end-on observations of the discharges have provided information on axial structure and distance of the filaments from the cathode fall. The electrical measurement has recorded a discrete *I-V* characteristic associated with the change of the numbers of the filaments. The spectral

measurement provides scaling information on the relative population of high-lying states ($1s_4$, $1s_5$, and $2p_6$) of excited xenon atoms. Moreover, temperature measurement has revealed that the thermal electron emission from the cathode surface is negligible for the formation of filaments. The reactor geometry with parallel-plate electrodes analogously gives self-organization. The gas species, the cathode material, and the reactor geometry are varied to facilitate the understanding of the CBL xenon discharges and the self-organization. When krypton is used instead of xenon, rather homogeneous plasma far from organized pattern formation is observed with decreasing current. Of the tested aluminum, copper, and tungsten cathodes, the aluminum cathode achieved higher excimer intensity at 250 Torr than that of the molybdenum cathode by a factor of two. The diameter of the plasma reactor was reduced to 300 μm, and it gave rise to a single filament, illuminating with an enhanced excimer power density of 500 mW/cm^2 at 62 Torr. Three mechanisms of these self-organizations are given and discussed in this thesis. The first mechanism explains that the axial electric field can initiate instability. This instability is caused by N-shaped negative differential conductivity (NNDC) in the vicinity of negative glow, which is attributed to electron-electron collisions. Positive feedback of the current density and the electric field due to the NNDC causes fluctuation to develop. Another positive feedback effect of the gas temperature is that the first Townsend coefficient can become dominant as the current density increases. The filaments are assumed to undergo Coulomb force from the positively charged cathode fall channels and positive space charges on the surface of the surrounding dielectric spacer. The calculations, based on these assumptions on the Coulombic interactions, showed good agreement with experimental data. The second mechanism for the pattern formation

is presented as to the development of Turing instability. The discussion is based on the idea that the regular arrangement of filaments is merely a result of general phenomena such as diffusion, ionization, or drift. A reaction-diffusion process with respect to the variation of local current density j and voltage v is the physical effect in the discharge. The numerical calculation was performed and obtained was a 2-D patterned structure exhibiting resemblance to the observed pattern. The transition time to self-organization was calculated to be 6.2 ms. A discussion of the dynamics of the fluctuations and the qualitative explanation for the pattern formation is presented. Benilov's argument (2007) is introduced as the third mechanism. The standpoint of this discussion shows an analogy to that of the second mechanism. The potential distribution behaves as the standing wave described by the Helmholtz equation in the discharge area. In conclusion, applicability of these three mechanisms to self-organization is discussed and compared.

ACKNOWLEDGMENTS

I would like to express my sincere appreciation and gratitude to my advisor, Dr. Karl H. Schoenbach, for his guidance and continuous support of my graduate study. I also thank Dr. Ravindra P. Joshi, Dr. Kurt Becker, and Dr. Hani Elsayed-Ali for thorough consideration of this document.

I want to express my special thanks to Dr. Wei-Dong Zhu and Dr. Shu Xiao for their corrections of this thesis through many readings in their busy days.

I am grateful for valuable discussions with Dr. Jurgen Kolb, Dr. Abdel-Aleam Mohamed, Dr. Mohamed Moselhy, and Dr. Jody White. I also would like to thank Ronald Bentley and Robert Price for their help and cooperation during the course of this dissertation.

I extend many thanks to Barbara Carroll and Ruth Lyman for their help in my study at the Frank Reidy Research Center for Bioelectrics.

Finally, I would like to thank my wife, Kazumi Takano, for her spiritual support and my parents for their belief in me.

TABLE OF CONTENTS

Page

LIST OF FIGURES

Figure Page

CHAPTER I

INTRODUCTION

Cathode boundary layer (CBL) discharges are produced in a reactor consisting of a planar cathode and a circularly opened anode and dielectric. Direct-current operation of the CBL discharges can be sustained over a wide range of pressures up to atmospheric pressure and currents ranging from tens of μA to 20 mA (Moselhy *et al.* 2004). The glow discharge that develops in such a geometry consists of a cathode fall, negative glow, and anode fall, without a positive column. The negative glow serves as a conductor, allowing the radial current to flow to the circular anode. CBL discharges have been developed as a candidate as a VUV light source with a high power density. When operated in a pressure range greater than 75 Torr and at a current of < 0.2 mA in xenon, the discharge appears homogeneous and emits intense excimer radiation with power densities reaching 4 W/cm^2 and efficiencies of approximately 6% and 3% for xenon and argon, respectively (Moselhy *et al.* 2004).

Schoenbach *et al.* (2004) observed spontaneous emergence of self-organized xenon discharge patterns in the CBL configuration by lowering the current density to close to a negative differential conductivity range in the *J*-*V* characteristic where *J* is the largest current density in a discharge and *V* is the sustaining voltage across electrodes. These patterns consist of a number of filaments regularly distributed on the cathode surface in a variety of geometric arrangements dependent on the pressure and the operating current. The patterning is considered to be unique with respect to the following

---

The format of *Journal of Physics D: Applied Physics* is used in this thesis.

three points:1) Filaments are stably arranged perpendicular to the cathode surface. 2) They are observed in an electrode geometry with a conductive cathode while a semiconductor cathode is often used for self-organization (Gurevich *et al.* 2005). 3) The discharge runs in dc voltage while other reported patterns are typically in dielectric barrier discharges using alternating current power (Muller 2004, Strümpel *et al.* 2001, Shirafuji *et al.* 2003).

A few papers have presented mechanisms for the self-organization in the CBL discharges. Glow-to-arc transition, which is a positive feedback of cathode temperature and secondary emission of electrons, results in contraction of the plasma column. A number of filaments may be observed due to this effect in parallel-plate geometry (Raizer 1991). In the case of CBL discharges, it was assumed that the cathode temperature, which determines the secondary Townsend coefficient, may play an important role in forming self-organization (Schoenbach *et al.* 2004). The assumption posits that glow-to-arc transition decreases the sustaining voltage, and successive heat conduction through the cathode can create another branch in a characteristic of the sustaining voltage with respect to the current density. Therefore, the experiment reported in this thesis shall assess the role of cathode temperature.

Benilov (2007) presents another view of self-organization. The author argues that the self-organization can be similarly explained using the theory that accounts for cathode spots in high-pressure arc discharges (Benilov 1988). The self-organization is attributed to an "N-shaped nonlinear relation" of the current density and the sustaining voltage, which is later referred to as having an S-shaped negative differential conductivity in this thesis. In this situation, multiple states with a negative slope in the j-v curve, where j is

the local current density and υ is the local sustaining voltage, are present in a three-dimensional system as a derivation of a one-dimensional solution. In the framework of this principle, the potential distribution exhibiting a standing wave can be allowed. The discussion derives solutions to the Helmholtz equation with respect to spatial distribution of potential perturbation, resulting in axisymmetric spots on the cathode by means of implementing two-dimensional computations.

In addition to existing explanations for self-organization in CBL discharges, other effects related to instability of the plasmas may be closely related to the self-organization as a possible mechanism. An oscillatory instability due to a drop of drift velocity with an increased *E/N* (the reduced electric field where *N* is the gas density) is known to exist by a number of experiments (Pack and Phelps 1961, Pack *et al.* 1962, and Haddad 1983). Aleksandrov *et al.* (1997) have proposed that the effect can also occur in xenon via elastic or inelastic electronic collisions with increasing *E*/*N*. The negative differential conductivity as a result of the collisional process is considered to occur in negative glow or Aston dark space.

In order to explore the mechanism of self-organization in CBL discharges, which was only observed in xenon, not in argon (Schoenbach *et al.* 2004) or krypton, the CBL discharges have been experimentally studied in the pressure range from 30 to 140 Torr, at low currents (< 1 mA). In addition to end-on observations, the discharge was observed side-on through a transparent dielectric spacer. This has allowed us to measure the cathode fall length. The information provides data on the secondary emission coefficient as well as the cathode fall voltage in these discharges. A subsequent temperature measurement on the back of the cathode surface gives the effect of the temperature on the

second Townsend coefficient. The size of the anode opening is varied, and the behavior of single-filament self-organization is investigated in the visible and the VUV. This experiment is aimed at an optimal design for a high-efficiency excimer light source. Spectral measurements can offer information on important plasma parameters which might affect the self-organization. For instance, the rotational temperature of the nitrogen in the luminous area can be calculated when a range of spectra is measured with nitrogen added as a probing gas. The use of hydrogen as a probing gas is also assumed for measuring Stark broadening of spectral lines to obtain values of the electron density. Absorption spectroscopy at 823 or 828 nm is widely used to calculate the population of excited atoms at high-lying states ($1s_4$ or $1s_5$) (Tachibana *et al.* 2000, Shintani *et al.* 2003). Knowing the population of excited atoms at $1s_4$ and $1s_5$ would allow us to estimate the production rate for excimers of the discharge. This could be critically important if the discharge drives an instability that is related to the excitation level. Unfortunately, in our case nitrogen cannot be added as a probing gas, for it immediately quenches self-organization when added. Furthermore, the shortness of optical path length (~100 μm) prevents absorption spectroscopy. Therefore, only optical emission spectroscopy (OES) is adopted in the experimental apparatus and conducted from VUV to NIR. The measurements from the VUV to NIR allow us to have a qualitative insight into the population of xenon atoms in excited states, Xe^{**} and Xe^{*}, respectively. A classical geometry of the plasma reactor, i.e., parallel-plane geometry, has been tested. This experiment enables the diagnosis of the importance of radial electric field for filament formation.

Three approaches to explain the mechanisms of the self-organization are discussed. One incorporates subsequent physical effects as the current is decreased. The fluctuations are initiated due to negative differential conductivity that is caused by the elastic collisions between electrons and neutral atoms. In the region where current density is concentrated due to the fluctuations, the current density undergoes a positive feedback that reproduces more charge carriers in the space because of the increase of the first Townsend coefficient. The regular formation of the patterns is attributed to the Coulombic repulsive force in the cathode fall region.

In another approach, a mathematical derivation and a numerical simulation are performed to understand the relationship between the derivative of local current density, j, and the voltage, v. The physical effects taken into consideration are a nonlinear relationship of j to v created by changes in the relationship of the first Townsend coefficient α to the electric field E, and transport (diffusion and drift) of charged particles parallel to the cathode surface. Due to the nonlinearity, small fluctuations develop via inhomogeneous production of j synchronized with transport. The resultant equations have a form of reaction-diffusion equations with a nonlinear term describing negative differential conductivity with respect to j and v. The analysis of these equations indicates that the competition of j and v creates pattern formation. The results of the numerical simulation are also shown and compared with the experimental results. In addition, linearization of the governing equations gives the wave number of this instability, and the time for formation of the self-organization in xenon is calculated.

Finally, the third option, leading to the Helmholtz equation, is introduced and evaluated. The discussion focuses on the difference between this approach and others

from the standpoint of what kind of specific effect causes the self-organization. The peculiarities of the solutions to the governing equation are compared with the experimental results with respect to arrangements of the filaments.

From an industrial point of view, the self-organization may offer an application as a VUV light source. The cathode material or the dimension of the plasma reactor should be optimized for the best operation. The device enhances the excimer radiation in the normal glow, including self-organization, compared to the abnormal regime. The mechanism for the maximum excimer intensity at a low current regime is attributed to the change of rate coefficients due to the variation in mean electron energy. A qualitative explanation is given to support this hypothesis.

Chapter 2 of the thesis describes the background of dc discharges in a parallel-plate configuration with a wide range of currents from Townsend-to-normal glow transition to glow-to-arc transition. CBL discharges are then compared with general discharges in parallel-plate geometry with respect to operating current range. In addition, other remarkable aspects of the CBL discharges, appearances and excimer performance found in past studies, are reviewed. Chapter 3 discusses representative instabilities that are thought to be crucial for pattern formation in dc discharges. Self-organized patterns observed in a variety of gas discharge systems are introduced, and their mechanisms are discussed in chapter 4. The diagnostic methods used in the experiments for this thesis are explained in chapter 5. Chapter 6 presents experimental results of a variety of measurements: electrical, optical, temperature and spectroscopic measurements. The secondary Townsend coefficient is derived for the CBL discharges, and a discussion of the enhanced excimer radiation in low current operation appears in chapter 7.

Furthermore, three mechanisms leading to the self-organization and the pattern structures are discussed.

CHAPTER II

BACKGROUND

2.1 DC GAS DISCHARGES

A gas in its normal state is an almost perfect insulator. However, when a sufficiently high voltage is applied between two electrodes placed in a low pressure gaseous environment, atoms and molecules of the gas will break down electrically, generating electron-ion pairs. This permits current to flow through the gas medium, enabling the gas to become a conductor. This phenomenon is called an "electrical discharge." Electrical discharges are subdivided on the basis of their current-voltage characteristics. Figure 2.1 (Francis 1956) shows the subdivision into the most common types of electrical discharges as a function of their current.

2.1.1 Photocurrent regime

For the onset of discharges, free electrons are required to exist in the vessel and must be accelerated by the uniform external electric field. The rate of generation of free electrons can be enhanced if the cathode is illuminated by ultra violet (UV) light. A somewhat higher steady current, of about 10^{-12} or 10^{-13} A, would be observed in this regime. The photoelectric current gives rise to more electrons, resulting in more electron multiplication and, hence, in a higher current. Thus, the characteristics of I and V exhibit a positive slope, as presented in region AB in figure 2.1. This phenomenon is a non-self-sustained discharge.

2.1.2 Townsend discharge

At very small currents (a few μA or less) the space charge holds such a small value that it causes little spatial distortion of the external electric field. The discharge

occupies the whole electrode surface. Such a discharge is called a Townsend discharge, and this regime is located in the segment BC in figure 2.1. The discharge does not appreciably glow, due to sparse ionization, so it is not a type of glow discharge. Because the sustaining voltage V is independent of the discharge current, V is equal to the breakdown voltage V_t.

2.1.3 Transition from Townsend discharge to normal glow

As the current density gradually increases, distortion of the electric field due to space charge becomes pronounced. The discharge may undergo radial contraction at this stage. The slope of the voltage-current characteristic in this regime is negative (causing instabilities). This is called a subnormal discharge and represented by CD in figure 2.1. In this regime, the loss of electrons by diffusion is considered to play a major role (Kolobov 1994) in determining the radius of the discharge. Because the diffusion of the electrons parallel to the cathode surface causes a loss for multiplication, the sustaining voltage is still found to be not the minimum. This subnormal discharge regime is known to accompany no radial constriction of light emission if the product of the pressure p and the interelectrode distance L is low enough. The criterion is $pL < (pL)_{pm}$ where $(pL)_{pm}$ represents the pL at Paschen's minimum (Kolobov 1991). The relation $pL < (pL)_{pm}$ is satisfied if the discharge is on the left branch of the Paschen's curve (Elemeus *et al.* 1974, Melekhin *et al.* 1987). No systematic investigation of the radial shape of the discharge in the subnormal glow has been published (Kolobov 1994).

Townsend-to-glow transition is considered to arise from an abrupt increase of impact ionization, as increasing the electric field due to nonlinearity of the first Townsend coefficient, α (Sicavic 2003). This regime constitutes an S-shaped *I-V*

characteristic. In a Townsend discharge, the discharge is sustained by applying the voltage equal to the ignition potential V_t. The electric field E is uniformly distributed and evaluated as $E_t = V_t/L$, where L is the interelectrode distance. When the current is increased, the charge buildup is no longer negligible. The distortion of the electric field between the cathode and anode is observed due to the space charge as shown in figure 2.3. The spatial distribution of the electric field due to charge buildup contains regions where $E > E_t$ near the cathode and $E < E_t$ near the anode. The decrease of the sustaining voltage caused by the charge buildup is due to the nonlinearity of the first Townsend coefficient $\alpha(E)$ as

$$\alpha = Ap \exp(-Bp/E), \tag{2.1}$$

where A and B are constants, p is the pressure and E is the local electric field. The diagram of α versus E has an inflection point where $d^2\alpha/dE^2 = 0$ where the electric field is $E_{critical} = Bp/2$ as shown in figure 2.3. From now on, we consider the case of $E_t < E_{critical} = Bp/2$, where the critical electric field E_t for the Townsend discharge is less than the electric field of the inflection point. The following conservation law must be satisfied for any self-sustainable discharge:

$$\gamma\left[\exp\int_0^L \alpha dx - 1\right] = 1 \tag{2.2}$$

where γ is the secondary Townsend coefficient. When a small amount of ionization is taking place, separation of charged particles creates two regions in space where $E > E_t$ and $E < E_t$. The former region contributes to multiplication of ion-electron pairs, where $E < E_t$ impedes it, while satisfying equation 2.2. The absolute voltage increase $|V_A|$ in figure 2.3 is smaller than the absolute voltage decrease $|V_B|$, but equation 2.2 is still satisfied

because the increase of α in the region A is significant even with a small increase of E because of the nonlinearity of $\alpha(E)$. When expanded to the second order, a_2 is found to be positive where $\alpha = a_0 + a_1 E + a_2 E^2$. Thus, the third term on the right hand side of the equation contributes to the increase of α. On the other hand, the decrease of α is mild in region B because the third term is negative in region B. Thus, a large drop of the potential is possible to cancel out the excess amount of ionization made in region A. Thus, the integration of the electric field from $x = 0$ to $x = L$ is found to be less than the voltage V_t. Consequently, an NDC of I-V characteristic is obtained.

2.1.4 Normal glow discharge

When the current density reaches a certain value, the discharge begins to spread radially again. This is known as the normal discharge as denoted by DE in figure 2.1 and characterized by a constant voltage. The sustaining voltage, V, also retains its minimum value, V_{min}, and provides the most effective reproduction of ion-electron pairs among four regimes: Townsend, subnormal, normal, and abnormal glow.

2.1.5 Abnormal glow discharge

When the current is further increased, the abnormal glow discharge (EF in figure 2.1) follows the normal discharge, occupying the entire area of the cathode. The voltage then starts to rise again with increasing current, and luminosity is enhanced because of more energetic reaction processes. The reason for the monotonic relation of the voltage to the current in the abnormal glow is attributed to the contribution of the nonlinearity of α as was explained in section 2.1.4. In the phase of the transition from Townsend discharge to normal glow, space charges start to accumulate in the cathode fall. The sustaining voltage decreases with a concentration of positive charges in the vicinity of the cathode.

However, there is a limit to the decrease in the voltage because of the boundedness of α (when α is bounded, α does not exceed a certain value no matter how large E is). The region near the cathode fall has such a large electric field that α becomes insensitive to E as shown in figure 2.2. As a result, further distortion of the distribution of the electric field does not contribute to an increase of ionization. Therefore, a higher electric field needs to be applied from the external source to increase the rate of ionization. This regime exhibits an increasing characteristic of V versus I, which is called abnormal glow.

2.1.6 Glow-to-arc transition

As the current density increases in the abnormal region, the sustaining voltage increases as well. Given more kinetic energy by the higher electric field, the positive ions can release more energy when impinging on the cathode surface. This raises the temperature of the cathode, and for refractory materials such as carbon and tungsten, the temperature of the cathode will become sufficiently high for thermionic emission to occur, e.g., at ~2000 K in the case of tungsten (Wehrli 1928). The increased electrons emitted from the thermionic cathode produce more positive ions in the cathode fall region due to electrical avalanche (FG in figure 2.1). In this case, the sustaining voltage necessary to maintain the current is found to be lower than that in abnormal glow because secondary effects to be sustained by high electric field are no longer necessary with the presence of the hot cathode. In experiments, the transition takes place rapidly, turning into arc with a current of nearly 1 A and a voltage of tens of volts.

A. von Engel (1924) formulated the relation of the secondary effect, including thermal effect at the cathode surface, to the total current density. At the cathode surface

where z = 0, the following equation is satisfied as to the electron current density, $J_{-}(0)$, and the ion current density, $J_{+}(0)$,:

$$J_{-}(0) = \gamma J_{+}(0) . \tag{2.3}$$

When taking into consideration the thermal emission of electrons from the cathode surface, the thermal electron emission current density, J_t, is calculated by the means of Richardson's law,

$$J_t = aT^2 \exp(-b/T) \tag{2.4}$$

where T is the temperature at the cathode surface and a and b are constants dependent on the electrode material. The total current density, J, is then evaluated as

$$J = J_{-}(0) + J_{+}(0) = (1+\gamma)J_{+}(0) + J_t . \tag{2.5}$$

The effective secondary Townsend coefficient $\gamma' = J_{-}/J_{+}$ is defined as

$$\gamma' = \gamma + \frac{1+\gamma}{(J/J_t - 1)} . \tag{2.6}$$

There is a recent model on self-organization in CBL discharges, accounting for the existence of branches of *V*-*J* characteristic instead of resistive abnormal glow due to abnormal-to-glow transition (Schoenbach *et al.* 2004). In this regime, the effective secondary emission coefficient, γ', is given by equation 2.6. The cathode temperature in this model is set to be uniformly distributed in the radial direction and determined by the hypothesis that the entire electrical power in the cathode fall is converted into blackbody radiation from the cathode surface with heat conduction,

$$JV_c = \sigma T^4 - k\frac{(T_c - T_{oc})}{d_c} , \tag{2.7}$$

where σ (5.7×10^{-12} W/(K^2 cm^2)) is the radiation constant, k is the heat conduction constant, d_c is the thickness of the cathode, T_c is the temperature at the cathode surface, and T_{oc} is the temperature of the opposite side of the cathode. The model predicts a transition from glow to arc at currents over 5 A/cm^2 at individual filaments with a temperature of the cathode comparable to the melting point of the cathode material (~2893K for molybdenum).

In cylindrical geometries, contraction, self-compression of a positive column, is typically observed during the mode from glow to arc. The instantaneous phenomenon accompanies one or several bright current filaments. This instability is undesirable because it increases the gas temperature away from equilibrium. The sudden drop of sustaining voltage takes place along with an increase of gas temperature and electron density. Another distinction of contraction is characterized by an abrupt increase in the degree of ionization, by nearly two orders of magnitude, due to the increase of the electron density inside the contracted current path (Raizer 1991).

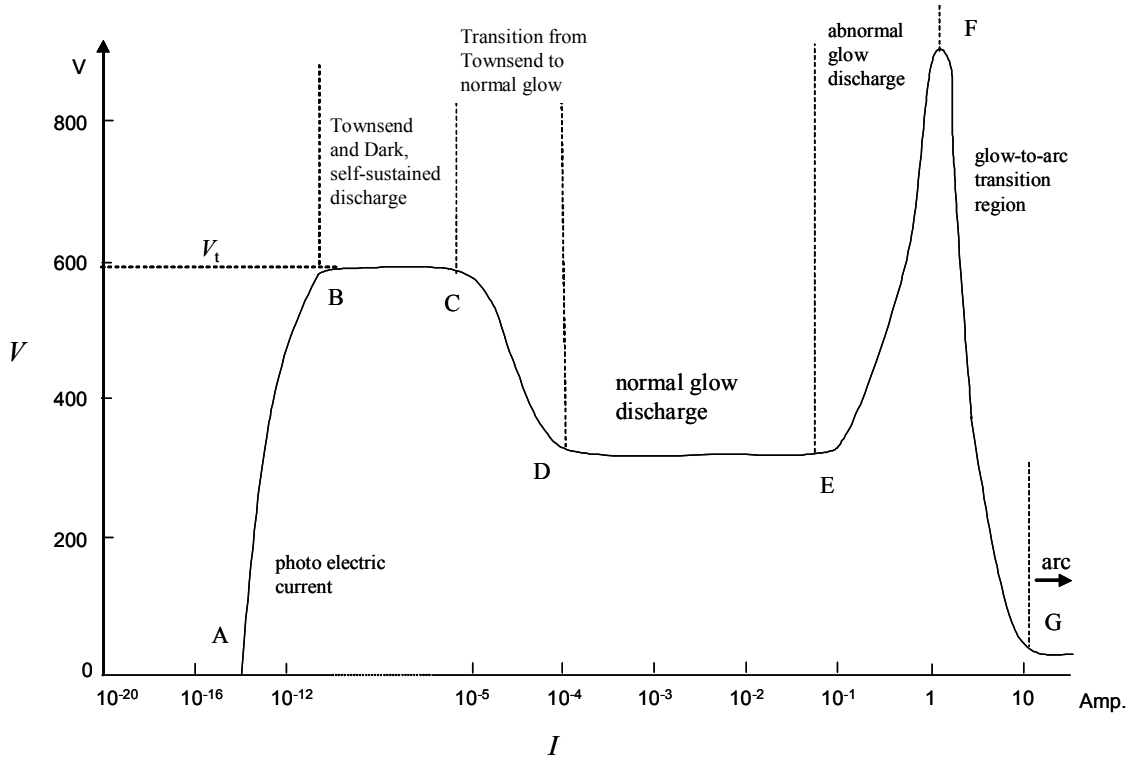

Figure 2.1. A diagram of a typical discharge to arc in a dc operation.

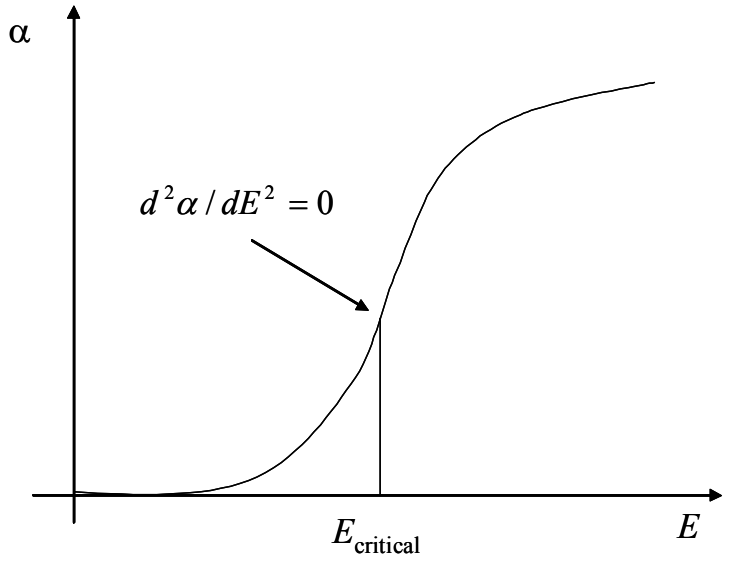

Figure 2.2. A qualitative relation of α to E. At E_{critical}, the curvature of $\alpha(E)$ changes (A. von Engel 1924).

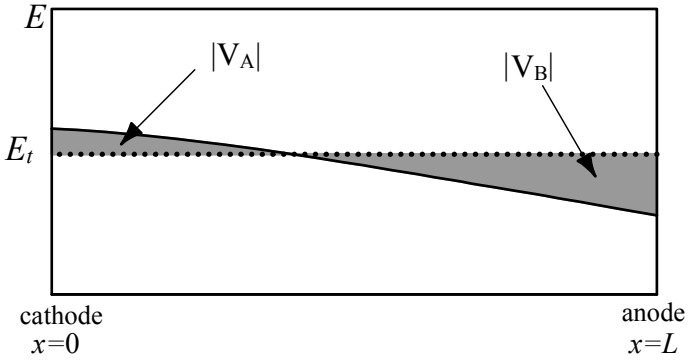

Figure 2.3. An illustrative diagram of an electric field distribution from the cathode (x = 0) to the anode ($x = L$) where the space charges are not sufficient for normal glow (Raizer 1991).

2.2 MICRODISCHARGES

Recently, there is much interest in the reduced size of glow discharges. Microdischarges or microplasmas, which are under millimeter scales (Becker *et al.* 2006), are expected to pioneer a new realm of plasma science. Integration of microdischarges is one of the promising applications, offering a large market area, as lately seen in plasma display panels. In addition, the potential of the microdischarges has been expanded to environmental applications (Becker *et al.* 2005) or light detection devices (Eden *et al.* 2004) with flexible dimensions of the plasmas. Development of microplasmas as a VUV light source has also attracted increasing interest (Moselhy *et al.* 2004), aiming at versatile applications such as lithography. In spite of this recent attention, the number of diagnostics to expand the understanding of microdischarges is limited due to their small size. More intensive and varied diagnostics need to be found.

2.3 A VARIETY OF GEOMETRIES OF MICRODISCHARGES

Microdischarges with a low ion/neutral temperature (cold plasmas) are operated in various reactor configurations. Microhollow cathode (MHC), capillary plasma electrode (CPE), and cathode boundary layer (CBL) discharges represent successful geometries with advantages over the conventional parallel-plate geometry. The reactor of MHC discharges incorporates an opening in the cathode with a typical diameter of the hollow part from 10 to 500 μm (El-Habachi *et al.* 1997, Moselhy *et al.* 2001). The geometry is derived from that of the well-known low-pressure hollow cathode (HC) discharges. The CPE discharges use electrodes covered by perforated dielectrics (Kunhardt *et al.* 1999), which differentiate them from dielectric barrier discharges (DBDs). When a gas flow is implemented, the CPE discharges present a characteristic jet

which emerges from the end of the capillary. This type of discharge is frequently operated by ac power.

2.4 CATHODE BOUNDARY LAYER DISCHARGES

The cathode boundary layer (CBL) discharges are produced by a CBL electrode system that has a significant difference from parallel-plane geometries; the CBL configuration has an open anode. The electrode geometry consists of a planar cathode and an anode with a circular opening having a diameter of up to 5 mm as shown in figure 2.4 (Shi and Schoenbach 1999). The cathode and anode are separated by a thin dielectric layer with the same opening geometry as the anode. The thickness of the dielectric layer varies between 100 and 500 μm. The glow discharge that develops in such a geometry has a structure consisting of a cathode fall, negative glow, and anode fall, without a positive column. The negative glow serves as a conductor, providing a path for the radial current flow to the circular anode (Schoenbach *et al.* 2004). With all the characteristic features, CBL discharges qualitatively have the same phases – Townsend discharge to arc discharge as described in section 2.1. Generally, CBL discharges stably operate in the positive slope of the *I-V* characteristics in abnormal mode with a typical current of tens of μA to 20 mA and a pressure range from 75 to 760 Torr as shown in figure 2.5 (Moselhy and Schoenbach 2004). Clearly, parallel operation of these discharges is feasible without individual ballast resistors. This has been demonstrated by Frame and Eden (1998) with arrays of microplasma devices with the structure described above. Zhu *et al.* (2007) successfully conducted an experiment of parallel operation of CBL discharges in xenon.

The radiant excimer emittance at 172 nm increases with pressure and reaches a value of 4 W/cm^2 for atmospheric pressure operation in xenon (Moselhy and Schoenbach

2004). The maximum internal efficiency, however, decreases with pressure having highest values of 5% for 75 Torr operation. As was observed with xenon, the radiant emittance of argon increases with pressure, and the efficiency decreases. The maximum radiant emittance is 1.6 W/cm^2 for argon at 600 Torr. The maximum internal efficiency is 2.5% at 200 Torr.

Spontaneous emergence of self-organized patterns of xenon plasma has been observed in a CBL configuration by lowering the current density with a measured pressure condition below 760 Torr (Schoenbach *et al.*. 2004). The point symmetric pattern consists of a number of filaments regularly distributed on the cathode surface, and the arrangements have variations depending on the pressure and the operating current. As the pictures in the visible and the vacuum ultraviolet (VUV) are shown in figures 2.6(a) and (b), respectively, one can find a simple principle: the number of the filaments is larger when the current and pressure are greater. The VUV radiation at 172 nm from excimers in the self-organized filaments provides higher optical power (figure 2.6(b)). The mechanism for this effect needs to be explained. Discharges in argon with the same configuration of the plasma reactor do not give self-organization.

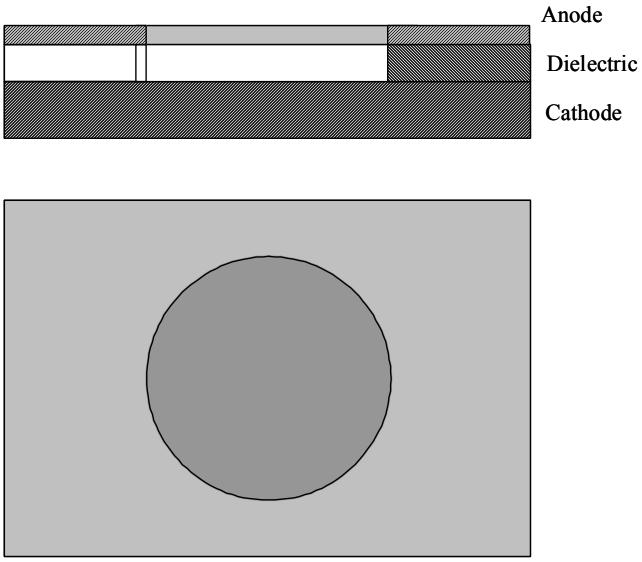

Figure 2.4. A side-on view (top) and end-on view (bottom) of a typical CBL configuration.

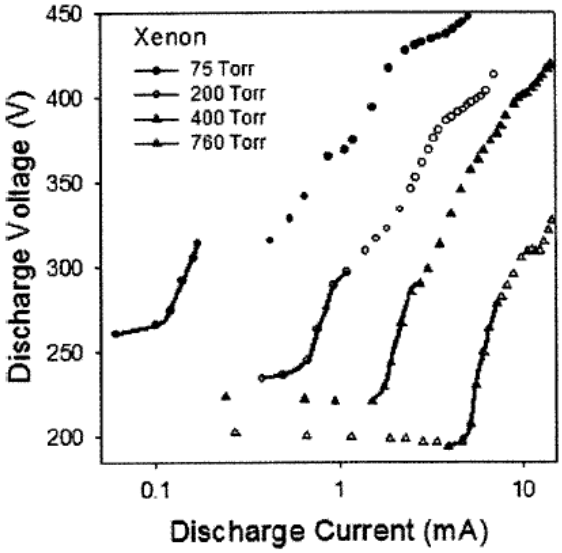

Figure 2.5. *I-V* characteristics of the CBL discharges are plotted with emphases of the rages with self-organization denoted by solid lines. The pressure range is 75 to 760 Torr (Moselhy *et al.* 2004).

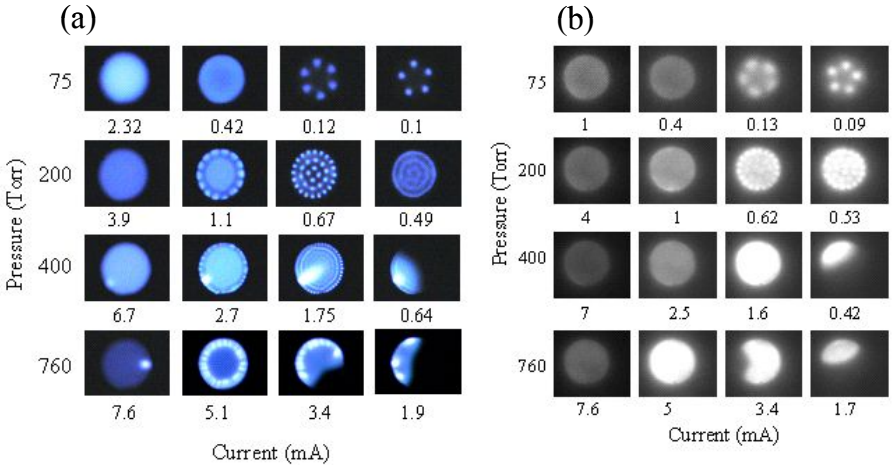

Figure 2.6. Self-organization (a) in the visible and (b) in the vacuum ultraviolet (VUV) (Schoenbach *et al.* 2004).

CHAPTER III

INSTABILITIES IN DC GLOW DISCHARGES

Instabilities in dc glow discharges arise from plasmas in various conditions in terms of volume, pressure, current, electron temperature, or gas temperature. Depending on the type of instability, the state of the plasma can be greatly altered, e.g., contraction of the plasma or striation. Regular pattern formation lateral to the current flow is also considered a particular result of an instability. In order to know what instability may cause pattern formation in CBL discharges, it is necessary to compare the reasons and results of instabilities to observed phenomena in CBL discharges. Hence, this chapter gives an overview of representative instabilities in dc glow discharges to give insight on possible instabilities in CBL discharges.

We can, in principle, group instabilities into two types: electronic and thermal. Electronic instability causes runaway ionization leading to constriction of the plasma column due to a positive feedback between the electron energy distribution and N^*, the density population of excited states (Haas 1973). An example of this type of instability is the attachment-induced instability that occurs in gas mixtures containing an electronegative gas such as O_2 (Nigham *et al.* 1974). Thermal instabilities are associated with changes in the gas density N due to heating of the neutral component. Such instabilities are explained in more detail in the following sections.

Instabilities often accompany negative differential conductivity (NDC) on account of a variety of mechanisms, such as thermal effects or the difference of inelastic collision frequency of electrons. The function of NDCs is significantly related to the catastrophic

growth of the instabilities. This chapter will provide comprehensive characteristics and mechanisms of such instabilities with an emphasis on NDCs.

3.1 THERMAL INSTABILITY

Gas heating has been known to be a destabilizing factor. It results in discharge contraction or formation of filaments in which the degree of ionization and the gas temperature are found to be much higher than ordinary glow discharges. The consequence is typically seen as a runaway from the preceding stable equilibrium. The instability develops from transverse inhomogeneities whose direction is perpendicular to the current flow. The causality of thermal instability is reflected in the following closed chain of links, and it can be initiated at any step (Raizer 1991):

$$\delta(n_e)\uparrow \Rightarrow \delta(jE)\uparrow \Rightarrow \delta T\uparrow \Rightarrow \delta N\downarrow \Rightarrow \delta(E/N)\uparrow \Rightarrow \delta(T_e)\uparrow \Rightarrow \delta(n_e)\uparrow, \qquad (3.1)$$

where upward (downward) directed arrows symbolize an increase (decrease) in a quantity. As the pressure of the gas levels off quickly, thermal expansion occurs, accompanied by a drop in the gas density. In molecular gas discharges, a significant amount of energy flow is made via vibrational states of the molecules (Bouef *et al.* 1986). Subsequently, the electron distribution function is shifted to the tail due to increased local *E*/*N*. This is followed by an increased ionization rate, α, resulting in an increase of the electron density.

3.2 ELECTRONIC INSTABILITY

In this type of instability, the electron energy distribution and N^* play an important role with *N* remaining constant as opposed to the case of thermal instability. We take two examples of such instability, multistage ionization instability and inelastic or elastic collisions causing a drop in electron drift velocity.

3.2.1 Instability due to stepwise ionization

This instability can result from a balance between ionization and electron-ion recombination. This instability is triggered when ionization and excitation have a strong dependence on the electron temperature, which is determined by the local electric field. Therefore, a small perturbation of the local electric field can cause concomitant changes in the electron density and density of excited states. Both changes accelerate or decelerate further production of electrons, leading to constriction of the plasma. The kinetic equations with respect to electrons and the excited states are written as follows (Raizer 1991):

$$\frac{dn_e}{dt} = k_i N n_e + k_i^* N^* n_e - \nu_{da} n_e, \qquad k_i = k_i(T_e) \tag{3.2}$$

$$\frac{dN^*}{dt} = k^* N n_e - k_2 N^* n_e - \nu_d^* N^*, \qquad k^* = k^*(T_e). \tag{3.3}$$

Here $k_i = \nu_i/N$, $k^* = \nu^*/N$ are the rates of ionization and excitation of atoms from the ground states, k_i^* and k_2 are the rates of ionization and deexcitation of excited metastable atoms, and ν_d^* is the frequency of losses of excited atoms not caused by electron impact. ν_{da} stands for the rate of diffusional loss of electrons. Equation 3.2 takes into account that $k_i^* << k_2$ because an electron needs sufficient energy for ionization but does not need it for deactivation. If the instability develops more slowly than the excited atoms decay, the density N^*, being quasisteady, tracks the growth of n_e:

$$N^* \approx N^*[n_e(t)] \approx k^* N n_e / (k_2 n_e + \nu_d^*). \tag{3.4}$$

Taking the variations of equations 3.2 and 3.4 at the steady-sate point and neglecting the dependence of k_i^* and k_2 on T_e in comparison with that of k_i and k^*, we obtain the growth rate, with an assumption $n_e \propto \exp(\Omega t)$,

$$\Omega = \frac{v_d^* k_i^* N^{*2}}{v^* n_e} + \frac{\delta \ln T_e}{\delta \ln n_e}(\hat{v}_i v_i + \hat{v}^* k_i^* N^*) \tag{3.5}$$

where $\hat{v}_i = d(\ln v_i)/d(\ln T_e)$. Although the two terms can be positive, it is found in the first term that the growth rate is strongly affected by the density of the excited states N^*. Stepwise ionization is known to be essential for formation of striation in the positive column as a result of longitudinal instability (Kolobov 2006), which develops and forms striations perpendicular to the current flow. The instability propagates in the medium along the electric field as a wave, i.e., ionization wave at the ion acoustic speed. The wavelength of ionization waves is typically up to tens of centimeters, and their frequency does not exceed tens of kilohertz (Golubovskii *et al.* 1963).

3.2.2 Inelastic or elastic collisions

A drop in electron drift velocity, *w*, as a function of *E*/*N*, defined as an N-shaped NDC (NNDC), has been extensively investigated especially in semiconductor physics. A good representative example would be the Gunn-effect in bulk III-V semiconductors. The NDC results in an oscillation of current or domain formation. This effect is caused by electron collisions occupying another upper conduction band valley, increasing the effective mass of electrons, and showing a decrease in electron mobility (Shaw *et al.* 1979).

In dc gas discharges, the drop of *w* with increasing *E/N* has been observed in specific gases such as CH_4 (Pack and Phelps 1961) or N_2 (Kleban and Davis 1977). Gunn-like instability is observed in an externally sustained discharge in mixtures of N_2 and CO with argon (Lopantseva *et al.* 1979) where an NNDC occurs. NNDC can be observed in argon with a dilute mixture of molecular gas. This was initially proposed

theoretically (Long *et al.* 1976) and experimentally proved (Haddad 1983). For inert gases, Robertson (1977) demonstrated experimentally that NNDC is not present. However, measurements of electron drift velocities are typically conducted using photocurrent (Hornbeck 1951) where electron-electron collisions are neglected. Recently there have been several theoretical predictions proposing the existence of NNDC in rare gases if an adequate level of ionizations is provided (Aleksandrov 1996, 1997; Kochetov *et al.* 1998).

The occurrence of the drop in w with increasing E/N in gas discharges has been elucidated by a number of theories in terms of the special features of the elastic and inelastic collision cross sections of the electron. There are two rough classifications of classic mainstreams. Kleban and Davis (1977) explained that NNDC can occur when an increase in E/N leads to an abnormally large increase in the elastic collision frequency. Then, the enhanced randomization of the directions of the velocity vectors can decrease the drift velocity even though the mean electron energy increases. The degree of anisotropy therefore plays a principal role in determining the drift velocity. On the other hand, Long *et al.* (1976) base their argument only on the variation of momentum transfer frequency $\langle \nu_m \rangle$ versus E/N. A Ramsauer-Townsend minimum is also considered to contribute to the presence of NNDC in both arguments. Petrovic (1997), however, has conducted calculations and showed that it is not a necessary condition.

Another mechanism for NNDCs in pure rare gases has been numerically predicted (Aleksandrov *et al.* 1996). On the basis of an analytical treatment of the Boltzmann equation, it has been shown that a constraint with respect to collision frequency for e-e collisions is required for displaying NNDC (Chiflikyan 2000). The treatment by

Aleksandrov *et al.* takes into account electron-electron collisions in addition to inelastic collisions. The drift velocity of the electron, *w*, can be calculated by solving the Boltzmann equation, with the two-term expansion of the electron distribution function in Legendre polynomials (Huxley *et al.* 1974), as

$$w = -\frac{eE}{3N}\left(\frac{2}{m}\right)^{1/2}\int_0^\infty \frac{\varepsilon}{\sigma_m}\frac{\partial f_0}{\partial \varepsilon}d\varepsilon \tag{3.6}$$

where *e* and *m* are the electron charge and mass, respectively, σ_m is the electron-atom collision cross section for the momentum transfer, $f_0(\varepsilon)$ is the isotropic component of the electron energy distribution function (EEDF). The processes taken into consideration in this equation are e-e collisions, the elastic electron-atom scatterings, and the direct and stepwise excitations and ionizations. The e-e collisions do not cause loss of electron energy, nor do they change the anisotropy. The e-e collisions, however, exert an influence on the shape of EEDF, as in figure 3.1 where electron energy distribution functions versus electron energy is plotted. For example, a comparison between the solid line 1 ($\alpha = 0$) and 3 ($\alpha = 10^{-5}$) demonstrates the effect of e-e collisions on the distribution of electron energy. Here, α is the degree of ionization $\alpha = n_e/N$ and δ the fraction of excited states $\delta = N^*/N$. Given zero ionization level ($\alpha = 0$), i.e., no e-e collisions taking place, the EEDF results in a plateau at low-energy levels $\varepsilon < 1$ eV (solid line 1). On the other hand, low energy electrons can be richer in number with an elevated ionization level ($\alpha = 10^{-5}$), attaining ~1 $eV^{-3/2}$ (solid line 3). As shown by solid line 3, the slow electrons (< 1 eV) occupying a large portion with respect to distribution are more likely to undergo momentum transfer with neutral particles than fast electrons. The resulting energy transfer is greater than that of a lower density for slow electrons (see solid line 1

in figure 3.1). Figure 3.2 shows the calculated electron drift velocity versus E/N for pure xenon (Aleksandrov 1996). Several sets of the results are given for the degree of ionization α and the fraction of excited states δ. The results of the calculation of equation 3.6, taking into consideration e-e and e-i collisions, showed that a certain range of ionization rate, α, is necessary for the manifestation of NNDC. Frequent excitations of xenon from ground state to the first excited state can strongly affect the w-E/N characteristic, in favor of NDC; a comparison is made in curves 2 and 4 (figure 3.2).

The nonlinear relation of w to E/N is the cause of spontaneous oscillations of current and voltage in externally sustained dc gas discharges, for instance, in mixtures of N_2 and CO with argon (Lopantseva *et al.* 1979). In a weak E/N on the order of 10^{-16}Vcm^2, the perturbation has a period of ~$1/w$ where w is on the order of 10^5 cm/sec. This suggests that it may be exploited to develop an rf source (by analogy with the Gunn effect).

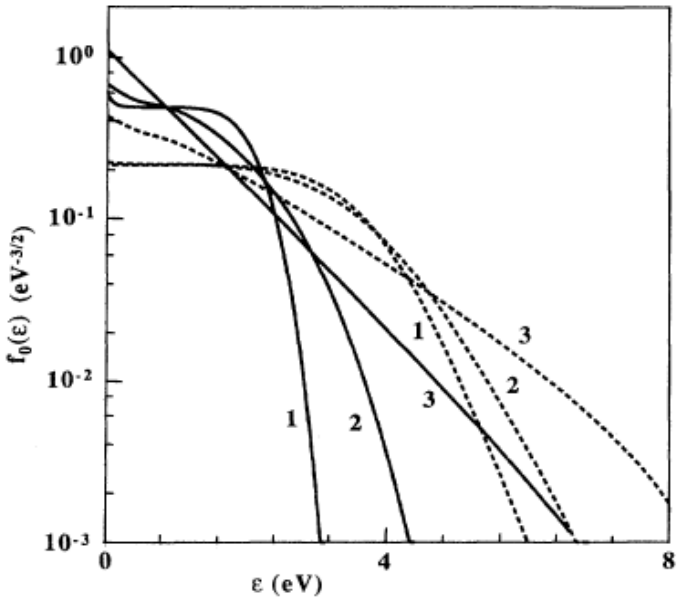

Figure 3.1. The calculated EEDF as a function of electron energy in xenon. The full curves are values at $E/N = 4\times10^{-18}$ V·cm^2 and the broken curves 2×10^{-17} V·cm^2. (1) $\alpha = 0$; (2) 10^{-7}; (3) 10^{-5} (Aleksandrov *et al.* 1996).

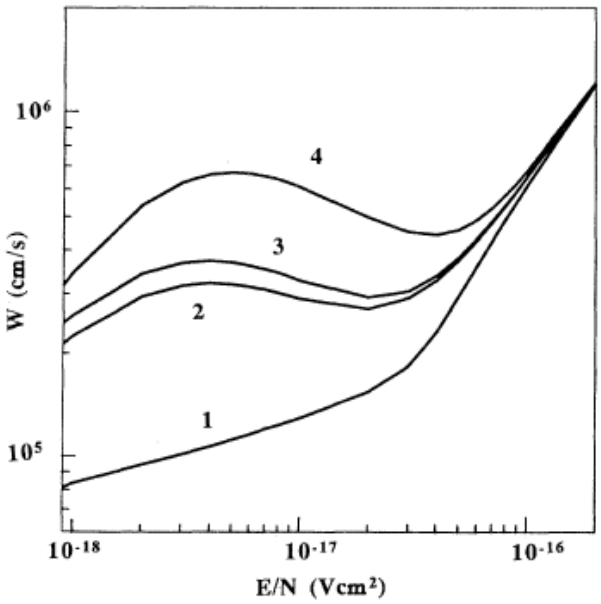

Figure 3.2. Calculated electron drift velocities in xenon (Aleksandrov *et al.* 1996) by the use of equation 3.6 for several sets of α and δ. (1) $\alpha = \delta = 0$; (2) $\alpha = 10^{-6}$; $\delta = 0$; (3) $\alpha = \delta = 10^{-6}$; (4) $\alpha = 10^{-6}$, $\delta = 10^{-5}$.

3.3 NEGATIVE DIFFERENTIAL CONDUCTIVITY (NDC)

The negative differential conductivity is known as a phenomenon exhibiting unusual responses of the system, leading to oscillation or pattern formation in semiconductor physics (Shaw *et al.* 1992) and gas discharge physics (Alexander *et al.* 2004). It has been extensively investigated because it can cause undesirable instabilities.

In weakly ionized dc discharges, two types of S-shaped negative differential conductance (SNDCs) exist in the j-V curve where j is the current density and V is the total voltage between electrodes. S-shaped NDC has an increase in j with a drop in V. The SNDC can be alternatively expressed in the I-V curve, but it typically shows discontinuity. SNDCs in dc discharges are explained by different mechanisms depending on the operating current density. While the SNDC in glow-to-arc transition is due to emission of secondary electrons from the cathode surface, that in the region between the Townsend discharge and normal glow is caused by an abrupt increase in electron-ion pairs by impact ionization. Note that SNDC can also be seen in semiconductors in which two charge carriers (electrons and holes) are produced by impact ionization (Adler *et al.* 1980).

There is another type of NDC whose characteristic contains a nonlinear relation of w to E/N as shown in figure 3.3(a). This type of NDC is referred to as N-shaped NDC (NNDC) hereafter. NNDC may result from negative differential mobility (NDM), so that a range of fields containing a relation $\mathrm{d}w/\mathrm{d}E < 0$ exists. Such a characteristic exhibits N-shaped NDC. One of the mechanisms is discussed in section 3.2.2.

3.3.1 General Characteristics in SNDC

The instability resulting from SNDC of the *I-V* characteristic seems to be the earliest known plasma instability – it was already reported in the year 1900 (Kaufmann, 1900). The stability condition and the mechanism of the SNDC between the Townsend discharge and normal glow are discussed in the following.

Consider a simple discharge configuration with parallel cathode and anode with a ballast R connected in series. A typical *I-V* characteristic of the discharge and the load line are illustrated in figure 3.4. At the point *A* where the load line starting from the applied voltage V_b cuts the *I-V* characteristic, the following fundamental relation is satisfied with respect to the closed circuit:

$$V = V_b - IR \tag{3.7}$$

where *V* is the discharge voltage. The following consideration explains that point *A* is a stable point and *D* is not: Assume that by some transient condition the current is reduced such that the operating point is shifted to *B*. Then the positive voltage difference δV arises as

$$\delta V = V_b - IR - V \ . \tag{3.8}$$

If there is no inductance in the circuit, δV is spent to accelerate electrons further. Subsequently, the increase in the ionization rate will cause an increase in the current until equation 3.7 is satisfied. On the other hand, the current would be decreased to the stable point *A* if the operating point is placed at *C* for the opposite logic. Thus, accidentally small perturbation in the vicinity of *A* results in damping of the current variation. It would seem that point *D* is also a stable point as well as *A*. However, if the current is slightly increased from *D* to *B*, the preceding discussion leads it to point *A*. A slight decrease in

the current at D results in a negative value δV, causing a further reduction in the current. Thus, unlike point A, point D is not a stable point. This discussion induces a criterion for stability as

$$\frac{dV}{dI} + R > 0 \tag{3.9}$$

where dV/dI is the slope of the discharge characteristic at the operating point and R is that of the load line. This condition is called Kaufmann's criterion (Kaufmann 1900).

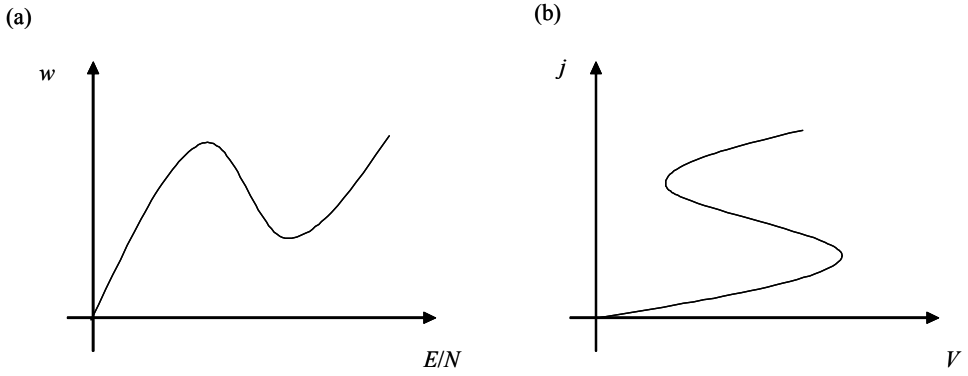

Figure 3.3. Illustrations of negative differential conductivities. (a) NNDC in a diagram of drift-velocity versus reduced electric field and (b) SNDC in a diagram of current density versus voltage.

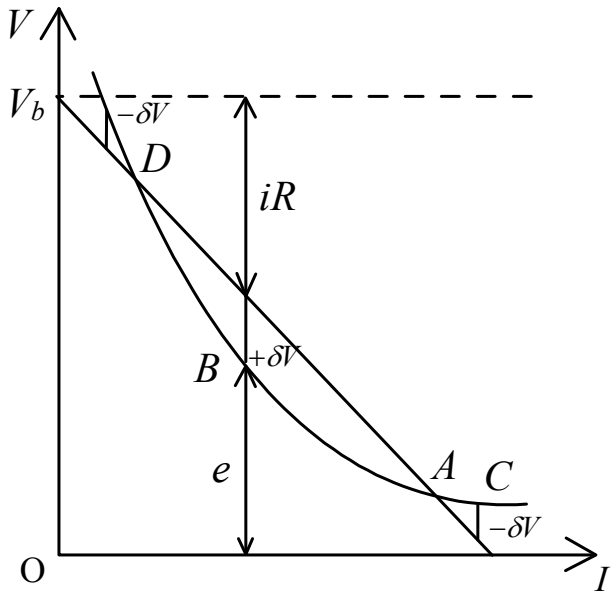

Figure 3.4. A diagram of the voltage across electrodes versus current. The diagonal line represents the load line and the *I-V* curve across the plasma.

CHAPTER IV

SELF-ORGANIZATION

Among the various instabilities in plasma physics, some enter equilibrium with pattern formation while others cause the instabilities to develop and quench the plasmas. These pattern formations are often referred to as "self-organization" of the plasma.

There have been a number of experimental observations of pattern formations revealed by various methods. Their features are roughly classified by appearance: striations perpendicular to the current flow and filamentary structures parallel to the current flow. The latter is studied hereafter with an emphasis on self-organizations with a low-current, dc operation. Although several observations of such self-organizations have been made, theoretical works leading to the dynamics of the filamentary pattern formation are quite few. This section introduces four representative pattern formations or theories reported for the past few decades. 1) Nasuno (2003) demonstrated unique pattern formation such as lined spots in air at 35 – 45 Torr in parallel-plate geometry. To the best of our knowledge, this is the only report, besides self-organization in CBL discharges, that employs a metal cathode. 2) Purwins' group has demonstrated a variety of pattern formations including DBD discharges (Muller *et al.* 1999). In order to account for 1-D pattern formation that was observed by Radehaus *et al.* (1987), a model has been proposed leading to a bistable system close to Turing instability. 3) Korolev *et al.* (1979) observed pattern formation using nitrogen in non-self-sustained volume discharges. The theoretical insight will be qualitatively explained. 4) Benilov (1998, 2007) has developed a theoretical explanation for well-known cathode spots in arc (Lieberman *et al.* 1994). An application of this theory to self-organization in CBL discharges is made by Benilov

(2007). The approach is introduced in this thesis, and the patterning yielded from the governing equations is summarized.

4.1 SELF-ORGANIZATION WITH A PARALLEL-PLANE GEOMETRY

Pattern formation in air discharge has been reported by Nasuno (2003), demonstrating dynamic dancing of luminous spots in a quasi-two-dimensional geometry. The gap maintained by a spacer has a thickness of d = 100 μm, and the pressure ranges from 35 Torr to 45 Torr. The plasma reactor consists of a nickel plate as a cathode and an indium-tin oxide coated (ITO) glass as an anode from whose side the discharges are monitored by an ICCD camera. The electrodes are connected to a dc power supply and operated at either a constant voltage of 2 kV or a constant current up to 1.5 mA via a ballast resistor (35.2 kΩ). The observed patterns in air are stationary localized patterns, i.e., a single snaking luminous string, teleportation of spots, or merging of spots. Moreover, a rich variety of dynamic patterning behaviors is confirmed, e.g., teleportation, coupling, and looping plasmas. Such behaviors of the patternings mostly depend on the pressure and the current. This phenomenon has been theoretically investigated by Sugawara *et al.* (2005), using an equivalent electric circuit model. This model provides a pair of reaction-diffusion equations with respect to the current and the electric charges accumulated in the cathode fall region.

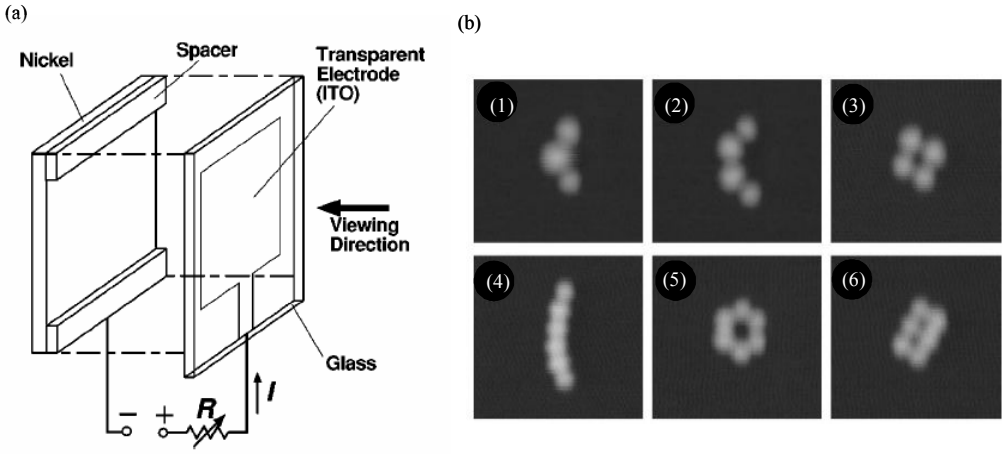

Figure 4.1. (a) A schematic diagram of the plasma reactor. The cathode is a nickel plate of 50 mm × 50 mm × 3 mm, and the anode consists of a thin transparent conducting film of indium-tin-oxide (ITO) on the glass plate. (b) Pictures of the observed patterns (Nasuno, 2003).

4.2 SELF-ORGANIZATION WITH A SEMICONDUCTOR CATHODE

4.2.1 Observation of self-organization

Gurevich *et al.* (2005) have experimentally confirmed unique pattern formations in dc plasmas with a semiconductor cathode. The experimental set-up consists of a parallel-plate electrode geometry with a gap thickness of 0.01 to 0.1cm as shown in figure 4.2(a). The gas-discharge area perpendicular to the surfaces of the electrodes has a diameter D = 1.5 cm. The most distinctive difference from the pattern of Schoenbach *et al.* (2004) is that they employ semi-insulated GaAs which allows the electrical potential to be distributed along the surface of the cathode. The anode is a thin conductive layer of indium-tin oxide (ITO) coated glass through which a CCD camera monitors the pattern formations (figure 4.2(a)). In the experiments, pure argon (99.998%) or nitrogen (99.998%) is used, and the operating pressure is typically p = 100 Torr. The dc voltage is applied across the cathode and the transparent anode with a sustaining voltage of 50 to 250 V. On the back of the cathode, a copper tube is attached through which liquid nitrogen flows to maintain the cathode in a cryogenic condition ranging from 100 K to 150 K. Controlling the temperature, current, and the pressure plays a primary role in changing the patternings. The low temperature also offers a stabilizing effect on the patternings.

A variety of stable patternings have been reported with the experimental setup using nitrogen. Figures 4.2 (b) to (e) display the representative appearance of such as the current increases, at a fixed temperature and pressure of T = 110K and p = 110 Torr, respectively. The patterning shown in figure 4.2(b) is observed where the current is ~ 60 μA until it changes its appearance to figures 4.2(c) and (d) where I = 90 μA. Rotation of

the pattern has been observed. The pattern may change the direction of rotation or undergo transformation into a spiral pattern in figure 4.2(d) which maintains its rotational velocity in about 2π rad/sec.

In addition, Purwins *et al.* (1997) observed through the use of the plasma reactor above, a nitrogen glow discharge undertaking a transition into hexagonal or striped patterns as the total current is increased.

4.2.2 Proposed mechanism with a treatment of reaction-diffusion process

The Turing pattern was proposed in a remarkable paper by Turing (1952) as a phenomenon occurring in chemistry and biology where reaction and diffusion play an important role. The important feature of the system is the competition between different temporal growth rates and spatial ranges of diffusion for the different chemicals in the system. Generally the governing equations consist of two sets of equations with respect to two concentrations u and v:

$$\frac{\partial u}{\partial t} = D_u \frac{\partial^2 u}{\partial x^2} + f(u,v) \tag{4.1}$$

$$\frac{\partial v}{\partial t} = D_v \frac{\partial^2 v}{\partial x^2} + g(u,v) \tag{4.2}$$

where D_u and D_v are diffusion coefficients of u and v, respectively. $f(u,v)$ and $g(u,v)$ consist of production and removal terms which could be nonlinear. This system can lead to instability toward a time-independent state with spatial oscillation. This contrasts the Hopf bifurcation, which exhibits space-independent, temporal oscillation.

Unlike Turing's theory, which greatly developed understanding of pattern formation in biology and chemistry, such approaches in gas discharges have been hindered until Radehaus *et al.* (1990). They utilized reaction-diffusion equations leading

to a bistable system analogous to Turing instability to account for pattern formation. The experimental result that motivated their formulation was a 1-D pattern formation by using a reactor with a semiconductor cathode as shown in figure 4.3(a). Their rigorous treatment shown in the equations below includes diffusion terms with respect to *v* and *w* that represent variations of current density, *j*, and voltage, υ,:

$$\frac{\partial v}{\partial \tau} = \sigma \Delta v + f(v) - w \tag{4.3}$$

$$\frac{\partial w}{\partial \tau} = \Delta w + v - w - T \tag{4.4}$$

with the two variables defined as $w = -U / U^*$, $v = j / j^*$. The derivation of these equations is summarized in Appendix A. In equations 4.1 and 4.2, the variables *w* and *v* represent concentrations of two substances, but in equations 4.3 and 4.4, *v* and *w* denote variations of the current density and the voltage, respectively, at the interface Ω of a nonlinear and linear layer shown in figure 4.3(b). The variation of the current density *j* is denoted by j_{10} in figure 4.3(b). The set of equations implies the possibility of a system called bistability in which the interaction of *j* and υ may form a pattern, leaving time-independent perturbations with respect to *j* and υ. The set of equations is derived from Poisson's equations and continuity equations (see Appendix A), with a model illustrated in figure 4.3(b). The model has been solved numerically in one-dimension, and a spatially-periodic structure of *j* and υ was obtained as shown in figure 4.3(c).

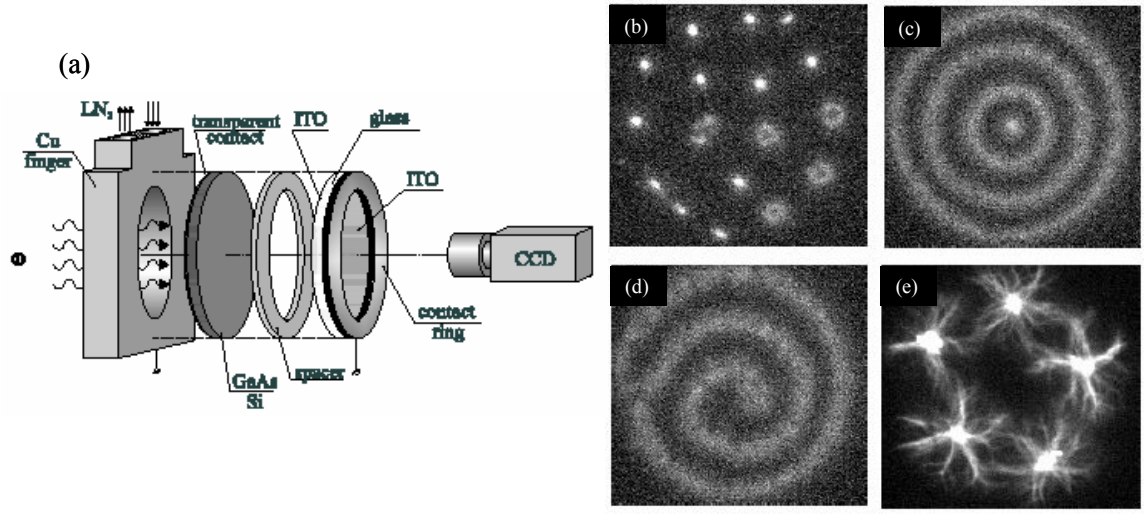

Figure 4.2. (a) An illustration of the discharge cell and the experimental set-up. The pictures of the observed pattern in nitrogen at current I = (b) 60 μA; (c) 90 μA; (d) 90 μA; (e) 870 μA. The temperature controlled by the cryogenic finger ranges from 100 K to 150 K. The transparent ITO coated glass enables the CCD camera to observe the discharges (Gurevich *et al.* 2005).

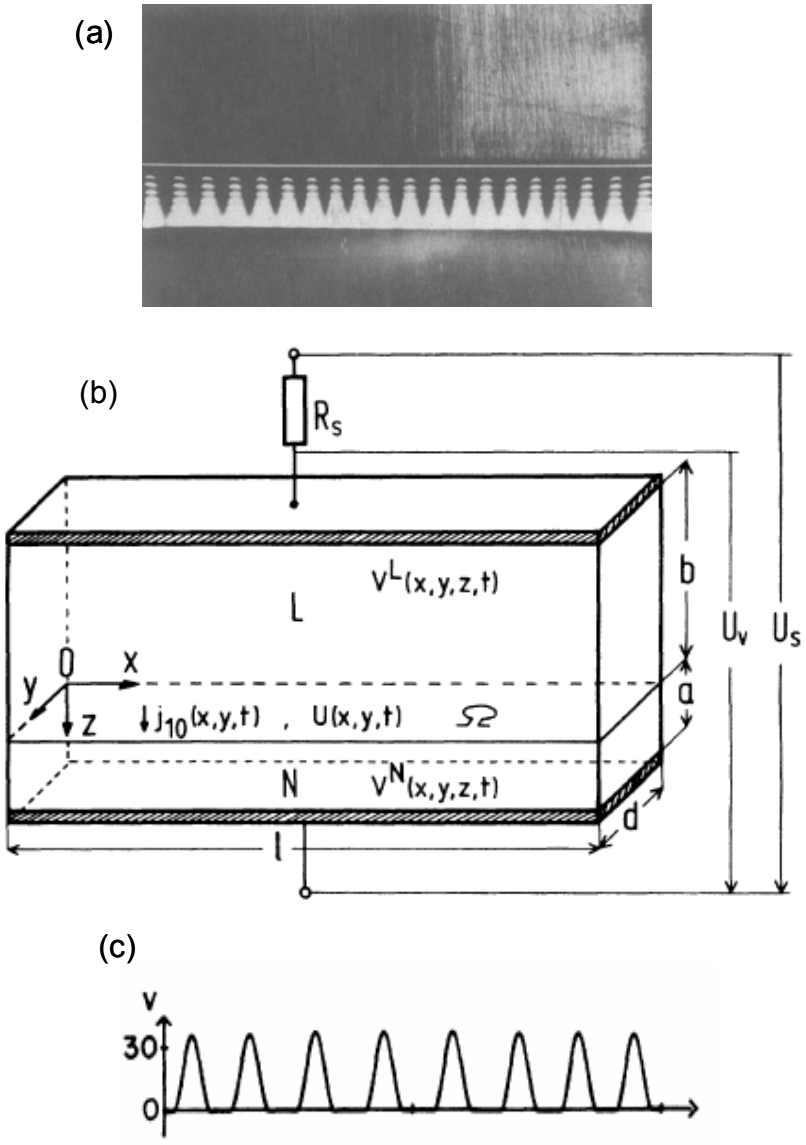

Figure 4.3. (a) A cross section of a stationary pattern formation in He at 100 mbar. (b)A schematic of the model of a plasma consisting of two layers L and N. The deviation of the current at the interface is denoted by j_{10}, and the deviation of the voltage by U. (c) The result of the numerical calculation. The abscissa represents the position, and the ordinate v, the fluctuation of the voltage (Radehaus *et al.* 1990).

4.3 SELF-ORGANIZATION IN VOLUME DISCHARGES

Korolev *et al.* (1979) investigated volume discharges whose current is maintained by an electron beam through an accelerator extraction window. The electron beam is directed through the window to the gas and generates a plasma as shown in figure 4.4(a). The electric field between the electrodes provides the charged particles with a current path from the anode to the cathode. One of the features of the volume discharges is that a subnormal discharge is observed when the current is decreased to a certain level, showing a SNDC in the *I-V* characteristic. Self-organization is simultaneously observed at the surface of the cathode, arranged from inner to outer circles, for non-self-sustained discharges in nitrogen or methane. Cross-section views of self-organization in N_2 are displayed in figures 4.4(b) and (c) at $t = 1$ μs and $t = 10$ μs, respectively.

The SNDC is attributed to the change of the relation between the first Townsend coefficient, α, and E/N, which is described in section 2.1.3. The consequence of such a change of the kinetic process is reflected in a relation between the local current density, j, and the voltage, υ. The authors constructed an *a priori* model of this pattern formation using this concept combined with an assumption that the sustaining voltage spatially diffuses parallel to the cathode surface. Figure 4.5 illustrates the spatial distribution of the current density and the voltage at the cathode surface ($x = 0$) in a subnormal discharge. Consider that the mean current density, j_0, is less than its normal value, j_n, (figure 4.5). When a fluctuation $j(y)$ appears in a uniformly distributed current density j_0, the potential $V(y)$ also exhibits a fluctuation having an opposite sign (region I) to follow the negative characteristic *I-V* curve. The transverse electric fields from III to I and II to I cause the flows of current, which further increase the current density in region I. As a result, the

current density in regions of I type returns to its normal value. Note that this instability does not increase the total current, so the instability cannot be stabilized by the external circuit parameters. The fluctuation stops developing since the total current is limited. The wavenumber of the fluctuation that develops in this discharge is determined by the diffusion effect of the voltage.

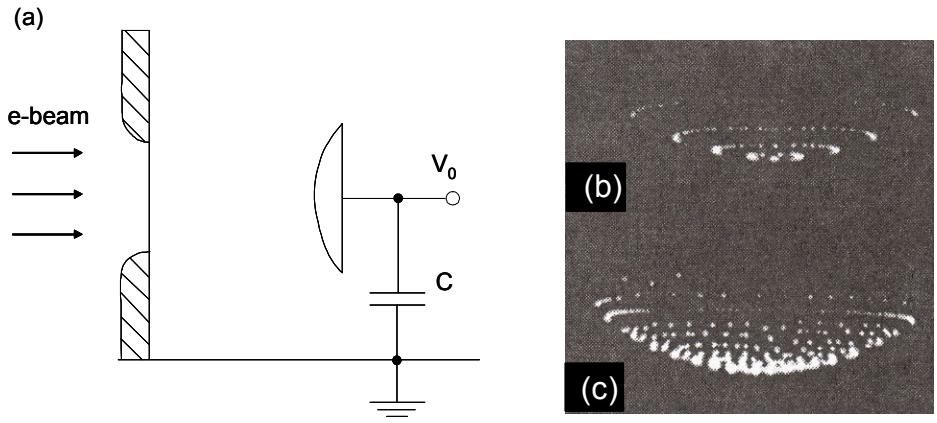

Figure 4.4. (a) An illustration of the reactor of a non-self-sustained volume discharge. (b) Photographs of the self-organization on the cathode surface at 760 Torr, E_0 = 5 kV, and t = 1 μs. (c) the same condition but t = 10 μs (Korolev *et al.* 1979).

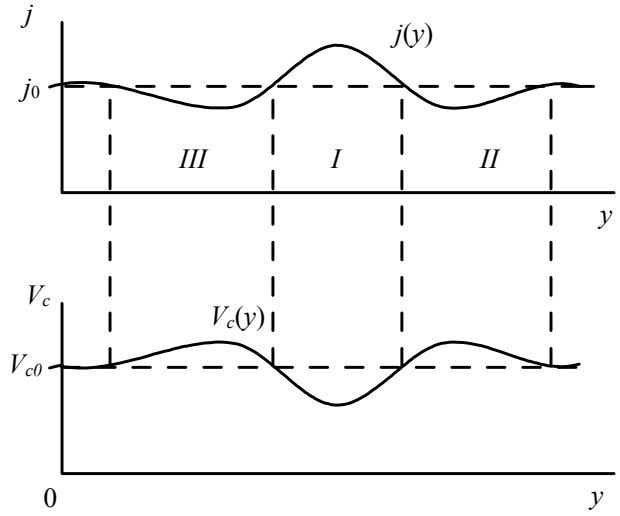

Figure 4.5. Illustrations of the spatiotemporal perturbations of the current density $j(y)$ and the cathode fall voltage $V_c(y)$ as a function of position (Korolev *et al.* 1998).

4.4 TRANSITION TO ANOTHER BRANCH OF j-V CURVE ACCOUNTING FOR SELF-ORGANIZATION IN CBL DISCHARGES

Benilov has made a comment (2007) on our two publications (Takano *et al.* 2006 and Schoenbach *et al.* 2004) and proposed that the self-organization in the CBL discharges can be explained by basic theories on glow discharges incorporating ionization, recombination, diffusion, drift, and secondary electron emission. The author interprets the manifestation of the self-organization as an indication of N-shaped nonlinearity (this thesis refers to it as SNDC) of the current and voltage. In the discharge mode where the current density is uniformly distributed, the distribution of discharge parameters in the near-cathode region is one dimensional (1D), and it is expressed as $f = f(z)$. (The origin of Cartesian coordinates x, y, z is on the cathode surface and the z-axis is parallel to the current flow.) Multidimensional distributions of parameters associating pattern formation on the cathode would then be given by $f = f(x,y,z)$. The discussion proceeds from a principle that one of the multidimentional functions $f(x,y,z)$ may also be a solution to a governing equation of 1D solution. The mathematical description of the system starts from Poisson's equation and the continuity equation for ions and electrons (Benilov 2006):

$$\frac{\partial n_i}{\partial t} = \nabla \cdot (-\mu_i n_i \nabla \phi) \tag{4.5}$$

$$\varepsilon_0 \Delta \phi = 4\pi e(n_e - n_i) \tag{4.6}$$

$$\frac{\partial n_e}{\partial t} = \nabla \cdot (\mu_e n_e \nabla \phi) + \nu_i n_e - \nu_{dif} n_e - \beta_{dis} n_i n_e \tag{4.7}$$

where μ_i and μ_e are the mobilities of the ions and electrons, respectively, ν_i is the ionization coefficient, β_{dis} is the frequency for the dissociative recombination, ν_{dif} is the

diffusional loss frequency. The right-hand side of equation 4.7 takes into consideration the diffusion or recombination losses. The parameters, μ_i, and μ_e are assumed constant and given, and v_i depends on α which is a function of E as $\alpha = \alpha(E)$. In equation 4.5, the diffusional loss of ions is neglected. The SNDC can be obtained by solving the 1-D simulation using equations 4.5 to 4.7, combined with a defined voltage distribution from the cathode surface to the anode. Next, the distribution of the electric potential is assumed to be of the form

$$\phi = f(z)\Phi(x, y) \tag{4.8}$$

where z is normal to the cathode surface with $z = 0$ and $z = L$ (> 0) corresponding to the cathode surface and anode, respectively, and $f(z)$ is the z component of the nonlinearity of potential distribution. The case of $\Phi(x, y) = 1$ gives the case of 1D solution and a variation in $\Phi(x, y)$ accounts for branching off the bifurcation to multidimensional solutions. With this assumption, it is found that Φ obeys Helmnoltz equations as

$$\frac{\partial^2\Phi}{\partial x^2} + \frac{\partial^2\Phi}{\partial y^2} + \frac{\partial^2\Phi}{\partial z^2} + k^2\Phi = 0 \tag{4.9}$$

with k representing the wave number of Φ. The equation can be solved with the Neumann boundary condition in the cylindrical coordinates (r, Φ, z) with the origin at the center of the cathode (Benilov 1988). The solutions can be expressed by a Bessel function of the first kind of order v ($v = 0, 1, 2$ ..) as

$$\Phi = J_v(kr)\cos v\theta \qquad k = j_{v,s} / R \tag{4.10}$$

where $j'_{v,s}$ is an s^{th} zero of the derivative of $J_v(x)\cos v\theta$, $s = 0, 1, 2, 3 \ldots$, and $R = 0.375$ mm is the radius of the cathode. For example, two of the solutions are illustrated in figure 4.6.

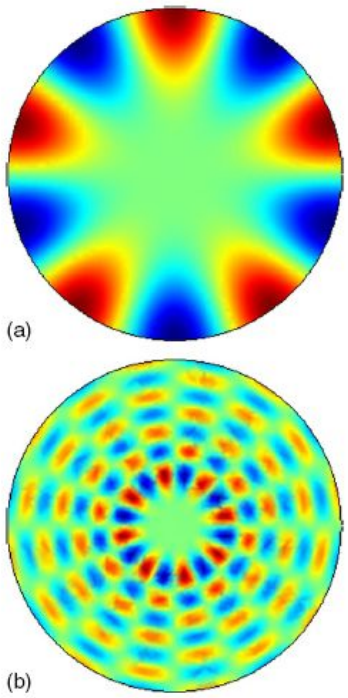

Figure 4.6. The static patterns obtained by solving equation 4.10. (a) $v = 5$, $s = 1$ and (b) $v = 8$, $s = 7$ where v and s are integers in equation 4.10 (Benilov 2007).

CHAPTER V

EXPERIMENTAL SETUP

To study the pattern formation in CBL discharges, CBL plasma reactors were fabricated with varied radial sizes and cathode materials. Another type of reactor, which has parallel-plate geometry, was also tested to facilitate the understanding of the distribution of the electric field near the anode.

The discharges were diagnosed using several techniques. Electrical measurement and imaging in the visible spectra offer basic information on the *I-V* characteristics and appearance of the plasmas, respectively, following Moselhy's (2003) experiments. The imaging in the visible has a new feature, namely, side-on measurement, allowing us to obtain information on the structure of the cathode fall and the negative glow, leading to the derivation of the secondary Townsend coefficient. Imaging by a VUV camera and spectroscopy in the VUV range gives intensity information of emissions around 172 nm. A temperature measurement on the back of the cathode was carried out to estimate the degree of thermionic emission of electrons from the cathode in addition to secondary emission.

5.1 PLASMA REACTOR AND ITS OPERATION

Typical electrode configurations for the CBL microdischarges are shown in figure 5.1. The electrode design as shown in figure 5.1(a) was used for most of the studies except side-on observations in the visible. The configuration shown in figure 5.1(b) is used for a side-on observation to take the picture in figure 6.17. The cathode and the anode are separated by a borosilicate disk with a thickness, d, which can be adjusted between 150 to 500 μm. The borosilicate is transparent in the visible and allows

observation of the discharge side-on. The planar cathode is made of molybdenum, copper, aluminum, titanium, or tungsten foil with a typical thickness of 250 μm. Molybdenum was used in most of the measurements unless noted. A well polished tungsten wire with a diameter of 750 μm was also used as a cathode. For single-filament observations, a smaller reactor with D = 300 μm was selected. The surface of these cathodes is planar and does not have any structures such as microholes. The dielectric and the anode have a circular opening with a diameter of D which determines the opening area of the cathode. The electrode system with the reactor is housed in the vacuum chamber with two transparent quartz windows that offer 60% transmittance for 172 nm. Prior to the experiments, the system is evacuated to a pressure less than 10^{-5} Torr, flushed once with xenon gas, and then filled with xenon (99.999% purity) to a pressure, p, ranging from 30 to 140 Torr. The electrical power is supplied in a direct current mode with a 100 kΩ ballast resistor connected in series to the plasma reactor as shown in figure 5.2. The power supply (Glassman PS/ER03R100-115) provides 1500 V and 100 mA maximum with a positive polarity. Another resistor R_c = 1 kΩ is connected in series to the ballast resistor to evaluate the current ($I = V_c/R_c$) through the plasma. The breakdown voltage is in the range of 600 to 700 V in our experimental set-up ($pd \sim$ 1 to 5 Torr cm). The sustaining voltage does not exceed 500 V in the range of our observations.

Realization of self-organization in a simpler geometry, parallel-plane geometry, is significant to demonstrate whether the unique CBL configuration essentially contributes to the formation of patterns. A new reactor was designed and fabricated with the anode facing the cathode as shown in figure 5.1(c). The anode is a glass with a 1200 to 1600 Å thick tin-indium-oxide (ITO) coating (the surface resistivity of the ITO cathode: η = 10

Ω/sq). A 30 μm gap was created between the anode and the borosilicate dielectric so that xenon gas could fill inside the reactor. The molybdenum cathode contacts the dielectric. The interelectrode distance is thus 280 μm.

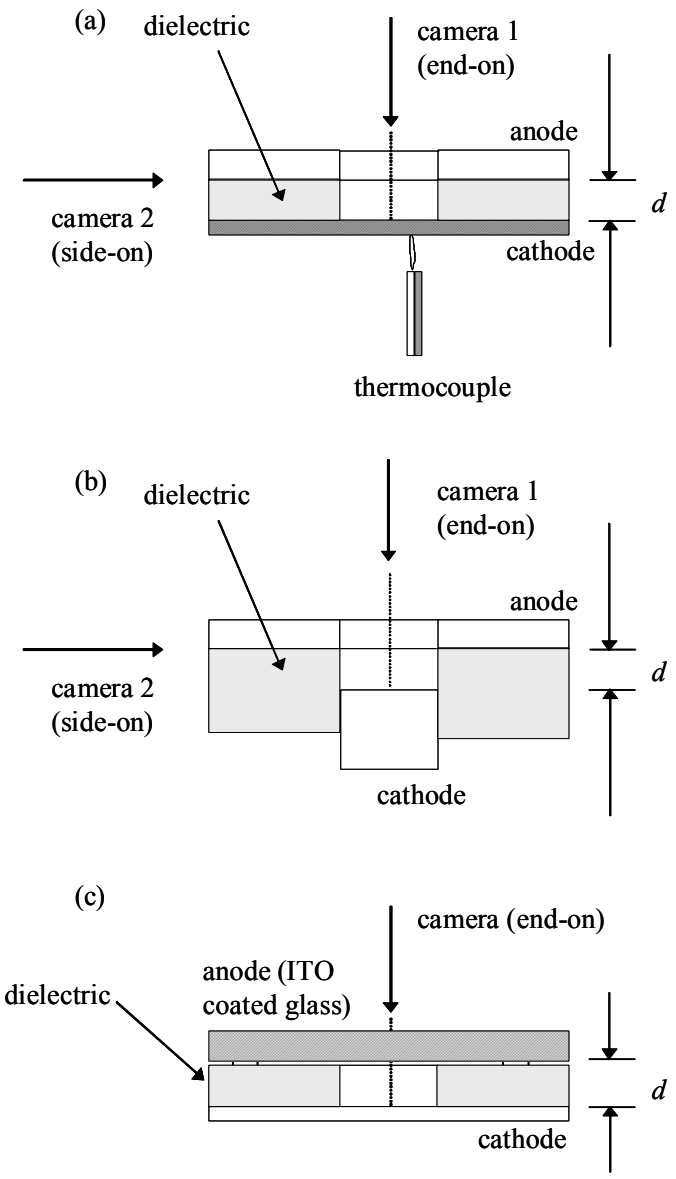

Figure 5.1. Three cross-sectional views of the plasma reactors are shown. (a) The diameter of the circular opening of the anode and dielectric varies between 300 and 750 μm. The thickness of the dielectric and the cathode is d = 250 μm and 25 μm, respectively, and that of the anode is 100 μm. A thermocouple is attached to the back of the cathode. This configuration was used in almost all studies; (b) a configuration used for the side-on observation shown in figure 6.17; (c) Indium-tin-oxide (ITO) coated glass is used as the anode. Because of the conductivity of ITO (the surface resistivity of the ITO cathode: η = 10 Ω/sq), the layer is transparent to visible light but sufficient to carry the radial discharge current.

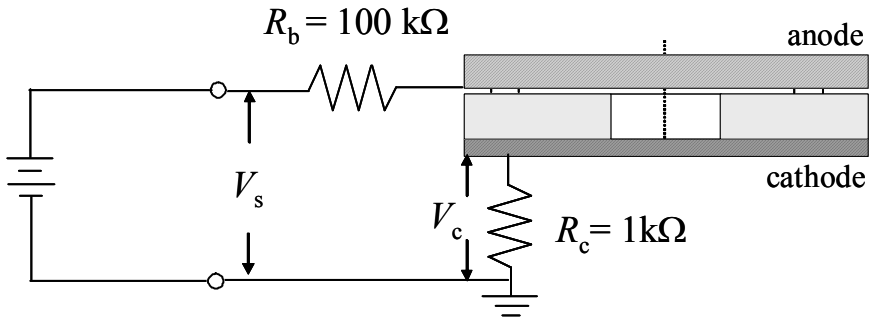

Figure 5.2. The electrical system consisting of a power supply, the ballast resistor R_b, and the current reading resistor R_c.

5.2 MEASUREMENT TECHNIQUES

5.2.1 Current and voltage measurement

The discharge voltage is measured with a voltage probe (Tek P5100) and recorded by an oscilloscope (Tektronix TDS 3052). The current through the plasma is measured by means of a current viewing resistor with a resistance of 1 kΩ in series with the ballast resistor (figure 5.2).

5.2.2 End-on and side-on imaging in the visible

Two identical CCD cameras (Panasonic GP-KR222) with a telescopic lens operating in the visible range are placed end-on and side-on to monitor the discharges simultaneously. The cameras with an S/N ratio of 50dB incorporate a ½ inch video chip with 380,000 effective pixels that features digital RGB signal processing. These cameras provide a capture speed of 30 frames per second, and the data is transferred to a PC and saved as images. The directions of end-on and side-on are indicated in figure 5.1.

5.2.3 Spectroscopy in the visible and near infrared (NIR)

Visible and NIR spectra were recorded using an Acton Research spectrometer SpectraPro-500i consisting of a 3600 grooves/mm grating and a photomultiplier tube (R928, Hamamatsu) as shown in figure 5.3. The emission from the discharge is introduced into the entrance slit via a lens with a focal length of 5 cm. Both the entrance and exit slit width are continually adjustable from 0.02 mm to 3 mm. The spatial resolution is limited by the slit width. The photomultiplier voltage is set from 450 to 800V. In an ideal setting, one can attain 0.05 nm resolution at 435.8 nm. The signals from the photomultiplier were acquired using a computer.

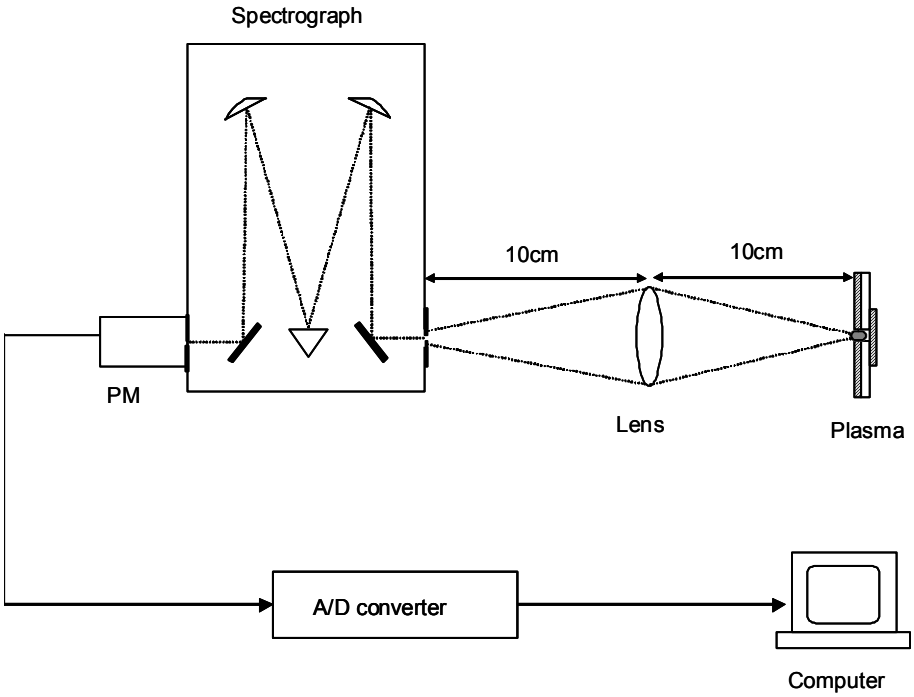

Figure 5.3. A schematic view of the experimental setup for OES in the visible and near infrared.

5.2.4 Calibrated detector measurements

In order to obtain absolute optical power emission in the VUV range, a calibrated radiometer (International lights IL1400) with a calibrated detector (SED185) was employed. The detector has an 8 mm diameter photocathode, i.e., the area is 50.24 mm^2, with a quartz window protecting it. The responsivity profile of the detector with the quartz window ranges from 160 to 240 nm peaking at 185 nm. Because the detector was pressed against the viewport of the chamber, it is presumed that there is negligible absorption of photons by the air. For the calculation of the optical power density at the plasma, an assumption is made that the plasma is a point source radiating isotropically. Therefore, the radiometer reading given in a unit of W/cm^2 is multiplied by $4\pi r^2$ where r is the distance from the light source. The resultant values represent the total power ideally detectable if the shape of the detector is a sphere containing the light source. Yet, this is not the total power emitted from the plasma because the spectral responsivity of the detector and transmittance of the quartz viewport of the chamber (83 % at 172 nm) are not taken into account. The absolute power is given after those corrections, and the absolute power density is calculated by dividing the absolute power by the area of the anode opening.

Another calibrated detector (International lights SEL006) was used with the calibrated radiometer (International lights IL1400) for measuring emission power densities from visible to near infrared (NIR) wavelengths. The detector incorporates a GaAs photodiode (Hamamatsu G8522-03) with an effective area of 0.113 mm^2. The peak irradiance response sensitivity factor calibrated at 823 nm, 1.08×10^{-4} $A \cdot cm^2 \cdot W^{-1}$, is given assuming monochromatic irradiance. The spectral range is from 400 to 890 nm.

The same procedure was used for the calculation of absolute radiant power densities except that the transmittance through the viewport was considered negligible.

5.2.5 VUV imaging

Camera 1 (end-on) was replaced with a VUV camera (ICCD-MAX provided by Princeton Instruments) to record images of the plasma at the wavelength of the xenon excimer emission (172 nm). A schematic of the set up for this ICCD camera is shown in figure 5.4. The tube connecting the discharge cell and ICCD camera is connected to the vacuum system. A MgF_2 lens with a focal length of 5 cm focuses the discharge image onto the CCD elements. The emission is observed through the lens and an optical filter with a peak transmission rate of 24% at 170.9 nm and a full-width at half maximum (FWHM) of 26.8 nm.

5.2.6 Emission spectroscopy in VUV

For measurements of VUV excimer radiation in xenon (172 nm), a 0.2 m vacuum VUV Mcpherson monochromator (model 234/302) was used. This monochromator covers a spectral range from 50 nm to 300 nm and contains a concave holographic grating with a groove density of 1200 grooves/mm and is blazed at 150 nm. The scanning can be controlled using a scanning controller (model 789A-3) with a stepper motor that determines the positioning of the grating. Figure 5.5 shows a schematic of the monochromator setup. In order to avoid absorption of the VUV spectra by the air, an ALCATEL DRYTEL 31 pump is used to maintain the pressure inside the spectrogram at less than 1 mTorr. Therefore, the deterioration of the spectra is considered negligible. For high spectral resolution, the slit widths (both entrance and exit) were adjusted to 100 μm.

The light is collected with a Hamamatsu photomultiplier tube (PMT) model R 1533 that covers a wide spectral range from 30 to 600 nm.

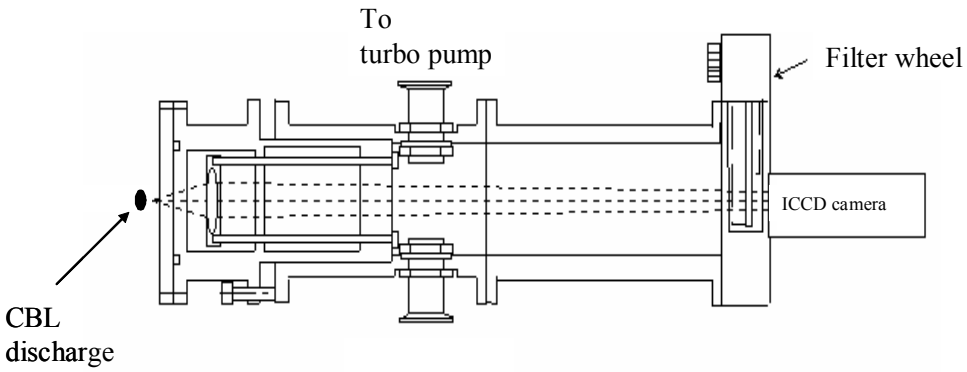

Figure 5.4. A cross sectional illustration of the VUV imaging system. The tube connecting the chamber and ICCD camera is connected to the vacuum system. The filter wheel enables the change of the optical filter.

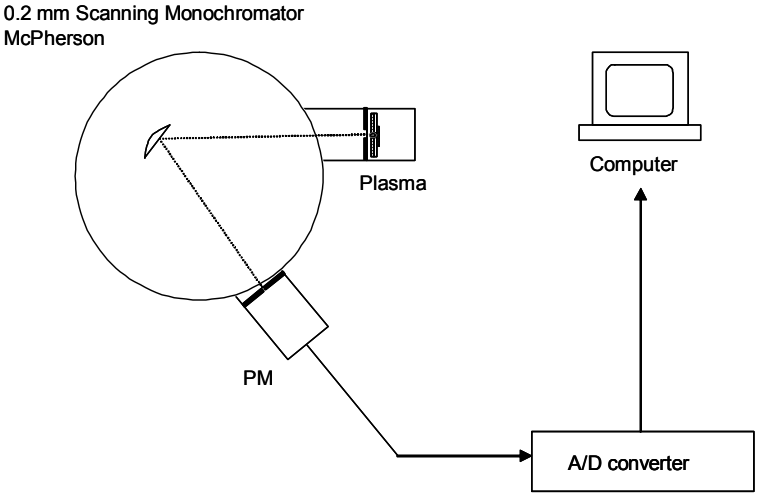

Figure 5.5. The diagnostic setup for VUV spectroscopy. The light from the plasma is led through an entrance and exit slit and detected by the photomultiplier.

5.2.7 Temperature measurement at cathode

For the temperature measurement at the back of the cathode, the 250 μm-thick cathode was replaced by a 25 μm-thick molybdenum film. The use of the thin cathode is to minimize thermal flow inside the cathode. The plasma reactor was attached to the chamber wall so that the cathode was exposed to the air. The contact between the anode and the chamber wall was sealed using Torr Seal® (Varian). In order to obtain a temperature distribution, a K-type micro-wire thermocouple (unsheathed T/C, measurable up to 2552 K, OMEGA Engineering, Inc.) was manually pushed against the back of the cathode. Because the diameter of the thermocouple is ~13 μm, the temperature measurement obtains a segmented 2D temperature distribution with a scanning resolution of ~13 μm. Since a viewport is installed in the chamber, the appearance of the plasma can be monitored while temperature and *I-V* measurement are conducted.

CHAPTER VI

RESULTS

6.1 END ON OBSERVATION IN THE VISIBLE

6.1.1 Observation in xenon

The CBL discharge was operated in dc with an electrode configuration as shown in figure 5.1(a). The diameter of the circular dielectric and anode opening was generally D = 750 μm. The thickness of the dielectric layer, d, was 250 μm. The xenon gas pressure, p, was fixed at 75 Torr. In this parameter setting, the product of the pressure and interelectrode distance, pd, is located on the right-hand side of the Paschen minimum.

End-on images of a discharge in xenon at 75 Torr are shown in figure 6.1, with current I as a parameter. The homogeneous plasmas shown in figures 6.1(a) and 6.2(b) are in abnormal glow mode in which the visible radiation becomes higher with increasing current. As the current is lowered, the diameter of the emissive region decreases as shown in figure 6.1(b). The self-organization (figure 6.1(c)) occurs with a further decrease of the current. The current channels are called filaments hereafter. The observed discharge structures are stable, except for the structure preceding the onset of self-organization (figure 6.1(c)). The transition from one pattern structure to another occurs on a timescale of less than 33 ms. It was not possible to observe the transition with our CCD camera, which has a shutter speed of 30 frames/sec. The early stage of discharges with diffused filaments with low luminosity will be called “diffuse mode.” The discharges shown in figures 6.1(d), (e) and (f) pertain to the diffuse mode. Those which show filaments with a well-defined diameter (figure 6.1 (g, h, j) are defined as “confined mode.” It needs to be noted that the discharge, once it enters a confined mode, can only be sustained when the

current is lowered at 75 Torr. Attempts to increase the current, when the discharge is in this phase, lead to extinction of the discharge.

Self-organization was observed in xenon with a high gas purity of 99.999%. Even small amount of impurities do not allow self-organization. In addition to the dependence on gas purity, the electrode material played an important role. Self-organization was observed when molybdenum or tungsten was used as cathode material, but it was not observed with a copper cathode.

6.1.2 Observation in krypton

Krypton shows characteristics analogous to xenon, such as forming diatomic molecules Kr^*_2 and emitting UV photons when excited. Krypton has an atomic number of 36, closer to xenon (atomic number: 54) than other noble gases, argon (atomic number: 18) or neon (atomic number: 10). It was thus presumed that krypton would be one of the leading candidates for self-organization.

In conducting measurements in krypton, the plasma reactor shown in figure 5.1(a) and the electrical circuit shown in figure 5.2 were used. In a pressure range from 50 to 125 Torr, the current was decreased from abnormal glow mode. Figure 6.2 shows end-on visible images at these pressures. As the current was decreased, the cathode area covered by the discharge decreases with a significant drop in visible emission. The decreased area did not show filament structures, which are seen in xenon, at any pressure as confirmed in figure 6.2. Although an unidentified bright spot can be seen at 125 Torr (see figure 6.2 at 0.40 mA), this is considered to be a localized corona due to surface roughness of the anode. Further decrease of the current extinguished the plasma.

6.1.3 Observation with parallel-plate geometry (ITO cathode)

Self-organized patterns were observed in xenon with the same electrical system shown in figure 5.2 but with a parallel-plate geometry as shown in figure 5.1(c). The pattern emerged when the current was decreased to a critical value in the measured pressure range from 50 to 150 Torr. The patterns monitored from the anode side are shown in figure 6.4. Although the appearances in the parallel-plane geometry quite resemble those in CBL geometry, a difference can be confirmed: a break of axisymmetric arrangement is seen where one (figure 6.4 (a)) and two (figure 6.4 (b)) filaments persist after extinction of other filaments. These arrangements were not observed in CBL discharges. Spatiotemporal fluctuations emerge at pressures of 125 Torr or higher accompanied by a higher voltage (figures 6.3 m,q). This feature can also be observed in CBL discharges.

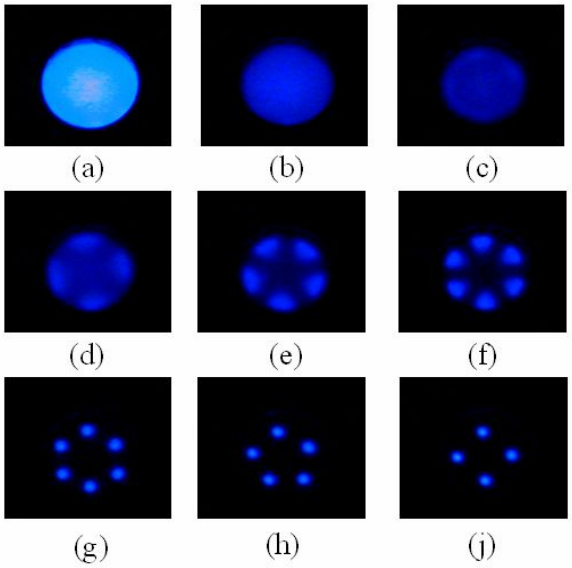

Figure 6.1. Sequential end-on visible images of CBL discharges in xenon at a pressure of 75 Torr, a gap distance of d = 250 μm, and a cathode diameter of D = 750 μm obtained by reducing the current. (a) 0.9 mA; (b) 0.23 mA; (c) 0.17 mA; (d) 0.17 mA; (e) 0.17 mA; (f) 0.16 mA; (g) 0.11 mA; (h) 0.092 mA; (j) 0.073 mA. All plasma configurations are stable except state (c) where an oscillatory behavior was observed.

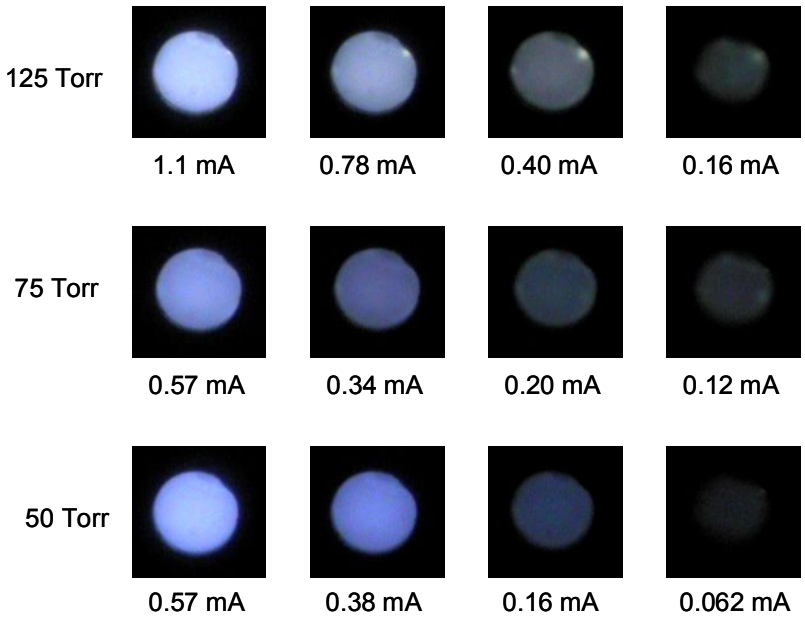

Figure 6.2. The end-on observations of discharges in krypton at 50, 75 and 125 Torr.

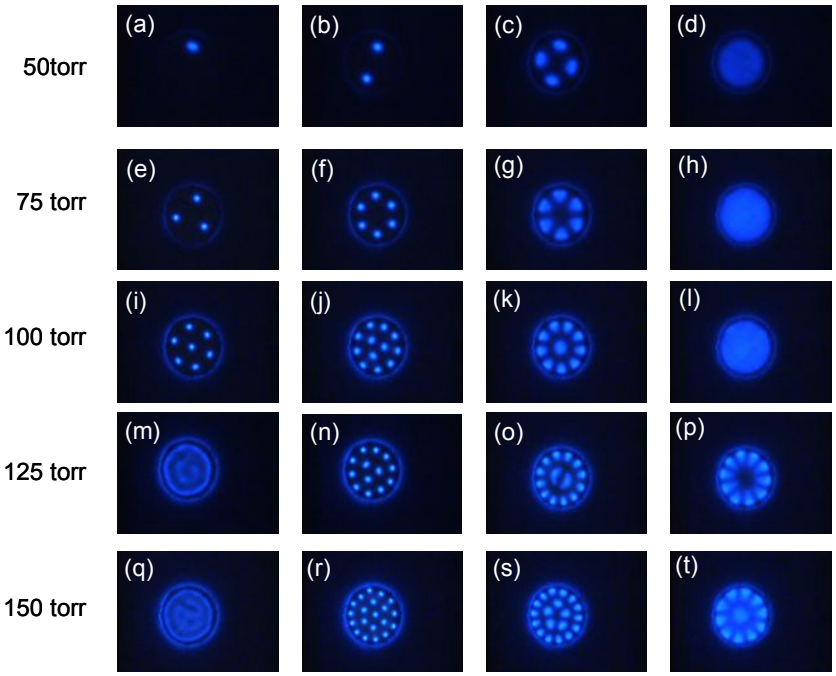

Figure 6.3. The appearances of the self-organization at (a) 0.020 mA, 292 V; (b) 0.035 mA, 284 V; (c) 0.086 mA, 303 V; (d) 0.096 mA, 347 V; (e) 0.051 mA, 252 V; (f) 0.11 mA, 258 V; (g) 0.168 mA, 301 V, (h) 0.231 mA, 331 V; (i) 0.110 mA, 249 V; (j) 0.211 mA, 257 V; (k) 0.261 mA, 287 V; (l) 0.300 mA, 323 V; (m) 0.211 mA, 256 V; (n) 0.239 mA, 248 V; (o) 0.331 mA, 275 V; (p) 0.367 mA, 304 V; (q) 0.239 mA, 247 V; (r) 0.347 mA, 239 V; (s) 0.471 mA, 273 V; (t) 0.541 mA, 303 V.

6.2 I-V CHARACTERISTICS

6.2.1 Xenon discharges

For the measurement of current-voltage (*I-V*) characteristics, four pressures were selected: 50, 75, 100 and 150 Torr. This is because one can expect more pronounced self-organized patterns in the low pressure range in comparison with the result by Moselhy *et al.* (2004). In their study, the operation at higher pressures of 400 and 760 Torr provided less defined self-organization.

The result for each pressure was acquired by sweeping the current from ~1 mA to 0.07 ~ 0.25 mA while the oscilloscope recorded the current and the voltage. Figure 6.4 shows the resultant *I-V* curves with alphabets on the curve for 75 Torr, corresponding to visible images in figure 6.1.

At a pressure of 75 Torr, when the current is decreased, the discharge changes from an abnormal glow discharge (figure 6.1(a)) into a normal one (figure 6.1(b)). The voltage, as shown in figure 6.4, approaches a constant value of approximately 360 V. The diameter of the plasma shrinks (figure 6.1(b)), but the discharge is still homogeneous. With further reduction of current, a transition from a homogeneous into an inhomogeneous, but well organized plasma, diffuse mode, is observed (figure 6.1(d)). The self-organization starts with its peripheral area splitting into four or five filaments at 75 Torr. The corresponding *I-V* curve is located in the transition from (c) to (d). The diffuse mode is characterized by an increase in the number but decrease in size of plasma filaments at an almost constant current but with decreasing voltage. The onset of discharges in the confined mode follows the last diffuse mode (f) without changing the number of filaments, with a drastic decrease of the voltage of around 20 V. The confined

mode with a smaller number of the filaments (figure 6.4(g), (h), (j)) accompanies a constant voltage with decreasing current. A remarkable behavior of the *I-V* characteristics was observed at the transition from (g) to (j): the oscilloscope shows jumpings of *I-V* curve exhibiting disconitnuities with a sampling rate of 100 Hz as shown in figure 6.4.

The current density (figure 6.5) was obtained by dividing the total current by luminous area in the visible, i.e., the diameter of the luminous area in each filament in confined modes was measured to be 80 to 100 μm. Although this is a rather bold assumption, it provides an estimate of the mean current density. This calculation indicates that the current density in the diffuse and the confined mode increases with decreasing current. The bifurcation at j = 50 mA/cm^2 (point (c)) corresponds to the onset of self-organization.

The number of filaments and their distribution is not only dependent on the current but also on the pressure (figure 6.6). In both confined and diffuse modes, the filaments can form multiple-shell structures (Schoenbach *et al.* 2004) when their number exceeds 7. In the diffuse modes, the number of filaments increases monotonically when the current decreases, whereas confined modes show the opposite behavior. The number of filaments in the confined mode is linearly dependent on current I as shown by the dotted line in figure 6.6. The current per filament in this mode is constant and has a value of ~20 μA. The diameter of the plasma reactor also determines the number of filaments. A reactor with a radius r = 300 μm at low pressures (50 to 62 Torr) allowed single-filament operation. This effect will be explained in detail in section 6.5.

6.2.2 Krypton discharges

Using the same electrical circuit and plasma reactor as in section 6.2.1, an electrical measurement was carried out simultaneously with end-on observation as presented in section 6.1.2. Figure 6.7 shows the *I-V* characteristics at 50, 75, and 125 Torr in krypton. The voltage resulted in a monotonically increasing function of current without an abrupt change in the voltage.

6.2.3 With parallel-plate geometry in xenon

The measurement by the use of the parallel-plate geometry shown in figure 5.1(c) was simultaneously conducted with the optical measurement presented in section 6.1.3. The *I-V* characteristics with parallel-plate geometry resulted in curves analogous to those in CBL discharges. The sustaining voltages were found to be slightly lower, e.g., the onset of self-organization at 75 Torr corresponds to 340 V and 360 V for parallel-plate and CBL geometry, respectively.

A feature that differentiates the *I-V* characteristics between the two geometries is asymmetric distribution of the filaments (figures 6.3(a) and (b)) at a low pressure (50Torr) and low currents. Such asymmetry never occurs in CBL discharges. The sustaining voltages (282 and 293 V) with the asymmetric pattern were found to be higher than the lowest (280 V), generating another branch in *I-V* characteristic at point X in figure 6.8. Similar increases of voltage near the extinction of the plasma can be also seen at higher pressures, 125 and 150 Torr, with circular structures shown in figures 6.3 (m) and (q). But this can also be observed with an increase in the voltage in CBL discharges as well; see figure 6.4 in which there is an increase at 0.2 mA, 150 Torr.

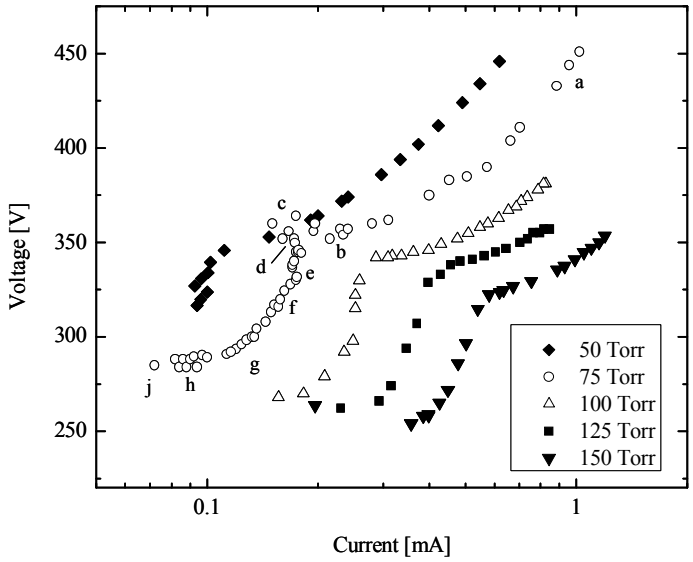

Figure 6.4. Typical *I-V* characteristics at 50, 75, 100, 125 and 150 Torr. Other parameters are d = 250 μm, and D = 750 μm. Each letter in the diagrams represents a different pattern corresponding to the pictures shown in figure 6.1. The self-organization occurs for currents of less than I = 0.18 mA.

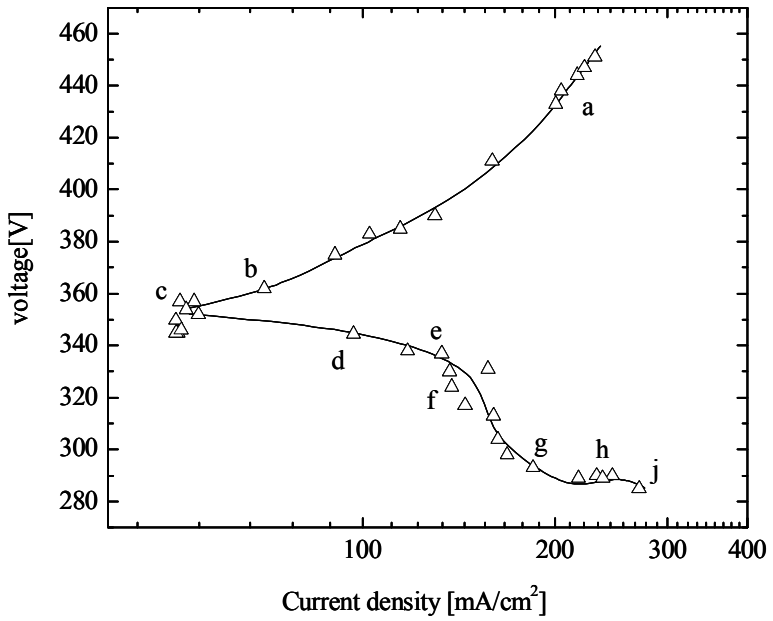

Figure 6.5. Typical *j-V* characteristics at 75 Torr, d = 250 μm, and D = 750 μm. Each letter in the diagrams represents a different pattern corresponding to the pictures shown in figure 6.1. The current density j in the diffuse and confined modes was obtained by dividing the total current by the area defined by the emission in the visible. It is denoted by $j = I/A$ with A being the area of the entire cathode, ~ 50 mA/cm^2 at 0.18 mA.

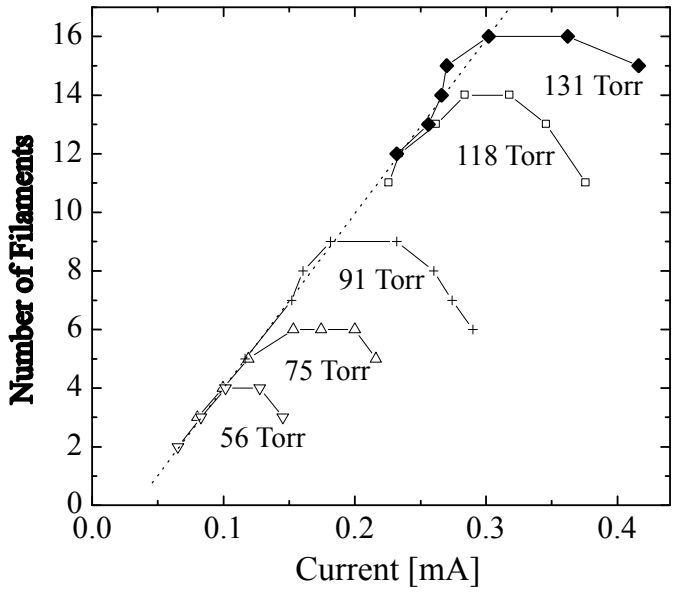

Figure 6.6. The number of filaments as functions of current and pressure for a discharge in xenon with $D = 750$ μm, $d = 250$ μm.

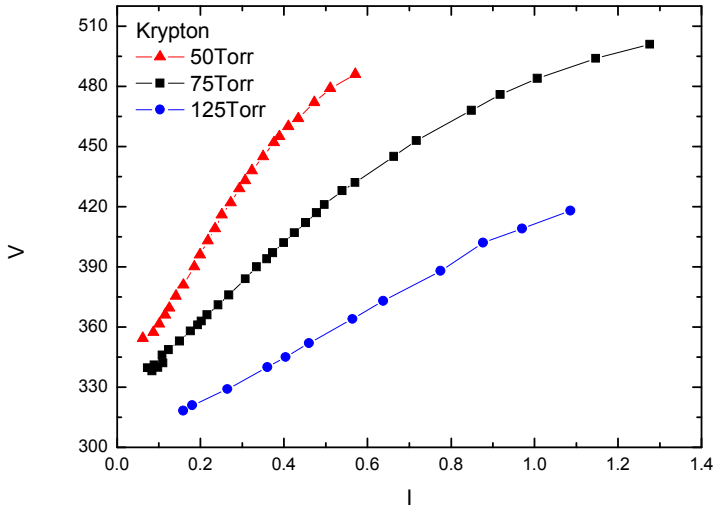

Figure 6.7. The *I-V* characteristics of discharges in krypton with a reactor configuration shown in figure 5.1(a).

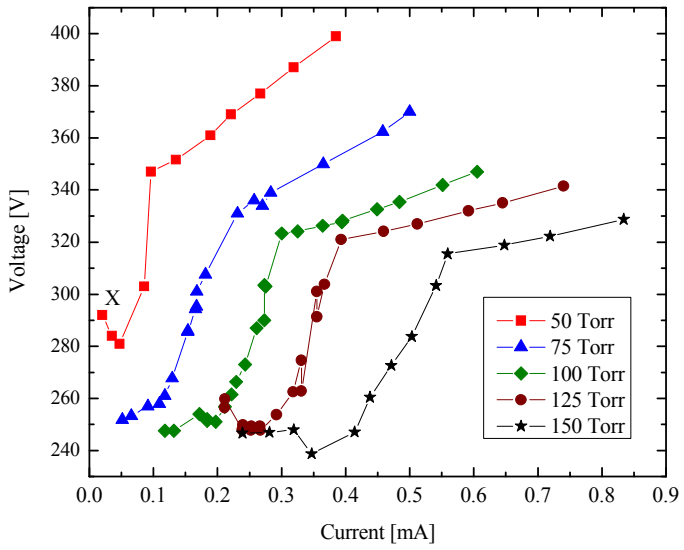

Figure 6.8. The measured *I-V* characteristics in xenon with a reactor configuration shown in figure 5.1(c). The point "X" locates the operating point where a branch of *I-V* curve is obtained as described in section 6.2.3.

6.3 MEASUREMENTS IN THE VUV

6.3.1 Spectral profiles

Figure 6.9 shows the measured xenon spectra under four pressures: 75, 150, 200, and 250 Torr. The ordinate of the graphs represents the relative intensity of the emission after a correction for the transmittance of the viewports. The most distinctive broad emission centered at 172 nm arises from excimers that are mainly produced by three-body collisions, expressed by

$$Xe^* + 2Xe \rightarrow Xe_2^*(\Sigma_3) + Xe \quad (6.1)$$

$$Xe^* + 2Xe \rightarrow Xe_2^*(\Sigma_1) + Xe\,. \quad (6.2)$$

This emission was found to increase with increasing pressure, as seen in figure 6.9. The production rate of excimers via three-body collisions is given by $kN_{gas}^2N_{xe*}$ where k = $4.4\times10^{-32}(300/T_g)^{1/2}$ and $2.0\times10^{-32}(300/T_g)^{1/2}$ are the rate coefficients for equations 6.1 and 6.2, respectively (Eckstrom *et al.* 1988). N_{gas} and N_{xe}^* are the number densities of the xenon atoms and the excited xenon atoms, respectively. Hence, the rate of excimer formation is proportional to the square of N_{gas}, and may be reflected in the measurement. Another distinct emission peak around 150 nm accounts for the first continuum (0^+_g). This continuum is shifted to the red at higher pressures (figure 6.9(a)). On the other hand, it comes closer to the resonance line (147 nm) as the pressure is decreased to 75 Torr (figure 6.9(d)). Provided the pressure is less than 75 Torr, the emission tends to show a sharp peak mainly from the resonance line. This trend is typically seen in xenon discharges (Almed *et al.* 1998, Bonifield 1980). Therefore, the shifted emission, just below 150 nm at 75 Torr in this experiment, is considered to be a result of lightly coupled xenon atoms with a larger vibrational radius (1^{st} continuum). If the pressure is much less

than 75, e.g., 20 Torr, the coupling becomes weaker, giving rise to another appreciable detection in the atomic spectrum at 147 nm, due to photon release from the resonance state $^3P_2$ to the ground state (Wieme *et al.* 1981).

6.3.2 Excimer intensity at 172 nm with molybdenum cathode

In order to evaluate the intensity of excimer emission using the VUV camera, a measurement with the calibrated detector was conducted as described in section 5.2.4. This process enables the relative intensity information from the VUV camera to be converted into an absolute value.

The dependence of excimer emission and internal efficiency on the current at fixed pressures is plotted in figures 6.10(a) and (b) with corresponding *I-V* characteristics shown in figure 6.10(c). The absolute intensity of excimer emission (figure 6.10(a)) represents the optical power in the VUV region radiated from the plasma. The reactor achieves a maximum radiant power density of 1700 mW/cm^2, which is obtained by dividing the radiant power by the area (1/4 × 0.075 cm × 0.075 cm × π). The maximum power density is higher than conventional DBD excimer lamps, e.g., by a factor of >17 when compared with CiMax-2000 Ushio, typically delivering 50 - 100 mW/cm^2 in spite of a long lifetime of 1000 hours (Ushio AMERICA, Inc.).

A remarkable result is the existence of an optimum point for absolute power density; the excimer emission is not a simple increasing function of the current. The maximum peak shifts to a larger value as the pressure is increased (figure 6.10(a)). As expected, the peak shifts further to higher currents if the current is increased up to 760 Torr (Moselhy *et al.* 2004). When the current is too low to fill the entire cathode area, the absolute power is low due to the small emissive area. The maximum peak corresponds to

the minimum current at which self-organization can exist. A further increase in current leads to an increase in the total area occupied by filaments, whereas the excimer emission cannot retain a maximum value, i.e., it is decreasing with increasing current. Note that this falling characteristic of the emission versus current continues while the plasma is in abnormal glow phase. In other words, the decrease of the current from abnormal glow to normal glow causes an increase of the emission of the excimer. The relation between the excimer intensity and the self-organization will be discussed later in section 7.3.

The internal efficiency is given as P_{out}/P_{in} where $P_{in} = VI$ is the input power and P_{out} is the absolute intensity given by data in figure 6.10(a). The efficiency profile in figure 6.10(b) can be readily understood with the following explanation: although the intensity profiles show a peak, the efficiency profile resulted in a monotonically decreasing function of the current. Although the output power is low at the low current regimes, input power can be extremely low such that the ratio P_{in}/P_{out} is high.

6.3.3 Dependence of Excimer Intensity on Cathode Material

Choosing different cathode materials allows us to vary the secondary emission coefficient, γ, of the cathode. Aiming for higher excimer emission performance, copper, aluminum, and titanium are used as the cathode material, in place of molybdenum. Conventionally, refractory materials are chosen for the cathode material, but other cathode materials can be tried if the current is limited such that the cathode material does not reach its melting point. Thus, the discharge current was limited to 2 mA, which is twice that of normal glow at 250 Torr. The UV intensities were measured using the same procedure as in section 6.2.2. In order to give the same surface smoothness, each foil,

with a thickness of 100 μm, was polished with an 800 grit sandpaper and the surface was cleaned with methanol.

The result of this measurement is shown in figure 6.11. A distinct difference can be seen when using aluminum as the cathode, yielding a higher excimer profile at most of the currents than any other material. In particular, the highest detection, at 0.8 mA, with the use of aluminum recorded 2200, larger than that using molybdenum by a factor of three. A comparison of intensities with respect to radial position is shown in figure 6.12 with the case of I = 0.8 mA. No well-defined self-organization was observed in the VUV or the visible with any discharge from any material at 250 Torr as seen in the views from the ICCD camera. Sustaining voltages are comparable regardless of the cathode material. The highest voltage at 0.8 mA was 247 V using aluminum. Other voltages at 0.8 mA were as follows: copper 231V, molybdenum 237V, and titanium 235V.

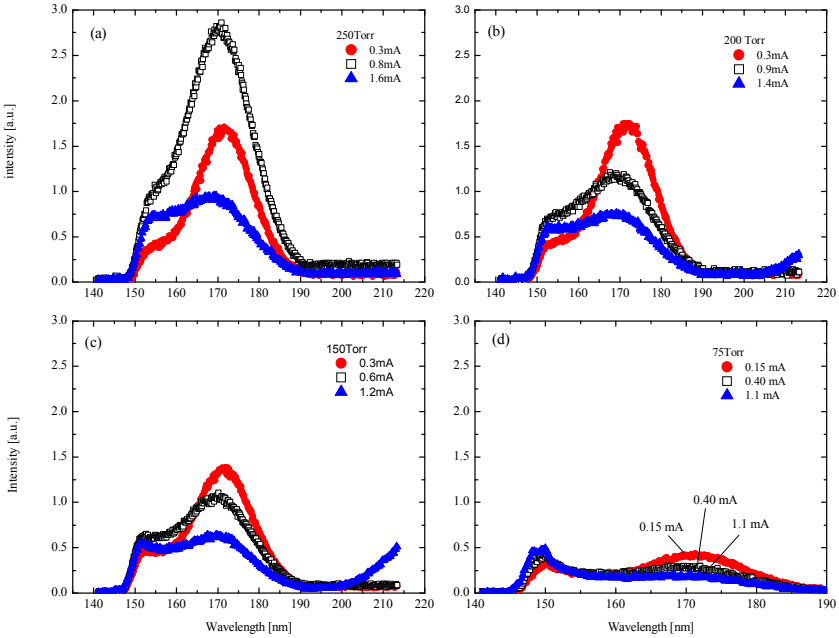

Figure 6.9. Spectroscopic data for four sets of pressures in xenon: (a) 250Torr; (b) 200 Torr; (c) 150 Torr; (d) 75 Torr.

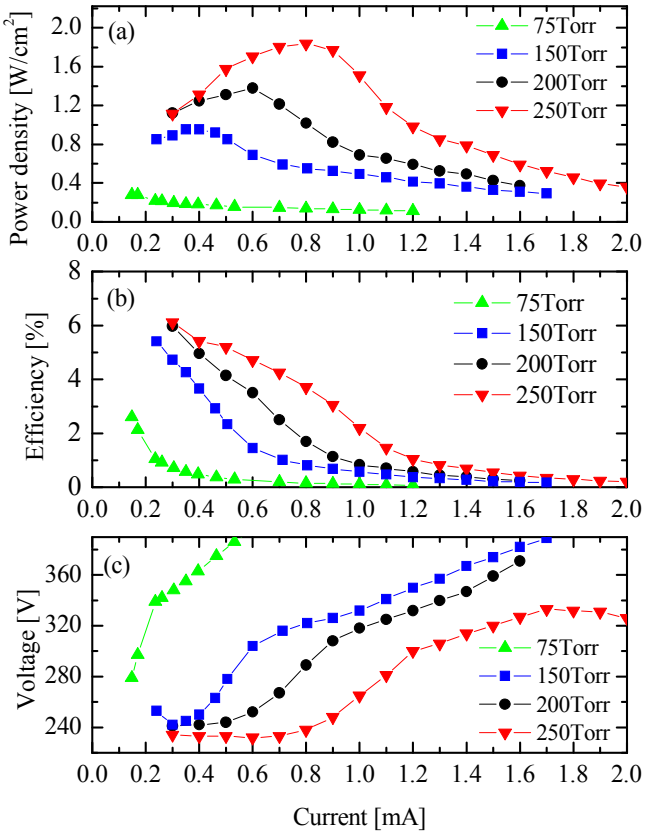

Figure 6.10. (a) The power density of excimer at 172 nm irradiated from a CBL discharge whose diameter is 750 μm. Molybdenum was used as a cathode. (b) The efficiency is given by the absolute intensity divided by electrical energy input to the plasma. (c) The corresponding *I-V* characteristics are shown.

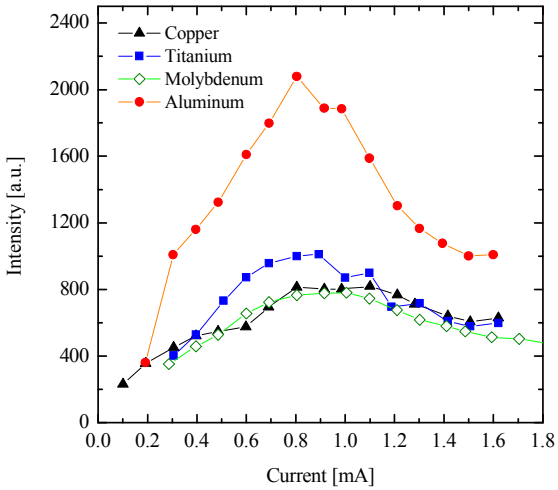

Figure 6.11. The comparison of intensities of excimer radiation with different cathode materials. The pressure is fixed at 250 Torr at which no self-organization was observed from the views by the ICCD camera.

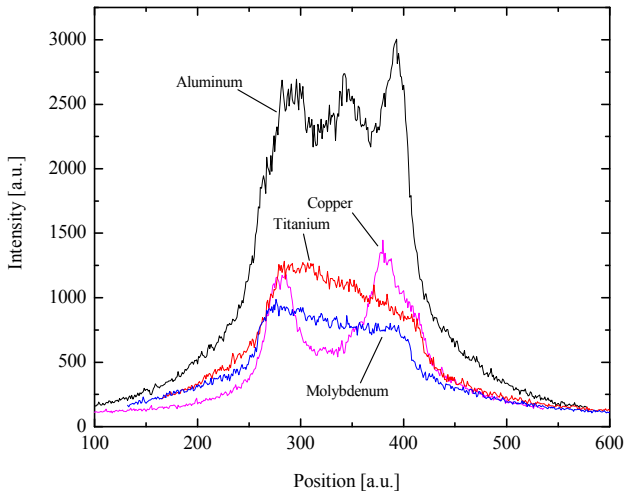

Figure 6.12. The intensity information as a function of radial position. The radius of the anode opening is 750 μm. The pressure is at 250 Torr. Although patterns appear with the use of aluminum and copper, they are not regular structure.

6.4 MEASUREMENTS IN THE VISIBLE AND NEAR INFRARED

6.4.1 Spectral profiles

Emissions in the visible and the near infrared (NIR) in xenon discharges are mainly from high-lying excited states Xe^{**} to excited states Xe^{*}. Spectroscopic measurements were carried out from 400 to 840 nm to give a comprehensive understanding of the relative population of excited states of xenon. This measurement has another motivation with respect to self-organization. As reported in section 6.3.2, the experiment obtained larger excimer emissions with the self-organized regimes than with the abnormal glow regimes. If this result is due to more frequent ionization in the self-organization, the profile in the visible and NIR should show the same tendency. Therefore, the OES measurement was implemented at 75 Torr with a current range of 0.11 to ~1 mA in which the regimes of self-organization is included.

Absolute intensities for three wavelengths, 823.1, 828.0, and 482.9 nm, versus current at 75 Torr have been obtained. The spectrometer (SpectraPro-500i) was used for measuring relative intensities of the selected wavelengths. The sensitivity profile of the spectrometer was corrected using a xenon arc lamp whose spectral distribution is given by the manufacturer. FWHM of these wavelengths were recorded and then calibrated with the detector SEL008.

Three atomic spectral lines were chosen in the visible and NIR as shown in figure 6.14. The two transitions, 823.1 and 828.0 nm from the second excited states (Xe^{**}) to excited states (Xe^{*}), predominate among emissions from 400 to 840 nm. This characteristic can be seen in most glow discharges in xenon (Carman and Mildren 2003). The intensity information at 823.1 and 828.0 nm has relevance to the populations of

excited states in $2p_6$ and $2p_5$, respectively. This is understood by considering the emission coefficient ε_{21}, which is proportional to the emission intensity of a transition from upper state 2 to lower state 1,

$$\varepsilon_{21} = \frac{1}{4\pi} h \nu_{21} A_{21} N_2 \tag{6.3}$$

where h is Planck's constant, A_{21} is the spontaneous emission coefficient, ν_{21} is the frequency of the photon, N_2 is the population density in excited states 2. Considering that absorption from Xe^* to Xe^{**} is small enough, the measured intensity gives rough information on the population of Xe^{**}. From this standpoint, we shall regard the emissions at 823.0 and 828.1 nm as merely an indication of the population in $Xe^{**}(2p_6$ and $2p_5)$, and will not distinguish them from each other. The emission at 482.9 nm (Xe I) provides one of the prominent peaks among those responsible for the blue color of CBL discharges in xenon. This emission is due to a transition from upper state $Xe^{**}(3p_7)$ to $Xe^*(1s_4)$ as shown in figure 6.13. Since the relaxation of $Xe^{**}(3p_7)$ takes place mainly by radiation, this emission can also be simply interpreted as the indication of the population of the upper state.

Unlike VUV emission at 172 nm showing a decreasing function of the current as reported in the preceding section, the emissions of these three spectra resulted in increasing characteristics with increasing current as shown in figure 6.14. For a comparison, the intensity profile of 172 nm as a function of the current is shown in the same figure. It must be noted that at the lowest currents (~0.1 mA) where self-organization appears, the total emissive area decreases to 10% of the area with homogeneous plasmas. The decrease in the intensities of these spectra in the visible and the NIR is therefore likely due to the decrease in the emissive area.

As for homogeneous plasmas, e.g., I > 0.2 mA at 75 Torr, the intensity information directly reflects the rate of the spontaneous emission without taking the emissive area into consideration. In the low current regimes near $j = j_n$, the populations in the upper states in $2p_6$, $2p_5$ and $3p_7$ are extremely low while the excimer intensity achieves its maximum. Since the population in these upper levels can affect the population at the metastable state $1s_5$, we may speculate that the population at $1s_5$ is not high enough at $j = j_n$ in spite of giving a strong emission at 172 nm. A more detailed discussion will be given in section 7.3.

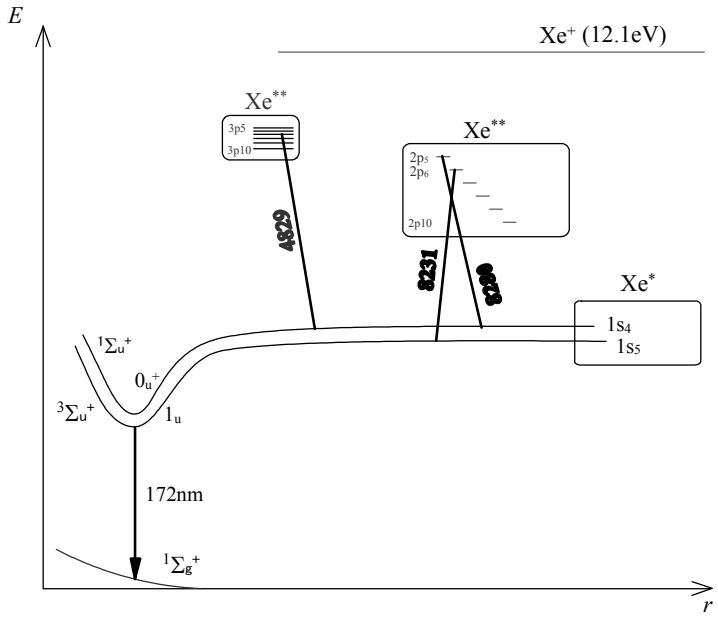

Figure 6.13. An energy diagram for a xenon atom. The abscissa denotes intermolecular distance and the ordinate electron energy.

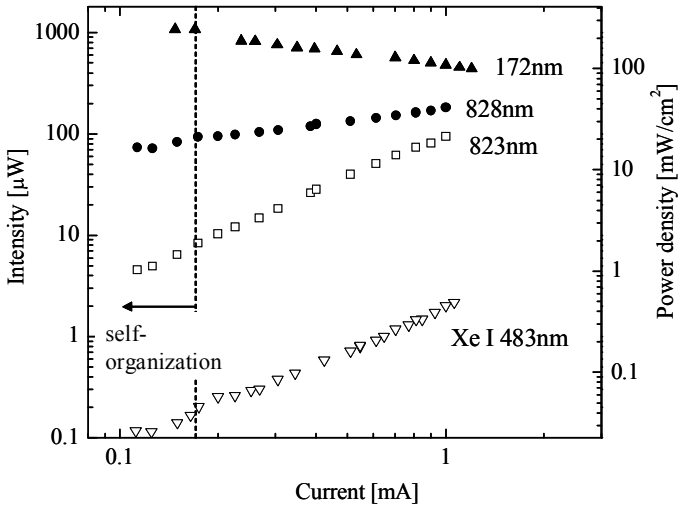

Figure 6.14. The comparison of absolute intensities for photon emissions at 75Torr. The self-organization occurs generally <0.15~0.20 mA.

6.5 SINGLE-FILAMENT OPERATION

Reduction of the current and the pressure gives fewer filaments as shown in figure 6.6, but a single filament was not obtained in CBL discharges with the anode opening of 0.75 mm. Reducing the size of the anode opening was expected to cause a reduction in the number of the filaments. A plasma reactor with an opening size of 300 μm in diameter was therefore fabricated. The configuration of the reactor is shown in figure 5.1(a). The visible and the VUV images at 50, 62, 75, and 100 Torr are shown in figures 6.15(a) to (h). The sustaining voltage drops at the onset of the self-organization as shown in figure 6.16(c). The magnitude of the voltage was found to exhibit a similar profile to that of the reactor with a 750 μm anode opening as seen in the comparison with figure 6.10(c). When the current is reduced, the self-organization is observed at all pressures. Among the four tested pressures, the confined single filament is observed only at 50 and 62 Torr. The emergence of the confined single filament follows an instable mode as shown in figures 6.15 (a.3) and (c.3) where a "wobbling" plasma can be seen. As shown in figure 6.16(a), the power density in the confined filament indicated a lower value (~300 mW/cm^2 at 50 Torr) than diffused mode (~400 mW/cm^2 at 50 Torr) mainly because in the confined filament mode the bright area is constricted in the center and the peripheral dark area does not contribute to the excimer emission. The internal efficiency at 75 Torr does not exceed 3% which is comparable to the case with a 750 μm opening (~3%), indicating that reducing the size of the reactor in diameter does not enhance the efficiency.

One can compare the mean values of excimer intensity in one filament among single-filament (62 Torr with D = 300 μm) and multi-filament modes (3 filaments at 75

Torr with D = 300 μm and 6 filaments at 75 Torr with D = 750 μm). The intensities turned out to be in the same range ~ 200 counts. The result leads to the conclusion that the brightness per filament is independent of the number of filaments and the area of the cathode opening.

In summary, it is possible to obtain a single filament by varying the pressure and current when the cathode area is reduced.

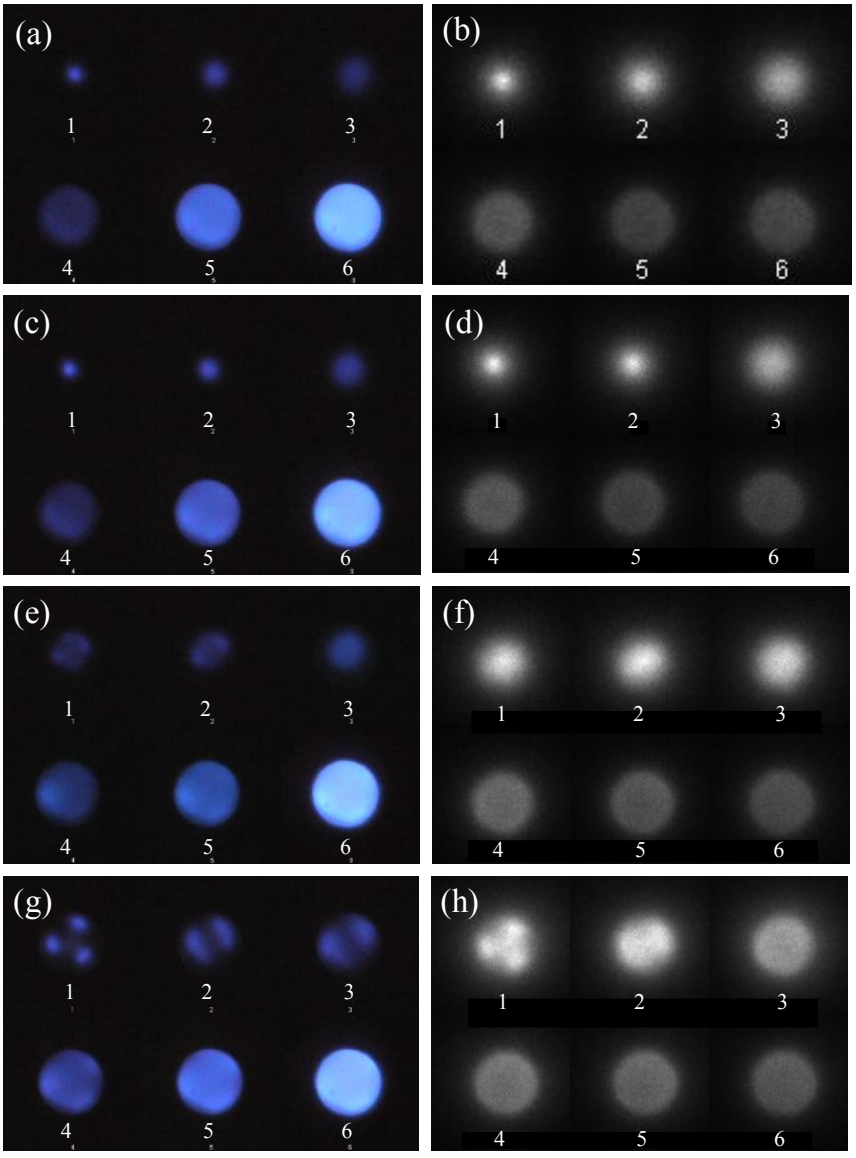

Figure 6.15. End-on observation of stationary plasmas at (a) 50 Torr in the visible, (b) 50 Torr in the VUV, (c) 62 Torr in the visible, (d) 62 Torr in the VUV, (e) 75 Torr in the visible, (f) 75 Torr in the VUV, (g) 100 Torr in the visible, (h) 100 Torr in the VUV. Six pictures of discharges belonging to each alphabet are sorted by its current in ascending order. The top left (number 1) corresponds to the lowest current.

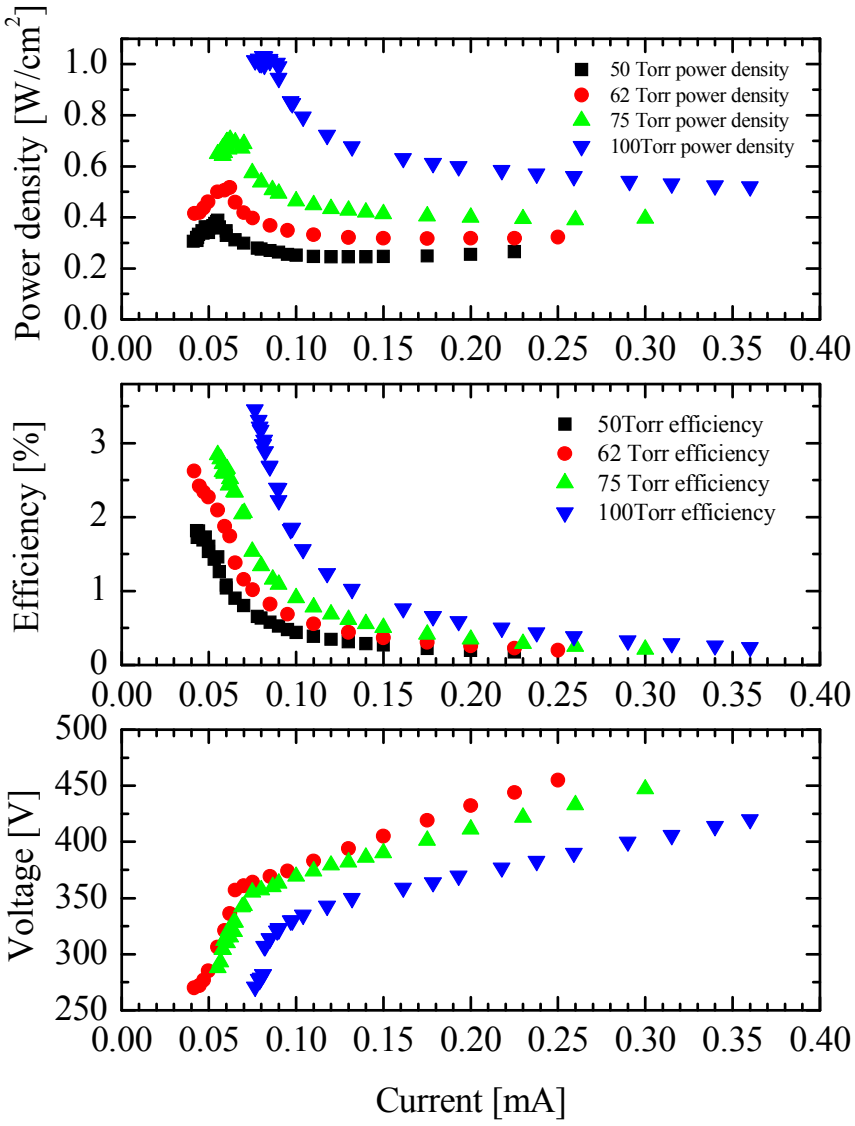

Figure 6.16. (a) The power densities, (b) the efficiencies, and (c) the *I-V* characteristics of single-filament operation.

6.6 SIDE-ON OBSERVATION

In order to study the filament structure in the axial (normal to the cathode surface) direction, side-on images of the discharge were taken through a 250 μm thick transparent dielectric separating cathode and anode. Such a side-on image is shown in figure 6.17 for a homogeneous xenon discharge at I = 0.37 mA and p = 64 Torr. A dark space is seen above the cathode, which one associates with the cathode fall region. The length of the dark space is denoted as d_c. The bright glow adjacent to the cathode fall is the negative glow region, which serves as a radial current path to the circular anode. The side-on measurements allow us to determine the cathode fall distance dependent on the current and pressure. By using similarity laws for the normal cathode fall, it also provides us with information on the secondary emission coefficient, γ, for the normal cathode fall region, and the cathode fall voltage over a limited range of current. We employed a polished tungsten foil with a thickness of 100 μm for the cathode for this side-on observation except for figure 6.17.

Figure 6.18 shows the results of cathode fall measurements in the normal glow mode of a xenon CBL discharge over a pressure range from 30 Torr to 140 Torr. The cathode fall length increases with decreasing pressure as expected. The normal glow mode was determined by recording the end-on image of the discharge at a given pressure with the current as variable parameter. We define the onset of the normal glow to be when the plasma begins to shrink, e.g., point (c) in figure 6.4 is set as at the normal glow in the case of 75 Torr. The current value at a normal glow mode divided by the entire cathode area (0.0375 cm × 0.0375 cm × 3.14 = 0.0041 cm^2) is defined as the normal glow current density, j_n.

Varying the current at a fixed pressure of 75 Torr allowed us to observe the development of patterns as seen in figures 6.18. The abnormal glow discharge provides a thick and bright negative layer. The current reaching up to 1 mA does not allow us to define the cathode fall thickness due to the expanded glow region near the cathode surface. When the current is decreased from the normal glow mode, the plasma becomes unstable and oscillatory (also confirmed by the negative differential conductance, shown in figure 6.4 at this transition), increasing the distance of the negative glow from the cathode plane without noticeable perturbations in the direction normal to the cathode. The cathode fall thickness recorded its highest value at 75 μm with a thinned negative glow layer as shown in figure 6. 19(a). A stable discharge with point symmetric patterns in the "diffuse mode" (figure 6.19 b) emerges when the current is lowered. With the current being further decreased to 0.092 mA, confined patterns appear as shown in figure 6.19(c).

The change of the cathode fall thickness with current is summarized in figure 6.20. The cathode fall length increases with decreasing current in the range of the abnormal glow, reaches a maximum at the normal glow mode, and decreases again when the discharge turns into the self-organization mode.

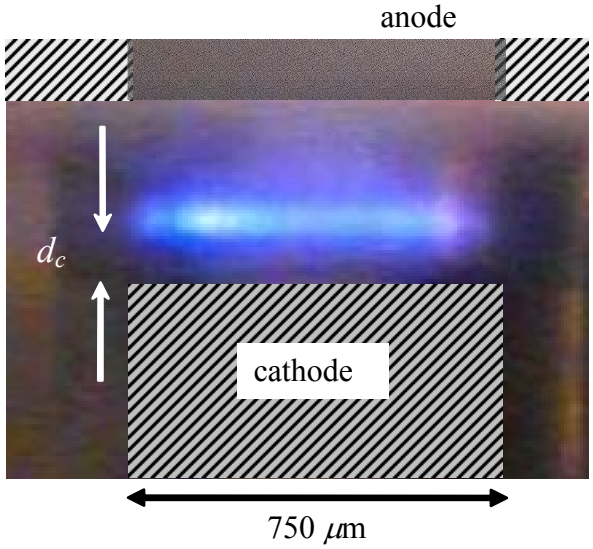

Figure 6.17. Side-on observation of a CBL discharge (D = 750 μm, d = 280 μm, I = 0.37 mA, and p = 64 Torr). A tungsten wire is used as cathode.

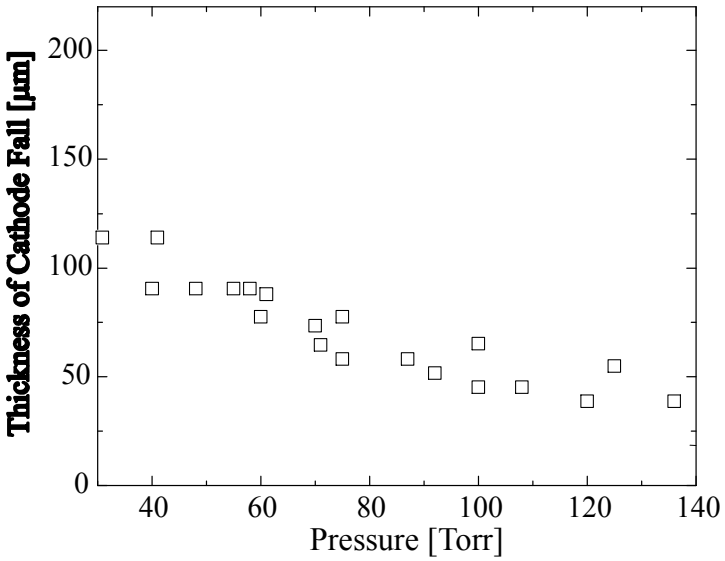

Figure 6.18. Measured normal cathode fall thickness depending on pressure.

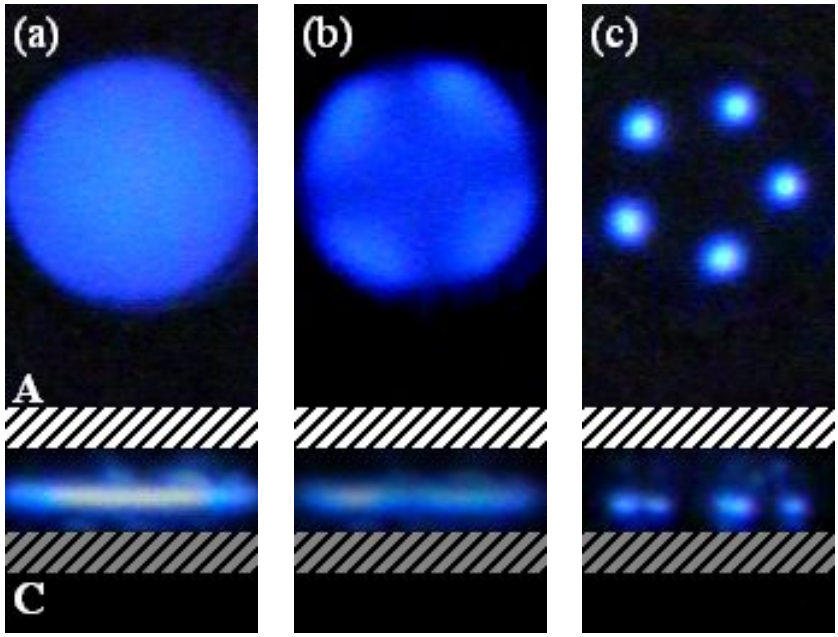

Figure 6.19. End- and side-on observations of discharges in a normal glow mode, diffuse, and confined mode are shown in (a), (b) and (c), respectively at p = 75 Torr. (a) d_c = 70 μm, I = 0.224 mA ($j \sim j_n$), V = 346 V. (b) d_c = 70 μm, I = 0.179 mA, V = 336 V. (c) d_c = 50 μm, I = 0.092 mA, V = 279 V.

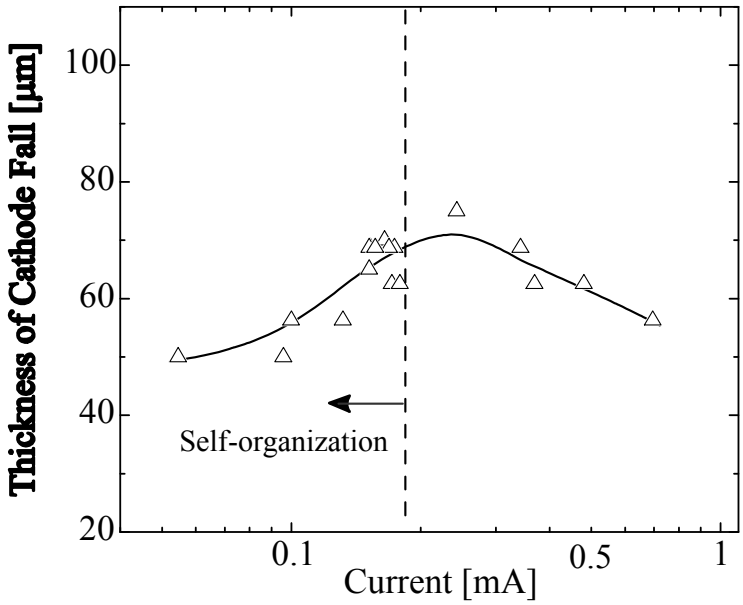

Figure 6.20. The observed cathode fall thicknesses, d_c, as a function of current. The self-organization is exhibited when I ~0.15 to 0.2 mA.

6.7 TEMPERATURE MEASUREMENT

In order to obtain information on the cathode temperature, temperature measurements were performed on the back of a very thin molybdenum cathode (thickness: 25 μm) using a micro-thermocouple. Choosing a cathode with a thickness of less than the diameter of the plasma filaments and a thermocouple with a very small tip diameter (13 μm), compared to the cathode diameter of 750 μm, allowed us to detect spatial fluctuation of the temperature with a spatial resolution of 13 μm, which is smaller than the filament diameter, 80~100 μm. This allows us to determine whether the cathode temperature is elevated at the position of the filaments and if thermal emission of electrons at these locations may play a role in the cathode fall voltage and thickness.

The results of these measurements at 75 Torr are shown in figure 6.21. The temperature at the back of the cathode was found to be independent of position and linearly dependent on the current. At the onset of the self-organization at a current of $I \sim$ 0.2 mA, the cathode temperature is 305 K, barely higher than room temperature (297 K).

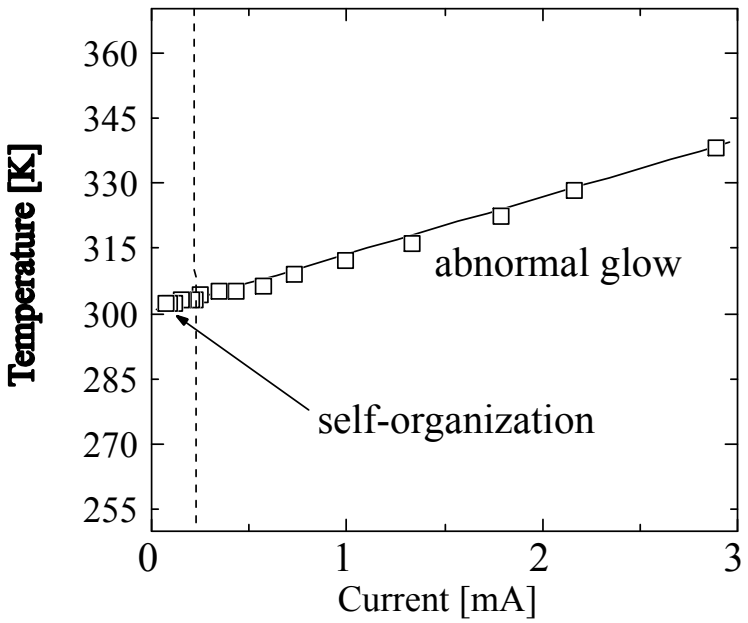

Figure 6.21. The observed temperature as a function of current *I*. The self-organization is exhibited when $I < 0.2$ mA.

CHAPTER VII

DISCUSSION

7.1 CATHODE FALL PARAMETERS

Measurements of the cathode fall in the normal glow mode allow us to determine the secondary emission coefficient, γ. Assuming that only ion impact determines the electron emission from the cathode, the normal thickness of the cathode fall (the length of the dark space on the cathode as a normal glow is realized), d_n, can be expressed (Cobine 1958) as

$$d_n = 3.76 \frac{\ln(1+1/\gamma)}{Ap}, \tag{7.1}$$

where p is the pressure and A is the inverse of the product of pressure and mean free path for ionization. For xenon, A = 26 (cm Torr)$^{-1}$ (Lozansky 1975). Knowing the cathode fall length, d_n, and the value of A for a given gas pressure allows us to obtain a value for γ. Equation 7.1 is thus rewritten with respect to γ as

$$\gamma = \frac{1}{\exp(d_n Ap / 3.76) - 1}. \tag{7.2}$$

Figure 7.1 shows the calculated cathode fall lengths denoted by dotted lines, using equation 7.2, for various values of γ, superimposed on the experimental values (figure 6.18). The gas temperature was assumed to be constant at room temperature. An optimum matching between the experimental values and theoretical curves is obtained for γ = 0.03 for a pressure range ~60 Torr to 140 Torr. The value of γ is comparable to that measured by Hagstrum (1956) for xenon-tungsten (γ = 0.025).

A deviation toward larger γ is seen for lower pressures (< 50 Torr) as seen in figure 7.1. A consideration was made on the gas temperature effect to explain the discrepancy between the calculated and measured γ in the low pressure range. The coefficient A in equation 7.1 is an empirically derived constant that has been widely used in studies for glow discharges (Raizer 1998). Equation 7.1 assumes p is a constant. However, the gas density N should be used rather than p since rate equations for collision processes which involve gas atoms scale with N, not with p. The gas density N can be obtained from the ideal gas law $p = NkT$ with T the gas temperature. The measurement for figure 7.1 was conducted with various values of j_n as shown in figure 7.2. Since j_n is dependent on p, the cathode fall length at higher pressures with higher current densities may suffer a decrease of N due to an increased T. This correction will "push up" the theoretical values in figure 7.1 at higher pressures. The nominal γ for xenon-tungsten may therefore result in higher values such as $\gamma \sim 0.07$.

Knowing d_n and the normal current density, j_n, allows us to calculate the cathode fall voltage, V_n, for the normal cathode fall (Cobine 1958):

$$V_n = \sqrt{\frac{j_n d_n^{\,3}}{4\varepsilon_0 K^+ (1+\gamma)}} \tag{7.3}$$

where $K^+ = 0.4$ cm^2/(V·s) (Varney 1952) is the ion mobility at the cathode at 75 Torr and ε_0 the permittivity in free space. Note that this equation is not sensitive to γ provided γ is in the range described in the preceding discussion. For a pressure of 75 Torr, the value of V_n is evaluated to be 320 V, a rather high value, but expected for the low value of γ (Kushner 2005). This method was used to determine the cathode fall voltage in the range where we see the onset of self-organization. In the condition of not moving too far from

the normal cathode glow region, we expect to obtain information on changes in the cathode fall voltage. Using this approximation, what we see is a substantial decrease in cathode fall voltage with reduced current (figure 7.3) from 320 V to approximately 240 V, when the current is reduced from 0.25 to 0.15 mA.

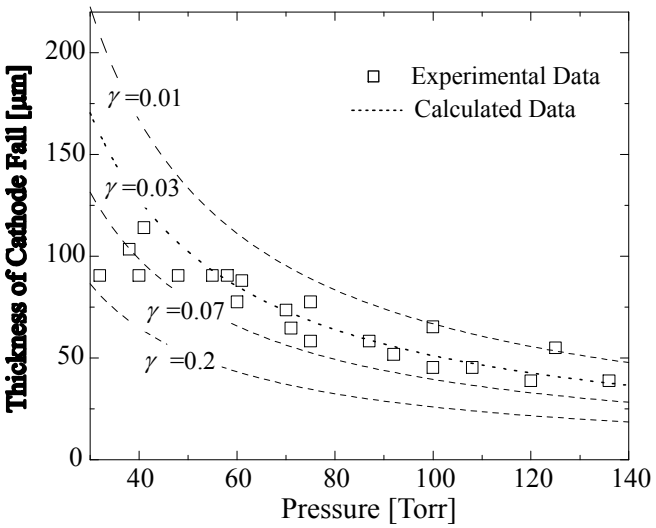

Figure 7.1. Experimental (squares) and calculated (dashed curves) thickness of cathode fall.

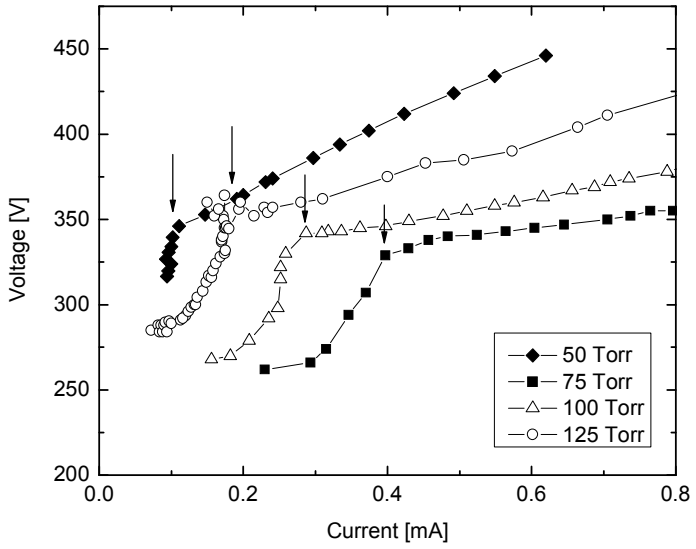

Figure 7.2. *I-V* characteristics of the CBL discharges are shown with arrows indicating j_n. The cases of only 50, 75, 100, 125 Torr are displayed.

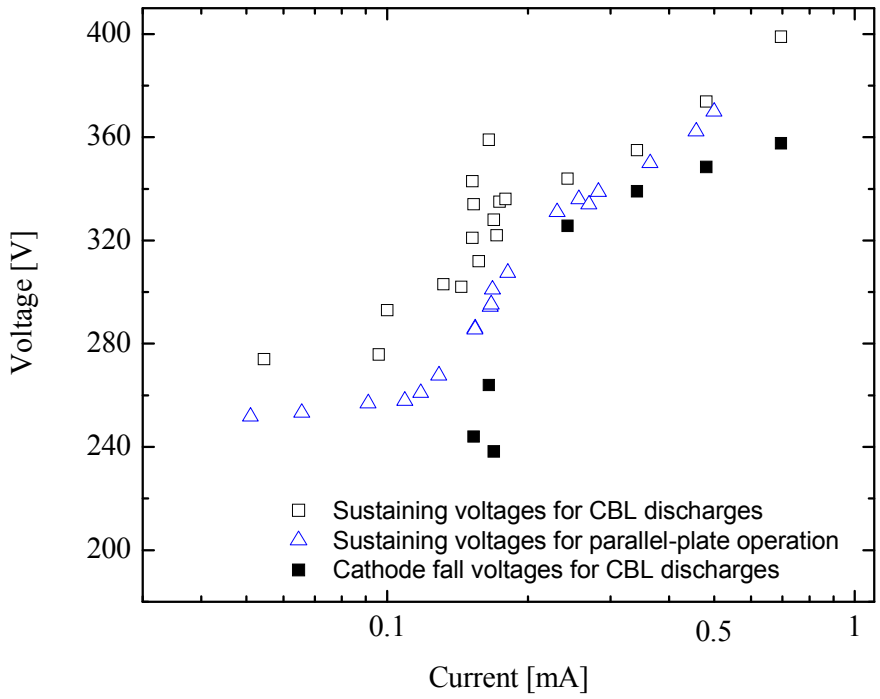

Figure 7.3. Experimental values of the sustaining voltage and the calculated cathode fall voltage. The discharge conditions are D = 750 μm, p = 75 Torr, d = 250 μm (CBL geometry), d = 280 μm (parallel-plate geometry).

7.2 OPERATION WITH DIFFERENT REACTOR GEOMETRY OR CATHODE MATERIAL

A confined single filament is considered a candidate as an element for an integrated VUV light source. Enhanced excimer radiation from the single filament is required for this application. Experiments in section 6.2.1 indicated the feasibility of single-filament operation under a particular condition with low p and I as shown in figure 6.6. However, in order to obtain a single filament, the reactor with the opening diameter of D = 750 μm requires low pressures, less than 50 Torr, at which the plasma easily extinguishes without self-organization. Therefore, the radial dimension was reduced to D = 300 μm. A confined single filament was obtained at both 50 and 62 Torr, as reported in section 6.5. Reducing the anode opening diameter to 300 μm does not change the relation of the current to number of filaments in accordance with figure 6.6; the typical current at 50 and 62 Torr with D = 300 μm resulted in 0.04~0.05 mA with single-filament self-organization. The dotted line in figure 6.6 indicates that 0.05 mA gives a single filament. This fact suggests that the results shown in figure 6.6 can be applicable irrespective of the size of the anode opening.

The radiative power density and its internal efficiency with D = 300 μm was 0.7 W/cm^2 and 2.8 %, respectively, for 75 Torr. The power density exceeded that of the larger geometry (0.3 W/cm^2 when D = 750 μm) by a factor of more than two. However, a comparison of the intensities showed that emission of excimers per filament is not likely to depend on the size of the anode opening. From this fact, the following is concluded: the difference of the power density between D = 300 μm and 750 μm arises mainly from the filling factor of the filaments. The reason is seen from the following discussion. The

opening area is changed by a factor of 6.25 ($6.25 = (750/300)^2$) when D is changed from 300 μm to 750 μm. On the other hand, the emission from the filaments changed only by a factor of ~2 since the number of filaments are 3 and ~6 for D = 300 μm and 750 μm, respectively. A simple calculation results in the power density for D = 300 μm can be $6.25/2 \approx 3.1$ times larger than D = 750 μm. The measured power density for D = 300 μm is less than twice as high as that for D = 750 μm. Actual comparisons must be made with emissions from areas adjacent to filaments, but the simple analysis clearly shows that reducing the size of the anode opening such that the filling factor of the self-organization becomes larger would yield a higher power density.

The reason for the decrease in radiative power density in the confined mode compared to that in the diffused mode is associated with the area of radiation, not with a change of excimer production or removal rate. As seen in figures 5.8(b,d,f,h), the brightness at the confined filament is larger than that in the diffused mode. For example, a factor of 1.5 is obtained from a comparison between figure 6.15 (b) 1 and 3. This fact indicates that more efficient excimer production or slow excimer removal is realized in the confined self-organization.

Aluminum as a cathode material recorded an outstanding excimer emission compared with other cathodes (figure 6.12). The reason could be the secondary emission coefficient, but no values for γ are known from past measurements with respect to aluminum in xenon, to the best of our knowledge. Aluminum is not known as a material that provides an enhanced secondary emission of electrons. For example, γ in H_2 is given by Hale (1939) where γ is given by a function of $E/p > 1300$ (V/cm/mmHg). For a discharge with V_c = 340 V, p = 75 Torr and d_c = 100 μm, γ is 0.02 based on the

assumption that $E = V_c/d_c$. This is not higher than that for a xenon discharge with a molybdenum cathode, evaluated as $\gamma = 0.03$ in section 7.1.

7.3 RADIATIVE EMISSION IN THE VUV – THE DEPENDENCE OF EXCIMER EMISSION ON THE CURRENT

The measurement of excimer intensity in the CBL configuration described in section 6.3.2 resulted in a peak near normal glow or diffused self-organization and a decrease as the current increases in the abnormal glow (figure 6.10). The experiment using the smaller plasma reactor (D = 300 μm) also showed the same tendency as reported in section 6.5. The following discussion deals with the mechanism for the result, maximum excimer intensity associated with the regimes where the current density is the smallest (normal glow). It must be noted that argon has a tendency similar to xenon, with the peak of excimer intensity near normal glow but without self-organization in the CBL configuration (Moselhy *et al.* 2004). There are two possible interpretations: one attributes the reason to an increase of the population of excited xenon Xe^* while the other attributes it to an enhancement of a rate coefficient for Xe^*.

If we assume that the peak of excimer intensity near normal glow is correlated with an increased population of excited states Xe^*, the population should scale with the excimer intensity. The emission spectroscopy in the visible and near infrared was thus conducted to assess the validity of this assumption. The experiment, however, resulted in low emissions from upper excited states Xe^{**} to lower excited states Xe^* at lower currents, indicating small populations of both Xe^{**} and Xe^* even for a large excimer intensity. This result does not support the assumption. The reason for the low emission from Xe^{**} to Xe^* can be attributed to a decrease of current, which is responsible for the density of electrons.

The decrease of electron density near normal glow due to the decrease of the current would be harmful for the production of Xe^* as well as Xe^+.

The rate constant for production of Xe^*, however, is likely to be optimized when reaching self-organized mode from abnormal glow. Carman and Mildren (2003) have modeled the strong dependence of the rate constants for $Xe^*(1s_4)$ and $Xe^*(1s_5)$ on the electron temperature in a short-pulse excited xenon excimer lamp. Their results show that the fractional rate constant of the $Xe^*(1s_4)$ state increases and that of the $Xe^*(1s_5)$ state decreases with increased electron energy. It yields the most effective production of $Xe^*(1s_5 + 1s_4)$, which is realized at $<\varepsilon> = 3.5$ eV where $<\varepsilon>$ represents the mean electron energy. In the CBL regimes, the plasma in abnormal glow can undergo an effect of optimized production of Xe^* when approaching self-organized mode from abnormal glow, coupled with the increase of the cathode fall voltage (Zhu *et al.* 2007). The increase of the rate constant prolongs the lifetime of Xe^*, and the excimer production can consequently be accelerated. This explanation can also be applied to the case for argon.

7.4 INSTABILITY DUE TO ELECTRONIC COLLISIONAL PROCESSES IN XENON

Most instabilities giving rise to pattern formation accompany a change in the electric field in the perturbed space. For example, electronic or thermal instability develops with a change in E/N as discussed in sections 3.1 and 3.2. Hence, it is essential to identify the location or magnitude of the electric field. The following analysis, shown in section 7.4.1.1, through the measurement with parallel-plate geometry, has found that the radial electric field is not significant for formation of self-organization despite its existence in the CBL configuration. We concluded that the axial electric field remains a

candidate for one of the decisive factors. In particular, the region where the axial electric field decreases to zero is known to exhibit instability. The modeling results by Aleksandrov *et al.* (1997) suggest that the negative glow can be the region where oscillation of the current occurs due to the nonlinear relation of drift velocity to the axial electric field. In order to explain the filamentation illustratively shown in figure 7.4(a), this section presents a sequence of the causal links in the following (a)-(f) that possibly connect the occurrence of instability in the region to the formation of filaments: (a) near-zero axial electric field existing in the negative glow; (b) dominant electron-electron (e-e) collisions changing EEDF; (c) NNDC in the negative glow due to increased momentum transfer; (d) instability occurring in the negative glow (figure 7.4(b-i)); (e) formation of axial filaments during transition from abnormal to normal glow (figure 7.4(b-ii)); (f) a positive feedback of the gas temperature and the first Townsend coefficient increasing the current density; (g) arrangement of the pattern due to Coulombic repulsive force (figure 7.4(b-iii)). Of these phenomena, the first step (a) is obvious as follows: the electric field toward in the cathode fall region ($0 < z < d_c$) can be approximated by a linear function

$$E = E_0(1 - z / d_c) \tag{7.4}$$

where z is the axial distance from the cathode surface. In the negative glow, on the other hand, the axial electric field reaches a value close to zero where slow electrons are generated after inelastic collisions (Raizer 1991). Therefore, we will discuss the rest in the following sections with a view on collisions.

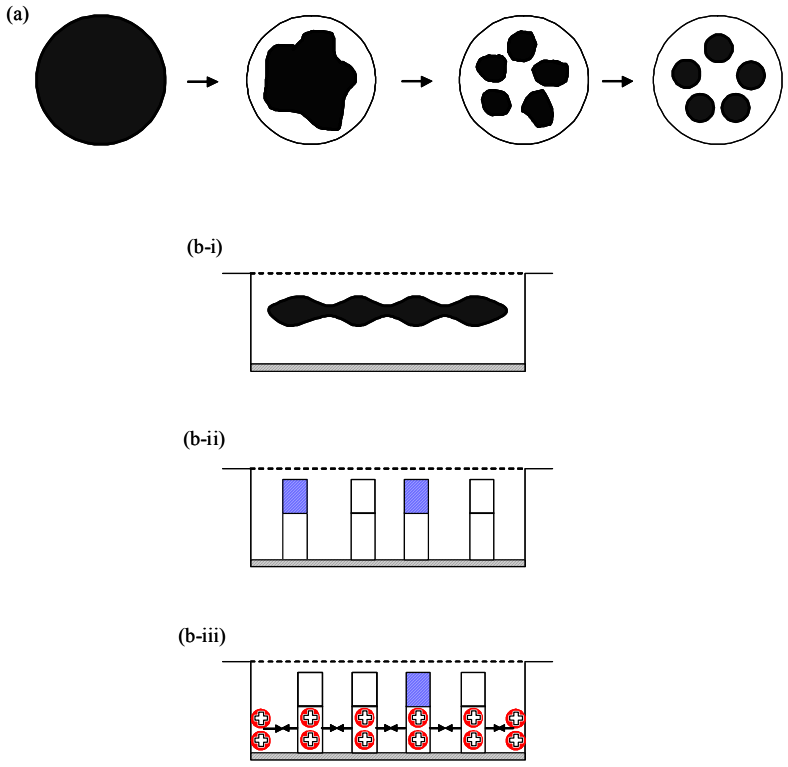

Figure 7.4. (a) Illustrations of a sequence leading to pattern formation from abnormal glow to the filamentation. (b-i) to (b-iii) illustrate phenomenological behaviors of the filaments in one-dimensional schematics: (b-i) Axial instability propagating toward the edge of the anode in (b-i). (b-ii) Filaments formed due to the instability. The hatched and blank rectangles standing on the cathode surface represent the negative glow and cathode fall, respectively. (b-iii) The Coulombic repulsive forces acting among cathode falls and dielectric wall.

7.4.1 Radial and axial electric fields

7.4.1.1 Parallel-plate configuration

The experiment described in section 6.2.3 using a parallel-plate geometry with a transparent anode was conducted to investigate whether a radial electric field plays a role in self-organization. The self-organization resulted in a similar *I-V* characteristic, structure of the filaments, and the number of the filaments to those in CBL geometry. The radial electric field on the anode was calculated with the given conductivity of the anode and the current where the self-organization arises. Using the surface resistivity of the ITO coated cathode η = 10 Ω/sq, and approximating the circular anode with a square whose width w and length l are $w = 2\pi r$, $l = r$ (r =0.0375cm), the resistance between the center to the edge of the anode is: $\eta \times l/w$ = 0.8 Ω. Assuming a critical current, 200 μA, when self-organization occurs, the voltage drop is calculated to be V = 200 μA × 0.8 Ω = 160 μV. The electric field is then 160 μV/0.0375 cm = 4.3 mV/cm. This is much weaker than the criterion, $1\sim10^2$ V/cm, which is shown in figure 3.2. We therefore concluded, with the calculation above, that no significant electric field in the radial direction exists along the anode plane of the parallel-plate geometry. V_r is thus approximated by zero when using parallel-plate geometry. Since the geometry is considered to have a negligible radial component of the electric field, it is reasonable to hypothesize that V-V_c matches the axial voltage V_a (figure 7.5) which exists in the negative glow or Faraday dark space.

The measurement of self-organization for the *I-V* curve (I < 0.15 mA) in the parallel-plate geometry resulted in obtaining a lower sustaining voltage by ~30V than that in the CBL configuration as shown in figure 7.3. We can deduce that self-organizations have a radial electric field generated in CBL configurations but shortened in the parallel-

plate geometry. The shortened current path consequently decreases the sustaining voltage in the parallel-plate operation. On the other hand, in the abnormal glow regimes where I > 0.2 mA, there was not such a large voltage difference between discharges in the parallel-plate and CBL geometry although there was some (less than 10 V). Homogeneous discharges are then considered to have a lower radial electric field which otherwise becomes prominent in the regimes of self-organization. Considering the emergence of self-organization in the parallel-plate operation as well, the shortcut of the radial current path was not decisive for the generation of self-organization. It is known that a space in those two regions, Faraday dark space and negative glow, has the lowest electric field reaching zero (Raizer, 1991). Since the criterion for the NNDC is $1 \sim 10^2$ V/cm, it is possible to have a space in the two regions where the electric field meets the value. We therefore consider that the NNDC can be initiated in these two regions.

7.4.1.2 CBL configuration

The drastic change in the calculated cathode fall voltage V_c, shown in figure 7.3, at the normal current density, j_n, indicates that a change occurred in the voltage across the anode to the interface between the cathode fall and the negative glow. The voltage, which is designated as V-V_c, is small at a current in abnormal glow but becomes larger when I < 0.18 mA as shown in figure 7.3. The region with the drastic potential drop V-V_c was considered to exist mainly in the path from the axial center of the negative glow (r = 0) to the side wall ($r = r_0$), creating an axisymmetric electric field inward the axial center. Notice, at any point in the discharge, that the following relationship holds: $V - V_c(r) = V_r + V_a$ where V_r is the radial and V_a the axial voltage as shown in figure 7.5. Provided that instability occurs due to NNDC that is discussed in section 3.2.2, an electric field on the

order of 1~ 10^2 V/cm is required at 75 Torr (figure 3.2) for the onset of the NDC. The cathode fall holds a larger electric field. Assuming a linear electric field as a function of position as shown in equation 7.4, E_0 at the cathode surface reaches 80 kV/cm. This calculation does not allow the region near the cathode surface ($z \sim 0$) to become the instable region.

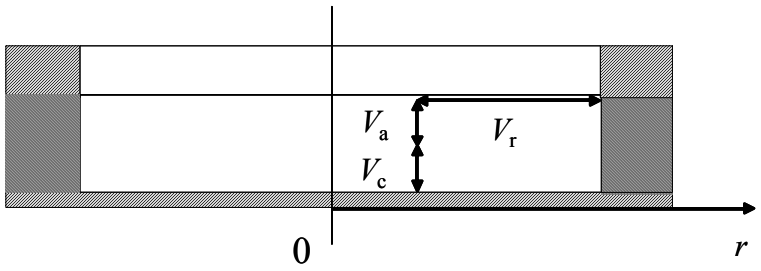

Figure 7.5. A path from a point on a cathode surface to an edge of the anode is shown in a cross sectional view of the CBL configuration.

7.4.2 The condition for the occurrence of NNDC

The e-e collision process, which was introduced in section 3.2.2, can be pronounced in CBL discharges at the onset of self-organization. As the current is decreased in the abnormal glow toward normal glow, the sustaining voltage is decreased, as found in the positive *I-V* curves in figure 6.4. This is interpreted as an indication of a decrease in the mean electron energy which reaches its minimum in the normal glow mode. Since the cross-section for e-e collisions is proportional to ε^{-2} (Aleksandrov *et al.* 1997), the situation with a lower mean electron energy is desirable for frequent e-e collisions.

Although a region exists where the electric field lies between $1 \sim 10^2$ V/cm at 75 Torr, the NNDC does not necessarily occur. The discussion by Aleksandrov *et al.* assigns a condition for the occurrence of the NNDC with respect to the ionization degree $\alpha_i = n_e/N$ where n_e is the electron number density. A degree, $\alpha_i = 10^{-6}$, is evaluated for adequate e-e collisions to occur. Micro-hollow cathode discharges, which are operated with a typical electron density of $10^{12}/cm^3$ near the normal glow (Moselhy 2002), achieve an ionization degree of $\alpha_i = 4.1\times10^{-6}$ at a pressure condition $p = 75$ Torr. Assuming that electron densities can be comparable between CBL discharges and micro-hollow discharges with the same current, it is reasonable to consider that CBL discharges also achieve analogous ionization levels that satisfy the criterion for the emergence of NNDC. In figure 7.6 the case with α_i being on the order of 10^{-6} is emphasized by the bold line.

The most serious difficulty in the experimental verification of the NDC phenomenon seems to be the high purity required for Xe because molecular gases generally have very large vibrational excitation cross sections which could also induce

NDC but with a different range of w and E/N (Kochetov *et al.* 1998). In CBL discharges, it is known that pattern formation is subject to the purity of xenon; self-organization is not observed in contaminated xenon (< 99.99 %). From these facts, the reason that self-organization is not observed in contaminated xenon can be attributed to the disappearance of NNDC in the range of the electric field due to vibrational excitation of molecular contaminants such as N_2. Note that a degradation of ionization degree α_i due to contamination of other gases can also cause a change in the NNDC, giving a similar effect.

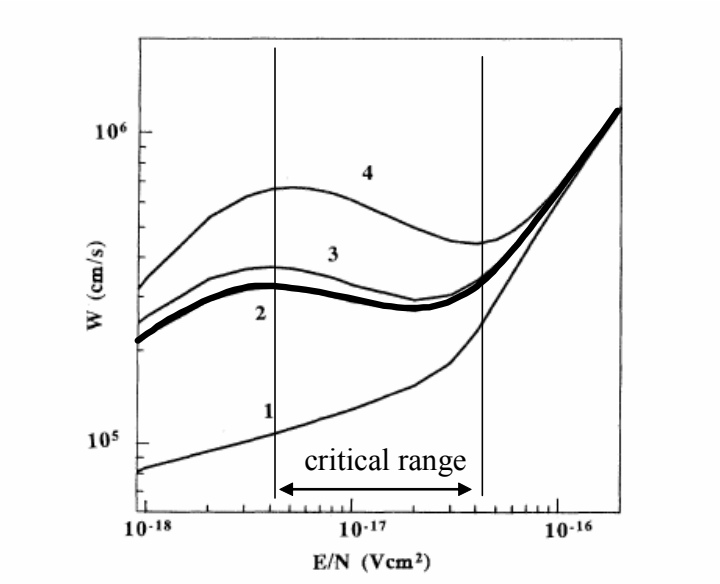

Figure 7.6. The NDC for the case of $\alpha_i = 10^{-6}$ and $\delta = 0$ is emphasized with the bold curve. Refer to figure 3.2 for the details of the other curves.

7.4.3 Consequences of NDC – the filament formation in the axial direction

A positive feedback effect is expected at the transition from abnormal to normal glow. The local current density and the electric field in the negative glow and Faraday dark space play an important role in creating deviations from equilibrium. An illustration shown in figure 7.7 depicts a positive feedback of local current density and voltage. At the position where the current density has a positive variation from the mean value, the local cathode fall voltage, υ_c, is found to be larger than the mean value of V_c (the position x = A in figure 7.7). This is confirmed by the fact that the *I-V* characteristic has a positive slope in the transition from abnormal glow to normal glow. Next, the following relationship is met as to the local voltage, υ_c: V_{total} = const. = $Ed_{ng} + \upsilon_c$, where d_{ng} is the length from the negative glow to anode. This means that the electric field E from the negative glow to anode is decreased where j remains higher than adjacent points. The positive feedback starts when E is decreased to the critical range of E/N which is shown in figure 7.6. As the electric field E is decreased, w is increased, accelerating electrons in the space. This effect then enhances the Townsend ionization coefficient α, resulting in further increase in j locally. On the other hand, a region with a negative variation of j turns out to yield a further decrease in j due to the opposite discussion. This positive feedback enables the small fluctuations in the negative glow and Faraday dark space to grow to become axial filaments.

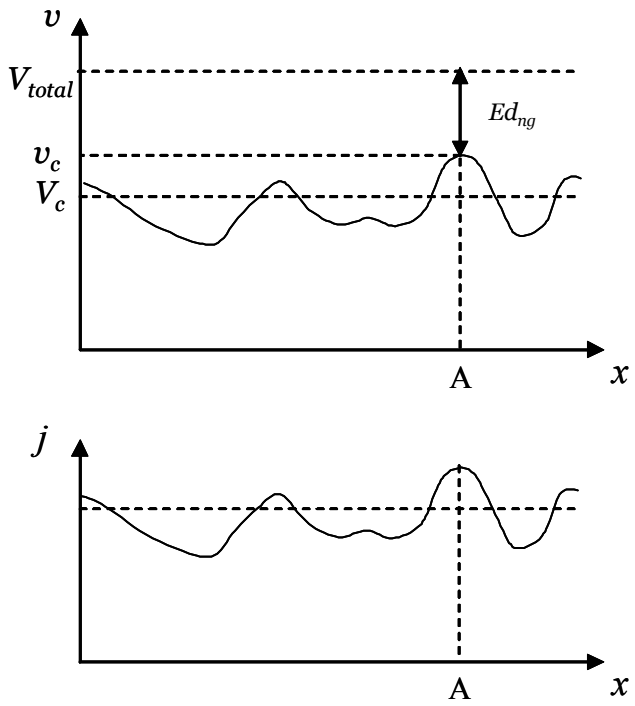

Figure 7.7. An illustration of local current density and voltage as a function of position *x* where *x* axis is parallel to the cathode surface.

7.4.4 The development of filaments due to temperature effect

The pattern formation may be developed further by another positive feedback that connects a decrease in local gas density, N, to an increase in the first Townsend coefficient, α. The following discussion explains the closed chain of the positive feedback effect.

Filaments resulting from NNDC show an increase in the local gas temperature, T. Assuming an ideal gas, the gas density, N, decreases to satisfy the constant pressure as $p = NkT$. The reduced electric field (E/N) in the filament consequently increases due to the decrease of N. The first Townsend coefficient, α, is known to be sensitive to E/N (Raizer 1991), and is a monotonically increasing function of E/N as

$$\alpha = ANkT \exp[-B(NkT/E)^{1/2}] \tag{7.5}$$

where A and B are intrinsic constants for the gas. Therefore, one finds an increase of α arising from the increase of E/N. The production of electron-ion pairs becomes more efficient, which decreases the sustaining voltage. The decrease of the voltage is seen in figure 6.4 as the positive slope in the I-V characteristic in the regimes of self-organization. The fact that the self-organization can be sustained at a lower voltage can be attributed to the more efficient production of electron-ion pairs as described above. The chain of such causal links is then expressed as

$$T\uparrow \Rightarrow N\downarrow \Rightarrow E/N\uparrow \Rightarrow \alpha\uparrow \tag{7.6}$$

where $\Rightarrow$ symbolizes the flow of the sequence, $\uparrow$ and $\downarrow$ an increase and decrease of the elements, respectively. At the last chain, an increase of α increases the gas temperature T, completing the positive feedback loop back to the first step.

Notice that an increase in the current density is an indication of the temperature increase as is presented in section 7.1.1. In CBL discharges, the increase of the current density is seen in each filament as shown in figure 6.5. The current density rises from ~50 to 280 mA/cm^2.

7.4.5 Regular pattern formation - Coulomb repulsive force

Whereas the positive feedback determines the amount of electron emission from the cathode surface, Coulomb force is assumed to be the reason for maintaining a self-organized pattern. The cathode fall is characterized by a positive space charge, creating the strong electric field near the cathode. Any filament developing in this region will therefore extend repulsive forces to neighboring cathode fall filaments. These repulsive forces are assumed to be balanced by electrostatic forces from positive surface charges at the surrounding dielectric spacer. It is supported by the fact that the current for a discharge with single filament is always approximately twice that expected for the filament alone. Figure 6.6 also indicates an excess amount of current (~0.03 mA) that is not due to filaments and is found with an extrapolation of the linear relation of the number of the filaments to the current. We consider that the excess current flows along the surface of the dielectric, forming a layer of positive charge. The surface charge at the dielectric generates a potential well in which the filaments arrange themselves based on the principle of minimum energy. The constant space charge on the inner dielectric is assumed to be evenly distributed.

Using polar coordinates, with the center of the cathode being at $r = 0$ and the radius of the opening r_0, the Hamiltonian (the sum of the electrostatic energies of the filaments) of a system which consists of n filaments, is:

$$H = q\sum_{i=1}^{n}\varphi_i = \sum_i \frac{q\lambda r_0}{4\pi\varepsilon}\int_0^{2\pi}(r_i^{\,2} + r_0^{\,2} - 2r_i r_0\cos\theta)^{-1/2}d\theta + \sum_{i\neq j}\sum_j \frac{q^2}{4\pi\varepsilon}\frac{1}{\left|\mathbf{r}_i - \mathbf{r}_j\right|}, \tag{7.7}$$

where λ is the charge density (charge/length of circumference) at the side wall, r_i is the vector from the origin to i^{th} filament, and ε denotes the permittivity of the medium. The positive charge $q > 0$ is assumed to be the same for each filament, which is treated as a point charge. The potential φ_i of a filament at a distance r_i from the center is, accordingly,

$$\varphi_i = \frac{\lambda r_0}{4\pi\varepsilon}\int_0^{2\pi}(r_i^{\,2} + r_0^{\,2} - 2r_i r_0\cos\theta)^{-1/2}d\theta + \frac{q}{4\pi\varepsilon}\sum_{j\neq i}\frac{1}{\left|\mathbf{r}_i - \mathbf{r}_j\right|}. \tag{7.8}$$

A typical potential distribution, determined by uniformly distributed charges on the side wall, but without filaments, is shown in figure 7.8.

The numerical calculation to evaluate the minimum potential with a given number of filaments was conducted for several values of space charge, λ, on the dielectric. The point charges associated with the filaments were placed at random positions in the potential well, and the potential distribution was calculated. The filaments were then moved a short distance in the direction opposite to the potential gradient. This process was repeated until a stable configuration was reached, i.e. the Hamiltonian reached a minimum value.

The calculation was conducted with the condition that the number of filaments was 1 to 8 with a one-shell structure. The result shows that the stable position of the filaments is point-symmetric around the origin of the coordinate system. Therefore, we can express the position of the filaments using the normalized distance of the filaments from $r = 0$. After normalizing the distance r by r_0, the results were compared with the experimental values at 75 Torr. Figure 7.9 shows the case of $q = \lambda\pi r_0/3$, $\lambda\pi r_0/6$, and $\lambda\pi r_0/12$. The optimum agreement with the experiment is thus obtained for $q = \lambda\pi r_0/3$. The case of a

single filament is in agreement between the calculation and the observation. Due to the axisymmetric potential well, the calculation for the single filament forces the position to be in the stable point at $r = 0$. The observation of the single filament supports this calculation. As seen in figure 6.15 (a,c), the filament is stable where $r = 0$. As for a single filament in parallel-plate operation, it is stationary in spite of $r \neq 0$, which does not apply to the result of the calculation. Another source of force is needed that competes with the Coulomb force.

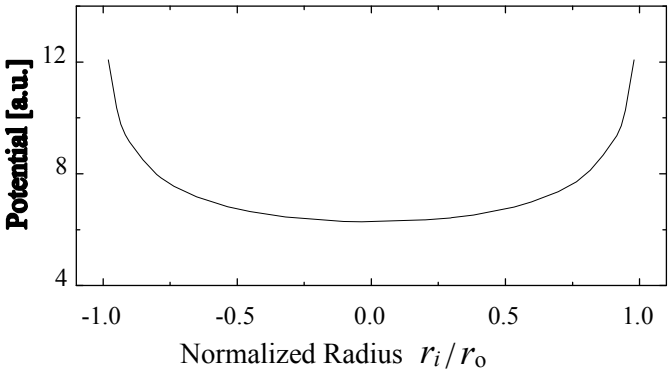

Figure 7.8. A cross-section of the potential well created by a layer of positive charges on the surface of the dielectric which separates cathode and anode.

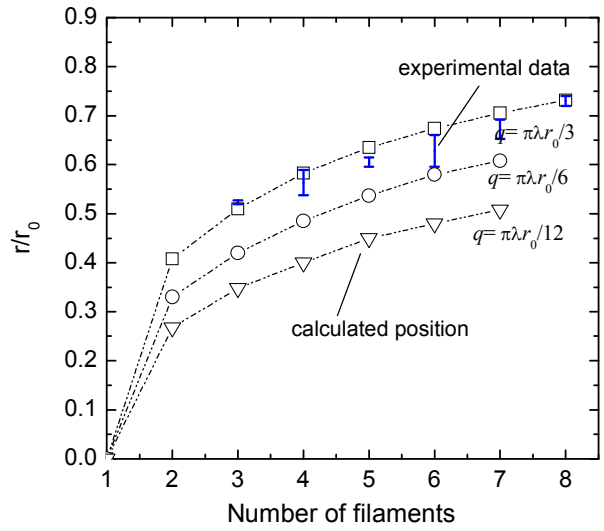

Figure 7.9. Comparison of calculated and measured values of the normalized average radii of the filament positions in a stable configuration. The measured values with error bars are based on a number of results typically shown in figure 6.1.

7.5 PATTERN FORMATION BASED ON REACTION-DIFFUSION PROCESS

7.5.1 The basic principles and the differences from the first mechanism

In this section, we attempt to explain the pattern formation by adopting generic gas discharge physics in parallel-plate geometries which has been widely and extensively studied. This approach is based on the experimental confirmation of self-organization in the parallel-plate geometry as described in section 6.2.3. Through section 7.5, the discussion proceeds with the experimentally supportable principle: self-organizations in both types of geometry are driven by the same certain effect. Note that no explanation has made a difference in the mechanism for CBL geometry from that for parallel plate geometry. Similarly, section 7.4 does not differentiate the mechanisms for both. It follows that it is easier to consider the mechanism of self-organization in the parallel-plate geometry than the CBL configuration. Furthermore, we shall make an extended conjecture, based on other pattern formations in chapter 4, that they may also be caused by the same effect. Given this point of view, we can refer to efforts and findings achieved throughout other similar systems in the past. A number of such efforts for solving the phenomena of self-organization in dc plasmas have mainly had a viewpoint on a nonlinearity of the plasma (SNDC), predicting that it is the key effect to drive instability (Korolev 1979, Benilov 1992, Radehaus *et al.* 1987, Sugawara *et al.* 2005). We hence attribute our self-organization to the SNDC as well, yet we will investigate the dynamics arising from the nonlinearity in order to explain the final state, pattern formation.

Solely considering the nonlinearity does not necessarily give pattern formation. Dc gas discharges with an SNDC often provide various phenomena including oscillation or a limit cycle of current and voltage (Hsu *et al.* 2003). Therefore it is necessary to

emphasize a certain effect for a proper modeling, leading to an explanation for self-organization. We consider that an interchange of charged particles parallel to the cathode plays a significant role in pattern formation, i.e., transverse diffusion and drift. The diffusion process in the negative glow, combined with local reproduction of charged particles via ionization and the distribution of axial electric field, is essential to describe the phenomenon. A heuristic but analytical approach will be given toward reaction-diffusion equations with respect to the variations of local current density, j, and voltage, υ. In contrast to the first mechanism, this approach relies on the resultant equations, and the consequence, including pattern formation, depends merely on the equations. Furthermore, unlike the first mechanism, e-e collisions, Coulombic force, or the temperature effect of neutral particles is not employed in this scenario. Hence, basic equations, such as Poisson's equation and continuity equations for electrons and ions, mainly govern the kinematics of those charged particles.

7.5.2 Identification of SNDC and causal links leading to pattern formation

The aim of the discussion in this section, is to analyze the dynamics of the variation of the current density, j, and the voltage, υ, away from an equilibrium point where nonlinearity takes place. Assuming a homogeneous distribution of the current density and the voltage, we subsequently hypothesize a small fluctuation in both. The dynamics are examined to verify whether or not the system is driven into a catastrophe of the stationary state and a succeeding stabilization effect resulting in pattern formation. Therefore, the corresponding phenomenon examined in the observed discharges will be the transition from the homogeneous state shown in figure 6.1(c) to the first pattern

formation (diffuse mode) shown in figure 6.1(d). The transition from diffuse mode to confined mode will not be discussed.

Because we will analyze the S-shaped NDC, it is very important to identify the proper type of discharge phase with which the instability leading to self-organization manifests. Section 2.1 reminds us of the two negative characteristics, C-D (transition from Townsend to glow) and F-G (glow-to-arc transition) in figure 2.1. Noting the magnitude of the operating current, the transition from Townsend to normal glow takes place ordinarily at 10^{-6}~10^{-4} A, while the glow-to-arc transition occurs at 1~10 A in a common discharge (Roth 1995, Korolev *et al.* 1998). The experimental results in this thesis therefore would favor the case of the transition from Townsend to normal glow.

A peculiarity of a typical *I-V* curve when reaching SNDC can be designated as a discontinuity which is shown in figure 7.10(a). See references to typical *I-V* curves presented by Lieberman *et al.* (1994) and Roth (1995) where they give a discontinuity in a representative *I-V* curve for dc gas discharge physics. It follows that CBL discharges may also exhibit a discontinuity in the *I-V* characteristic as shown by the dashed line and the black circles in figure 7.10(c). The corresponding *j-E* curve for CBL discharges may have a negative characteristic which is shown in figure 7.10(b). Based on the above assumption, we will focus on the discharge regimes where the intersection of the unobservable *j-E* curve and the load line, d_{cll}, is positioned in the negative characteristic (7.10(b)) while the operating point of the *I-V* curve is still on the end of the positive slope, as indicated by T in figure 7.10(c).

The causal links for the pattern formation are as follows: (a) The local abnormal glow enters a phase that exhibits SNDC. (b) Since the operating point determined by the

external circuit is instable, the local j and v can deviate from the operating point, allowing diffusion and drift parallel to the cathode surface. (c) The total stability is met where the transport, production, and removal of the charged particles balance.

In order to mathematically express the causal links above, the following methodology was attempted. Firstly, this nonlinear relation of j to v was written as a polynomial form expanded to the third order. Secondly, a set of reaction-diffusion equations was obtained from continuity equations and Poisson's equation. It describes local variations of j and v. Finally, a numerical calculation was conducted to obtain two-dimensional pattern formations with respect to j and v. The time for forming fluctuation with a wavelength of 100 μm which is seen in CBL discharges, was calculated.

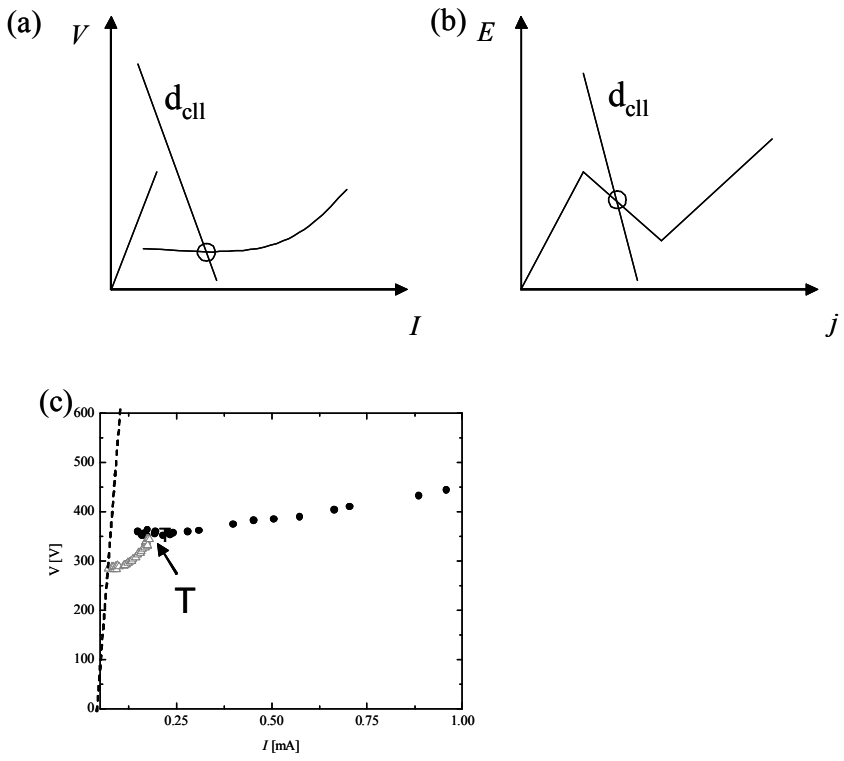

Figure 7.10. The qualitative curves of (a) *I-V* and (b) *j-E* for a typical discharge possessing SNDC. The graph (c) is taken from figure 6.4, and the gray dots in (c) denote the regime where the current is measured as a result of summation of inhomogeneous and homogeneous currents. The dashed curve is artificially added to have an analogy with (a). The transition point from the homogeneous status to diffused self-organization is denoted by T.

7.5.3 Nonlinear and linear layer in the CBL discharges

Before modeling the discharge, we introduce a definition of the discharge areas depending on the behavior of j and v, following Radehaus (1990). If v linearly responds to j, the discharge layer is called linear. On the other hand, a nonlinear layer exhibits a nonlinear relation between j and v. It is possible to approximate the nonlinear relation by a polynomial form expanded to quadratic orders or more.

The CBL and parallel-plate discharges are also composed of a nonlinear and linear layer. The decrease of sustaining voltage as the current increases, Townsend-to-normal transition, is caused in the cathode fall region where charge multiplication plays a role. Since this region is responsible for the major change in the sustaining voltage characteristic including SNDC in the *I-V* curve, we consider this layer to be the nonlinear layer. The others, the negative glow, the Faraday dark space, and the anode fall in the CBL discharges are considered a linear layer where j is proportional to v. The consideration of the positive column is therein omitted because CBL discharges operate without any positive column.

The dimensions of the nonlinear and the linear layer, a and b, are determined so as to describe the case of CBL discharges. The thickness of the nonlinear layer is set as a, which is the thickness of the cathode fall. The linear layer has a thickness of b. Therefore $a \sim 75$ μm and $b \sim 175$ μm hold for a typical CBL discharge at 75 Torr. We will follow the behavior of j and v at the interface between the nonlinear and linear layer.

7.5.4 Modification to the reaction-diffusion equations

Now it is of interest to analyze the relationship of j and v at the interface. In order to derive the relation of j to v, one needs to be concerned first with the number density of

electrons and ions, n_e and n_i, respectively, and the electric field E. The variables j and υ are derived from Poisson's equation, continuity equations, and conservation of magnetic field including displacement of the current. These equations were coupled, nondimensionalization was carried out, and we obtained, from the procedure described in Appendix A:

$$\frac{\partial j}{\partial \tau} = D_j \Delta j - f(j) + \upsilon \tag{7.10}$$

$$\frac{\partial \upsilon}{\partial \tau} = D_\upsilon \Delta \upsilon - pj - q\upsilon \tag{7.11}$$

with the variables and constants listed in Appendix A. The fluctuation component away from the dc component (j^*, υ^*) is denoted by (j, υ). The evolutions of υ and j are described as time derivatives in the left hand sides using a scaled time τ. These two variables υ and j represent a variation of the voltage and current as functions of position and time at the interface between the cathode fall and the negative glow. The meaning of equation 7.10 is interpreted as follows: The nonlinear curve of j and υ at Townsend-to-normal transition essentially is the criterion for the sustainable discharge. If there is a deviation, it causes a local increase or decrease of the current density. Equation 7.11 accounts for the temporal response of the voltage. The right hand acts as though it is the external circuit. Nonlinearity exists in the first equation as $f(j)$, which reflects reactions such as ionization, excitation, or recombination in the cathode fall region and the interaction of the charged particles and the cathode surface. Provided $\upsilon = f(j)$ is satisfied, υ and $f(j)$ cancel each other out in the right hand side of equation 7.10. This is the case at all positions on the interface between the nonlinear and linear layer when the plasma is in a stationary state. In other words, the curve $\upsilon = f(j)$ corresponds to the well-known j-V

characteristic up to abnormal glow (cf. section ABCDE in figure 2.1). Note that the set of equations is different from that of Radehaus *et al.* (1990). This system has a form of Turing instability as opposed to the bi-stable system in the model of Radehaus *et al*.

7.5.5 Development of the model

Careful consideration must be used when dealing with the nonlinear term $\upsilon = f(j)$. The curve $\upsilon = f(j)$ does not necessarily match the *I-V* curve which can be expressed as $V = g(I)$ although there may be a qualitative resemblance. The curve $\upsilon = f(j)$ represents a relation satisfied within an infinitesimal distance while the *I-V* characteristic is obtained as a result of an integration over the entire discharge width. In addition, $\upsilon = f(j)$ describes a relation at the interface of the nonlinear and linear layer, not between electrodes.

We employ an approximation of the nonlinear relation of j and υ for the sake of simplicity using a Taylor series as

$$f(j) \equiv a_0 + a_1 j + a_2 j^2 + a_3 j^3 + O(j^4) \tag{7.12}$$

where a_0, a_1, a_2, a_3, and $O(j^4)$ are specific to the gas. With an appropriate selection of the coefficients a_0 to a_3, we can mimic the SNDC which we can see in typical glow discharges. For example, figure 7.11 shows the curve $\upsilon = a_0 + a_1 j + a_2 j^2 + a_3 j^3$ with an approximation $O(j^4) \sim 0$ where $(a_0, a_1, a_2, a_3) = (0, -0.7, 1.2, 1.3)$. The generated nonlinear relation has two positive and one negative slopes.

7.5.6 The dynamic behavior of j and υ

The set of equations is now simplified to

$$\frac{\partial j}{\partial \tau} = D_v \Delta j - (a_1 j + a_2 j^2 + a_3 j^3) + \upsilon \tag{7.13}$$

$$\frac{\partial \upsilon}{\partial \tau} = D_\upsilon \Delta \upsilon - pj - q\upsilon \,. \tag{7.14}$$

The equations 7.10 and 7.11 become a modified form of FitzHugh-Nagumo (FHN) equations (Fitz-Hugh 1961, Nagumo *et al.* 1962) as shown in equations 7.13 and 7.14. They comprise two reaction-diffusion equations with a non-linear term in equation 7.13. The equations, depending on a selection of coefficients, are known to give the dynamics of two variables j and v, behaving as time-independent fluctuation, pulsating, or position-independent fluctuation (Nishiura 2003). The case of time-independent fluctuation is known as Turing instability where pattern formation called a Turing pattern may arise.

For more concrete understanding, linearization of the FHN model is attempted (See Appendix B). Considering linearized equations of 7.13 and 7.14, we get the wavenumber of the instability as

$$k = \left(\frac{f_j g_v - f_v g_j}{D_j D_v} \right)^{1/4} = \left(\frac{a_1 q + p}{D_j D_v} \right)^{1/4} . \tag{7.15}$$

Equation 7.15 indicates interesting aspects of the pattern formation. Since the wavenumber is dependent on D_j, which varies according to the diffusion coefficient of the ions and electrons, the pressure of the gas cannot be independent of the size of the wavelength of the instability. If the gas pressure is enhanced, it decreases the diffusion coefficient D_j, and consequently yields a larger wavenumber. This qualitatively accounts for the dependence of self-organization in CBL discharges on the pressure. For the self-organization at 75 Torr and 150 Torr, we can experimentally confirm, e.g., using figure 6.3, the following data: $k_{75\text{Torr}} = 4\sim7/r = 53 \sim 93$ cm^{-1} and $k_{150\text{Torr}} = 10\sim14/r = 133\sim187$ cm^{-2}, respectively. Indeed, the wavenumber becomes larger when the pressure is raised.

The isocline system of these FHN equations is illustrated in figure 7.11 with a combination of coefficients: (a_0, a_1, a_2, a_3, p, q) = (0, -0.7, -1.2, 1.3, 3, 2) where arrows

denote the direction of shift of the operating point. The direction depends on which region among I to IV in figure 7.11 the operating point currently is located. The sets of coefficients are chosen by the linearization in Appendix B to satisfy stability condition equations B.8 and B.9, but they also satisfy instability condition (a) $S < 0$ in equation B.11. The variables (j,υ) are to be apart from the equilibrium point with diffusion being taking into consideration. The roles of the variables (j,υ) are interpreted as follows: if p and q are positive, any accidental voltage or current deviation generated at the interface can be suppressed, as found in equation 7.14. One finds that the terms including p and q act as a damping system on the plasma with respect to the voltage. If the operating point is on $pj+q\upsilon = 0$, the voltage is not subject to any change. If the diffusion coefficient D_j is sufficiently small compared to D_υ, the component υ rapidly diffuses and is equalized in space prior to diffusion of j. Figure 7.12 is shown to facilitate understanding of such a dynamic behavior of j and υ. In region III in figure 7.11, the production of j is inhibited in the vicinity of the perturbed space A in figure 7.12. The charge multiplication is not active in this space, so the discharge consists of a dark space. On the other hand, j may be increased at the perturbed space B with a smaller concentration of υ because the positive υ accelerates the reproduction of j (region I in figure 7.11). The origin in figure 7.11 is an asymptotically stable point, and small perturbations around the origin are likely to be stabilized by diffusion. However, the qualitative discussion above on the difference of the diffusion coefficients may lead to divergence from the origin. This model mathematically shows a substrate-depleted system in biology (Grey *et al.* 1984), which is known to possibly exhibit a Turing pattern (1954).

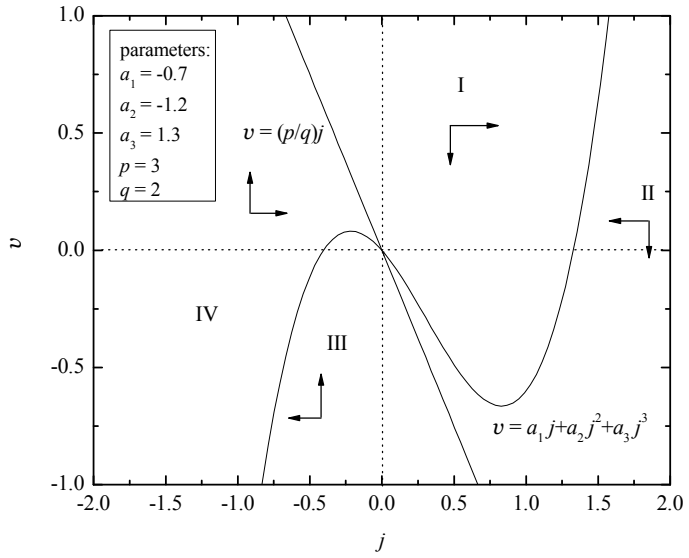

Figure 7.11. Isocline of the equations 7.13 and 7.14 for a set of parameters: (a_0, a_1, a_2, a_3, p, q) = (0, -0.7, -1.2, 1.3, 3, 2). The behavior of the operating point (j, υ) is dependent on which region the current operating point (j, υ) exists among I, II, III, and IV.

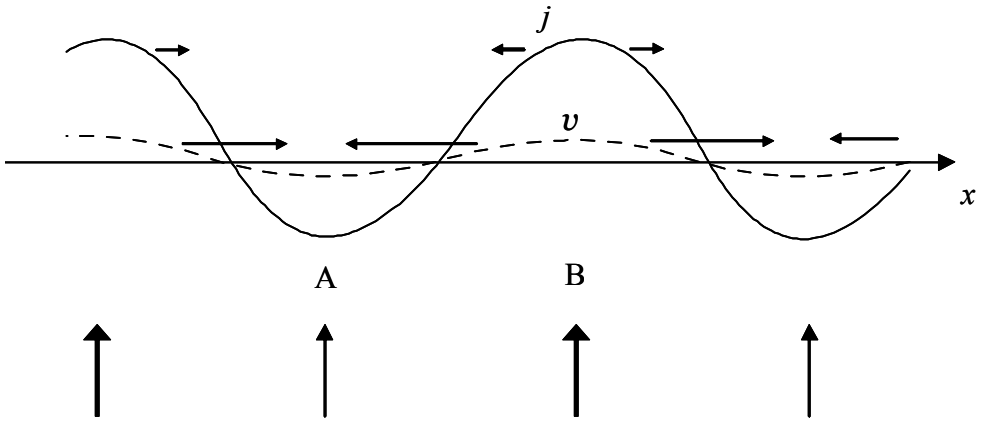

Figure 7.12. An illustration of equilibrium in the negative glow is shown where bi-stable spaces A and B co-exist in a system. The x-coordinate is parallel to the cathode surface. The solid curve represents the density of j and broken curve υ. Horizontal arrows denote directions of diffusion of j and υ. The density of j is depleted in region A while concentrated in B. The amount of supply of charged particles is expressed by boldness of vertical arrows.

7.5.7 Results of numerical calculations

Two-dimensional numerical calculations are executed with the Neumann boundary condition or periodical boundary condition. Using Cartesian coordinates, the calculation area with a length of 10 on the side is divided into 128×128 pixels. Euler's method is used for solving the differential equations. Prior to the calculation, a random perturbation of j and υ with the maximum amplitude of 0.1 is given in each pixel. Therefore, there is no correlation between j and υ before the calculation is performed.

The result of the calculation gives a spotted pattern analogously distributed to the arrangements of self-organization in CBL and parallel-plane geometry. A set of parameters (D_j, D_υ, a_1, a_2, a_3, p, q, dX, $d\tau$, τ_n) = (0.4, 20, -0.7, -1.2, 1.3, 3, 2, 0.3, 0.001, 500000) is set which is determined in section 7.5.6. Turing instability is expected to arise with the wave number $k = \{(f_j g_\upsilon - f_\upsilon g_j)/D_j D_\upsilon\}^{1/4} = 0.67$, i.e., $\lambda = 9.4$. The result of the numerical calculation of equations 7.13 and 7.14 is shown in figure 7.13 where a series of six contour plots indicate the development of spatial distribution of j at (a) $t = 0$ to (f) $t =$ 6.2 ms. In each figure, a pixel with the minimum value of j is colored with black and the maximum with blue. It is readily understood that the morphological equilibrium results in the shape of a "spotted pattern" as shown in figure 7.13(f), which shows analogy with self-organization in CBL discharges. It is known that the branch of the bifurcation from the spotted pattern to "roll patterns" depends on the symmetry of the nonlinear term, $f(j)$ (Arjen Doelman 2004). In the model for CBL discharges, $f(j)$ is not an odd function with the presence of a_2. Provided that $a_2 = 0$, roll patterns would be expected to emerge instead of a spotted pattern.

The above numerical calculation and the discussion must proceed in the real system which is subject to dimensional restrictions. In order for the wavelength of the fluctuation to have the diameter of the filaments, ~100 μm, the elapsed time required to form the Turing pattern of figure 7.13(f) is calculated as follows: we substitute $D_j = 0.4$ into equation A.20, $D_j = t^* D_0 / x^{*2}$ using an appropriate x^*. The relation $x^* = c/(20 \text{ pixels} \times dX) = 8.6$ μm must be needed where $c = 50$ μm is the diameter of the filament. The calculation comes to find $t^* = 1.2\times10^{-5}$ s, which is the infinitesimal time for one iteration of the numerical calculation. As for D_0, the following constants were used: $\mu^+ = 0.4$ cm^2/(V·s) (Varney 1952), $\mu^- = 500$ cm^2/(V·s), $D^+ = 0.03\times\mu^+$ using D^+/μ^+ for Rb^+ in xenon (Tan *et al.* 1995), $D^- = 0.03\times\mu^-$, $n^+ = n^- = 10^{12}$ cm^{-3}. Substituting those figures in equation A.12 gives $D_0 = 2.4\times10^{-6}$ m^2/s. The total transition time, t_{total}, is defined as the time for the formation of the pattern shown in figure 7.13(f), and it is given by $t_{total} = d\tau \times \tau_n \times t^* =$ 6.2 ms. The comparison of the calculated time and the real time to form the filaments has yet to be investigated. Figure 7.14 shows the time evolution of (j,υ) at the center of the simulated area, $(X,Y) = (64, 64)$ and the other two positions, (64, 30) and (64, 100) plotted with the nullcline of the equations 7.13 and 7.14. The information of j in the four plots from figures 7.13(a) to (d) coordinates the intensity of blue at positions (64, 30), (64, 64) and (64, 100) in the figures 7.12 (a) to (f). The final stable points of these positions are marked with dotted circles in figure 7.14 (d). The final equilibrium point is not necessarily located on the nullcline of $\upsilon = f(j)$ or $p\upsilon + qj = 0$ due to the contribution of the diffusion effect. With the three representative positions (64, 30), (64, 64) and (64, 100), we can see that the points do not converge at one point (j^*, υ^*) but distribute with deviations.

Next, a comparison was made for argon pattern formation, obtaining t_{total} = 2.0 ms resulting in the same radius of the filaments as the case with xenon. The following constants were used for the calculation of D_0 for argon: μ^+ = 1.2 $cm^2/(V \cdot s)$, μ^- = 0.84 $cm^2/(V \cdot s)$, $n^+ = n^- = 10^{12}$ cm^{-3}, $D^+/\mu^+ = 0.03$ and $D^- = 0.03 \times \mu^-$ assuming the electrons have the same energy as the case for xenon. The sole use of the result implicitly enables pattern formation in any gas, provided a characteristic time is addressed. The discussion in this paragraph therefore does not state the reason for obtaining self-organization only in xenon. One requires further investigation not only of the characteristic time but also other factors such as the variety of the nonlinearity depending on the gas species.

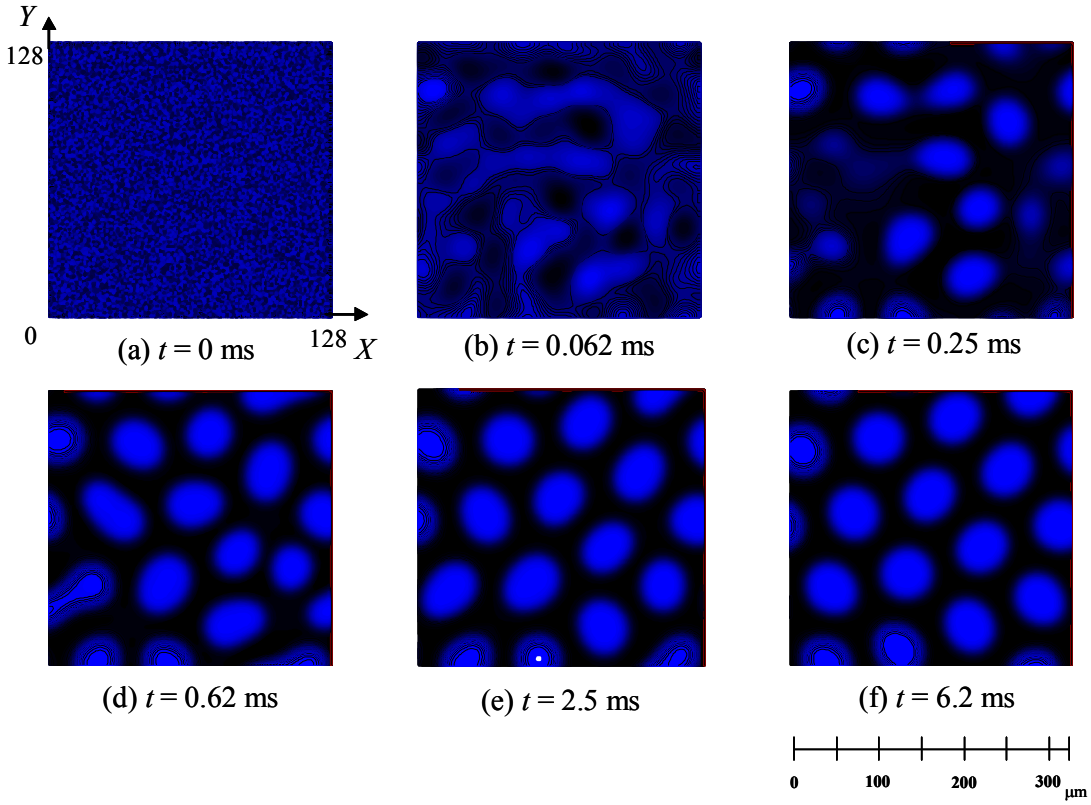

Figure 7.13. The evolution of two-dimensional mapping for j. The parameters are: (D_j, D_v, a_1, a_2, a_3, p, q, dX, $d\tau$) = (0.4, 20, -0.7, -1.2, 1.3, 3, 2, 0.3, 0.001).

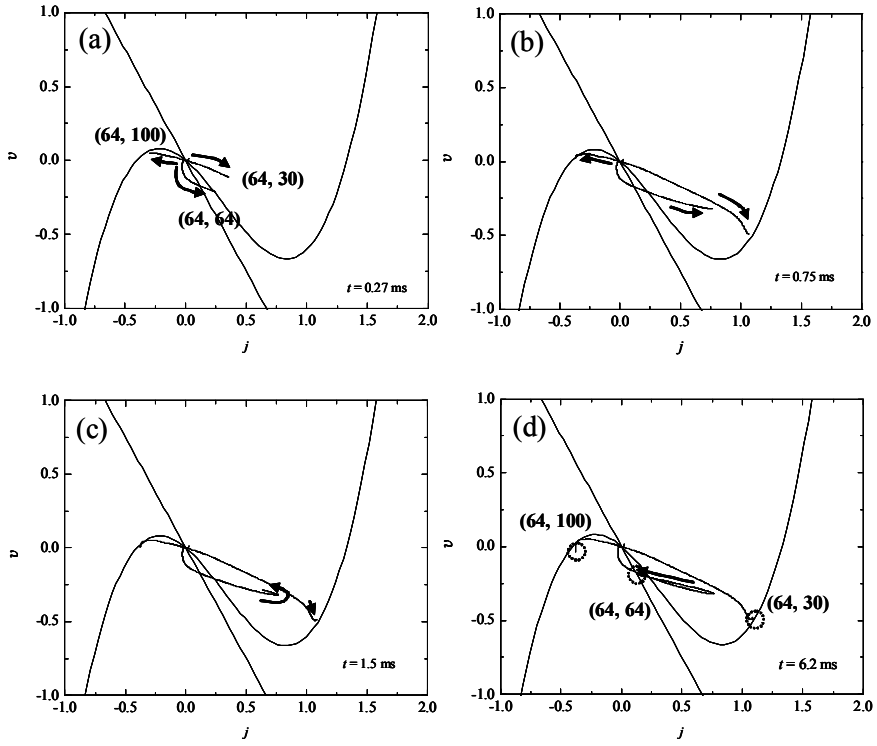

Figure 7.14. Time evolution of (j,υ) at point (64, 30), (64, 64) and (64, 100). The parameters are (D_j, D_υ, a_1, a_2, a_3, p, q, dX, $d\tau$) = (0.4, 20, 0.7, 1.2, -1.3, 3, 2, 0.3, 0.001), and (a) t = 0.27 ms, (b) t = 0.75 ms, (c) t = 1.5 ms, (d) t = 6.2 ms.

7.6 PATTERN FORMATION DUE TO VOLTAGE VARIATIONS EXHIBITING STANDING WAVE

7.6.1 The third model described in the reference by Benilov

Benilov (2007) has established a few major principles that originate from the author's numerical calculations to solve the problem of pattern formation in CBL discharges. The principles are summarized as follows: (a) The basic mechanisms of glow discharges, ionization, drift, diffusion, ionization, and recombination, are, in principle, sufficient for solving solutions that give rise to self-organization. Therefore, heating of the gas leading to an increase in the reduced electric field is, for example, addressed as a particular effect, and it should not be taken into consideration. Electrostatic force determining the position of the filaments is also not required in the model. (b) The presence of self-organization is interpreted as an indication that the j-v curve of the near-cathode region possesses two stable (having positive slopes) sections. The two positive slopes are found in the abnormal glow and a regime where the discharge is not ignited. This necessary characteristic in the model is simply expressed as an S-shaped j-v curve in this thesis.

The author's standpoint, regarding the above two principles, is in accordance with the second mechanism in section 7.5. As far as the author's principle (a) is concerned, the first mechanism adopts a few "particular" effects, e-e collisions, gas heating, and electrostatic force, which Benilov does not consider as essential. Rather, the author indicates that ionization and recombination are the only interactions required in the model. Similarly, the second mechanism employs only basic plasma physics from which Poisson's equation or a continuity equation manifests. As for Benilov's principle (b), the

second mechanism shown in section 7.5 also assumes SNDC in the j-υ curve. However, the nonlinearity is essentially a different matter in the first mechanism, which assumes the relation of the drift velocity of the electrons, w, and the reduced electric field E/N.

Next, the author, starting from continuity equations and Poisson's equation, reaches differential equations for the potential distribution on the near-cathode surface. The major difference of the formulation from that of our second mechanism can be associated with the treatment of the diffusion effect. As seen in one of the author's papers (Benilov 1988), the diffusion is treated as a dissipative factor and combined with the term of recombination. On the other hand, the second mechanism in section 7.5 leaves this effect in the final governing equations as an independent effect. Therefore, the results of those two mechanisms are found to be different with respect to the final form of the equations. The author derives one equation for the stationary potential distribution. The second mechanism, in contrast, deals with two equations to trace dynamics of the relation between j and υ. Comparative pros and cons of these two approaches cannot be understood until the resultant data of the pattern is diagnosed.

In the recent comment by Benilov (2007), the Helmholtz equation (equation 4.9) is presented as the governing equation for the potential distribution in equilibrium. The solutions obey the Bessel function of the first kind of order v (v = 0, 1, 2, …), as

$$\Phi = J_v(kr)\cos v\theta, \qquad k = j'_{v,s} / R \ . \tag{7.16}$$

The author gives two solutions as instances of static pattern formation (figure 4.4). The potential distribution, therefore, features a standing-wave pattern in the cylindrical coordinates.

7.7 ASSESSMENT OF THE THREE MODELS

7.7.1 The first model

Benilov (2007) remarks that this approach is hard to justify from the following viewpoint: a filament represents a collection of ions, electrons and atoms, which are moving rather than quiescent and interact strongly among themselves and with the surrounding gas. The author states that it is thus not possible to treat each filament as a material point with a given electric charge, subject only to an electrostatic force. However, it should be noticed that the positive space charges predominate in the filaments that comprise cathode fall. For a more detailed evaluation, a dynamical approach would be necessary, tracing the kinematics of such particles. A proper description with continuity equations, Maxwell's equations, and kinetic equations, combined with initial and boundary conditions will determine whether the plasma behaves as a material point or not. In order to experimentally support the theory of the Coulombic repulsive force, measurement of the positive ions in the cathode fall would give information about the magnitude of the force exerted between filaments. It is necessary to evaluate the electric field distribution from the cathode to the negative glow to implement the measurement.

This model is based on a number of assumptions as well as the other two mechanisms. The NNDC proposed by the modelers such as Aleksandrov *et al.* is a theoretical prediction without experimental support as far as pure rare gases. A numerical or analytical description of the development of fluctuations needs to be developed further in order to support the theory by Aleksandrov *et al*. The positive feedback effect on the gas heating requires a proof or supporting calculations to give values for the increase in

temperature and ionization rate. The explanation with respect to the Coulombic repulsive force can progress further; the electrically charged region that creates the potential wall needs to be identified and verified by means of numerical calculations or experiments.

Yet, it is still possible to find several aspects in favor of this model. The sequence of physical effects does not contradict any of the observed effects toward self-organization. The used assumptions are straightforwardly deduced from the observed phenomena, which makes it a smooth explanation since there's no leap of logic with respect to the sequence of phenomena, leading to the final state, self-organization. As opposed to the second mechanism, which applies to a phenomenon commonly seen in biology, the first mechanism envisions only basic physical effects ordinarily observed in plasma physics.

7.7.2 The second model

Substantial challenges must be overcome for support of this model. Firstly, self-organization in CBL discharges has a circumference of the dielectric that imposes a different boundary condition from the periodic condition given by the numerical calculation. This effect must be taken into account in future simulations. Secondly, the model assumes that the operating point is located at the negative slope of the j and υ curve, the transition from normal to Townsend discharge; detailed descriptions accounting for such a phenomenon are not thorough. Thirdly, a different gas species such as krypton or argon does not cause pattern formation in experiments; the model does not account for this phenomenon. Nevertheless, it should be stressed that this approach offers a phenomenological success, obtaining pattern formation. The model will possibly connect the reaction-diffusion process more realistically to the claimed self-organization

in such a way that further modifications based on experimental findings may offer clues toward more convincing solutions to these problems.

7.7.3 The third model

One may consider that the solutions Benilov has derived expose a different aspect in terms of the arrangement of filaments, when compared to experimental data shown in chapter 6. Before analyzing the author's solutions, we set up a definition of the nomenclature of filament arrangements. In the following we call the description "(N_1, N_2, N_3, …)" the configuration in which N_i of filaments occupy the i^{th} shell from the center. For example, the configuration in figure 6.3(r) is denoted by (1, 6, 13). In general, any configuration in CBL and parallel-plate geometry with a multi-shell structure adheres to a relationship: $N_1 < N_2 < N_3$… i.e., the number of filaments of an arbitrary inner shell is smaller than that of the outer shells. The solution Benilov gives, however, merely offers shell configurations of (N, N, N …) where the number of antinodes in the same phase at any shell remains the same as other shells. For example, the case of figure 4.6(b) has a structure of (8, 8, 8, 8, 8, 8, 8). Exceptions are not allowed since the solution must fulfill equation 7.16. In the case of a single-shell structure, the pattern obtained from the Helmholtz equation conceivably offers a solution. The solution displays an analogous arrangement with (N) structures (cf. $N = 5$ for figure 4.6(a)). So far, no explanation has been given to identify the reason for the deviation in the multi-shell structures, but this discrepancy must be considered for assessment of the applicability of this approach.

7.8 FUTURE APPLICATIONS OF THE SELF-ORGANIZATION IN CBL DISCHARGES

The CBL discharges, due to the positive characteristic in the *I-V* curve, can produce uniform excimer radiation when integrated with a common anode (Zhu *et al.* 2007). Self-organized patterning is observed in the positive slope of the *I-V* curve. This fact and the characteristics of self-organization observed in this thesis possibly enable versatile applications of the self-organization in the CBL discharges: (a) With the high excimer power density, a novel type of flat panel VUV light source is promising. (b) The self-organization in the CBL discharges is also reactive. Non-equilibrium kinetic processes – if position and size of filaments are more controllable – offer a possibility of maskless chemical processes such as position-selective etching. (c) two-dimensional integration of self-organized CBL discharges may explore an innovative opportunity in photonics applications. The experimental study by Sakai *et al.* (2007) demonstrated microplasma arrays exhibiting characteristics of a photonic crystal such as unidirectional and diverted propagation of millimeter-waves near the plasma frequency. This result showed the feasibility of controlled propagation of electromagnetic waves by use of microplasmas. By operating arrays of self-organization with the flexibility of periodical gaps, changing the current and the pressure, we can expect an effect on the transmission of electromagnetic waves within a range of certain wavelengths depending on the periodical gap.

CHAPTER VIII

SUMMARY

Cathode boundary layer (CBL) discharges are operated in a reactor configuration consisting of a planar cathode and a ring-shaped anode separated by a thin dielectric layer. This geometry offers a discharge structure without a positive column. Since self-organization of CBL discharges in xenon has been discovered, it has been investigated from the physical point of view. The major purpose of this study has been to expand understanding of the behavior of the self-organization with experimental and theoretical approaches.

Comprehensive diagnostics have been performed to investigate the behavior of those filaments by use of optical, electrical, spectral and temperature measurement. The optical observations in xenon discharges showed that, with current reduced to 0.2 mA at 75 Torr, the discharge changes from an abnormal glow discharge, first to a normal glow discharge with a reduced plasma diameter and then to a filamentary discharge which is characterized by stationary, self-organized (diffuse) patterns. The marginal current density is calculated to be ~50 mA/cm^2. With a further reduction in current, these diffused filaments become well-defined (confined) filaments. The side-on observation found that the axial dimensions of the filaments are determined by the length of the cathode fall (< 70 μm for xenon discharges at 75 Torr). The visible structure of such filaments, determined by the side-on optical measurement of the negative glow, is disk-shaped with a diameter of ~80 μm. The side-on observations have also allowed us to measure the cathode fall length which is dependent on the pressure and current. This information enables the determination of the secondary emission coefficient, γ, by

knowing the current density and the cathode fall voltage. For discharges in xenon with a tungsten cathode, γ. was determined to be 0.03, and the value of γ may be subject to a temperature effect, a change in the number density of neutral xenon atoms. γ is estimated to increase when operated at an elevated current and pressure. The value of γ may be varied due to the gas temperature as described above but not by the cathode temperature. The temperature measurement at the cathode surface has shown that the thermal electron emission from the cathode surface due to the change of cathode temperature is negligible. The cathode fall voltage, under normal glow conditions in xenon discharges at 75 Torr, was found to be 320 V, and decreases when the discharge transforms itself into a self-organized mode. Electrical measurements of the CBL discharges recorded a discrete change in the total current when the self-organization is exhibited in the confined mode. The spectral measurement provides scaling information about the relative population of high-lying states ($1s_4$, $1s_5$, and $2p_6$) of xenon atoms. The rate constant for Xe^* is likely to be optimized when reaching normal glow from abnormal glow.

The gas species, the cathode material, and the reactor geometry affect the behavior of the xenon discharges and the self-organization. Krypton was employed in place of xenon, resulting in rather homogeneous plasma without any appreciable change in pattern. Purity of xenon is crucial for self-organization. In no xenon gas, with a purity less than 99.99 %, can the self-organization exist. Of the tested aluminum, copper, and tungsten cathodes, the aluminum cathode achieved a higher excimer intensity at 250 Torr than any other cathode material. When the diameter of the plasma reactor is reduced to 300 μm, it gives rise to a single filament, illuminating with an enhanced excimer power density of 500 mW/cm^2 at 62 Torr. The experiment using the closed anode geometry

elucidated that the radial electric field on the anode plain decreased to near zero in contrast to the case in CBL geometry. From the fact that both types of geometry yield analogous self-organization, it is concluded that the radial electric field in the CBL discharges does not affect the pattern formation.

CBL xenon discharges yield strong excimer emission: the power density reaches 1700 mW/cm^2 and the internal efficiency recorded 6% at an optimized condition of pressure, 250 Torr. A change in the diameter of the anode opening can enhance the performance of the emission. Reducing the current and the diameter of the plasma reactor to 300 μm, the emission resulted in a reduced number of filaments with an increase in excimer power density, e.g., 700 mW/cm^2, by a factor of more than two at 75 Torr compared to 300 mW/cm^2 (D = 750 μm). Therefore, further decrease in the dimension of the plasma reactor is expected to provide a higher power density. The efficiency showed a monotonic decreasing function of the current, with a maximum value of 6.0 % at 250 Torr for D = 750 μm. It is essential that the current-voltage characteristic in the self-organization mode has a positive slope, indicating that parallel operation of intense micro excimer sources is feasible using self-organization. This has been experimentally demonstrated by Zhu *et al.* (2007).

An interpretation was qualitatively given as to the dependence of excimer intensity on the current; the excimer radiation decreases as the current is increased. From the spectroscopic experiments in the visible and infrared, it has been found that the population of excited states is not increased near normal glow or self-organized mode. A perspective is therefore given based on the result: the dependency is attributed to the variable rate constants for $Xe^*(1s_4$ and $1s_5)$, which are the precursors of excimers. As the

simulation by Carman *et al.* indicated, a range of low electron energies optimizes production of Xe^* in terms of rate constants when the plasma is in abnormal glow near normal glow. The excimer formation is accelerated near the normal glow as a result. Determination of such production rates of Xe^* is necessary to enhance the understanding of excimer production. Since this phenomenon is also observed with the use of argon, this is not likely to be relevant to self-organization.

The axial electric field is likely to induce N-shaped NDC in the *w*-*E* phase in the negative glow or Faraday dark space, due to their weak electric field. Electron-electron collisions are likely to cause a change in the frequency of momentum transfer to neutral particles, generating the NDC effect. A positive feedback of the current density and the electric field develops the fluctuation in the region where NNDC manifests. When the current is decreased toward the confined mode, the magnitude of the ionization in the filaments is enhanced due to local gas heating, resulting in growth of the first Townsend coefficient. This insight is supported by our experimental observation of a drastic increase in the current density in each filament. The organized filaments can be explained as Coulomb forces acting on the individual filament placed in a virtual potential well created by positive electric charges. The Coulomb forces are due to the positive space charges in the cathode fall of the filaments confined in a potential well defined by positive charges distributed along the circular dielectric spacer. A model, based on this assumption, was assessed by a computational calculation, and the result yielded a positioning of the filaments similar to those observed experimentally.

The second mechanism for the pattern formation is discussed. It notes the interaction of α and E, whose relation is subsequently converted into the relation of

variation of the local current density, j, and the voltage, v, at the interface between a hypothesized nonlinear and linear layer. The dynamics of the two variables, j and v, showed a system described as reaction-diffusion process where two variables inhibit or activate each other while diffusing. The dynamic numerical calculation was carried out, and the result yielded a development of 2-D patterning which consists of spotted domains equally spaced from each other. In the case of CBL discharges, the transition time of t = 6.2 ms is required for the formation of the pattern with a typical filament diameter of 50 μm.

The third model theoretically proposed by Benilov regarding self-organization in CBL discharges bases its principles on an S-shaped nonlinear relation of the current density to the voltage, which is similar to the assumption made in the second mechanism. By abbreviating the diffusion effect of charged particles in a term linear to the population and describing the governing equations with respect to the voltage, the author obtained a Helmholtz equation which rules the spatial distribution of the voltage in the negative glow. The solution of the equation gives a Bessel function of the first kind, resulting in axisymmetric arrangements of domains similar to the self-organization in CBL discharges. The voltage distribution parallel to the cathode surface exhibits a profile of a standing wave in the cylindrical coordinates. However, the solution requires the same number of nodes in each shell of the pattern structure. This requirement does not fulfill the experimental result of most of the multi-shelled self-organizations in CBL discharges.

BIBLIOGRAPHY

Adler D A, Shur M S, Silver M and Ovshinsky S R 1980 *J. Appl. Phys.* **51**, 3289.

Aleksandrov N L, Dyatko N A, Kochetov I V, Napartovich A P and Lo D 1996 *Phys. Rev. E.* **53**, 2730.

Aleksandrov N L, Kochetov I V, Lo D and Napartovich A P 1997 *J. Phys. D: Appl. Phys.* **30**, 2217.

Becker K, Koutsospyros A, Yin S –M, Christodoulatos C, Abramzon N, Joaquin J C and Brelles-Marino G 2005 *Plasma. Phys. Control. Fusion* **47**, B513.

Becker K, Schoenbach K H and Eden J G 2006 *J. Phys. D: Appl. Phys.* **39**, R55.

Benilov M S 2007 *Plasma Sources Sci. Technol.* **16**, 422.

Benilov M S 1988 *Sov. Phys. – Tech. Phys.* **33**, 1267.

Benilov M S 2006 Presentation at the *2006 IEEE Int. Conf. Plasma Science* (Traverse City, MI).

Benilov M S 2007 *J. Phys. D: Appl. Phys.* **40**, 1376.

Bonifield T D, Rambow F H K, Walters G K, McCusker M V, Lorents D C and Gutcheck R A 1980 *J. Chem. Phys.* **72**, 2914.

Bouef J P and Kunhardt E E 1986 *J. Appl. Phys.* **60**, 915.

Carman R J and Mildren R P 2003 *J. Phys. D: Appl. Phys.* **36**, 19.

Chiflikyan R V 2000 *Phys. plasmas* **7**, 2704.

Cobine J D 1958 *Gaseous Conductors: Theory and Engineering Applications* (New York: Dover).

Eckstrom D J, Nakano H H, Lorents D C, Rothem T, Betts J A, Lainhart M E, Dakin D A and Maenchen J E 1988 *J. Appl. Phys.* **64**, 1679.

El-Habachi A and Schoenbach K H 1997 *Appl. Phys. Lett.* **72**, 22.

Fitz-Hugh R 1961 *Biophys. J.* **1**, 445.

Frame J and Eden J G 1998 *Electronics Letters* **34**, 1529.

Francis G 1956 *Handbuch der Physik* ed S Flügge **22** (Berlin: Springer-Verlag) (in Germany).

Golubovskii Yu B, Maiorov V A, Kozakov R V, Solyman S, Stockhausen G and Wilke C 2001 *J. Phys. D: Appl. Phys.* **34**, 1963.

Grey P and Scott S K 1984 *Chem. Eng. Sci.* **39**, 1087.

Gurevich E L, Astrov Y A and Purwins H-G 2005 *J. Phys. D: Appl. Phys.* **38**, 468.

Haas R A 1973 *Phys. Rev. A* **8**, 1017.

Haddad G N 1983 *Aust. J. Phys.* **36**, 297.

Hagstrum H D 1956 *Phys. Rev.* **104**, 1516.

Hornbeck J A 1951 *Phys. Rev.* **83**, 374.

Hsu D D and Graves D B 2003 *J. Phys. D: Appl. Phys.* **36**, 2898.

Huxley L G H Crompton R W 1974 *The diffusion and drift of electrons in gases* (New York: Wiley).

Kaufmann W A 1900 *d. Physik* **2**, 158.

Kleban P and Davis H T 1977 *Phys. Rev. Lett.* **39**, 456.

Kochetov I V, Napartvich A P, Ye C and Lo D 1998 *J. Appl. Phys.* **84**, 1863.

Kolobov V I and Fiala A 1994 *Phys. Rev. E* **50**, 3018.

Kolobov V I 2006 *J. Phys. D: Appl. Phys.* **39**, R487.

Korolev Y D, Rabotkin V G and Filonov A G 1979 *Teplofiz. Vysokikh Temper.* **17**(1), 211.

Korolev Y D, Mesyats G A, 1998 Physics of pulsed breakdown in gases (Yekaterinburg: URO-PRESS).

Kunhardt E E and Becker K 1999 US Patent 5872426, and subsequent patents 6005349, and 6147452, 6879103, and 6900592.

Kushner M J 2005 *J. Phys. D: Appl. Phys.* **38**, 1633.

Lieberman M A and Lichtenberg A J 1994 Principles of plasma discharges and materials processing (New York: John Wiley and Sons, Inc).

Long W H Jr, Bailey W F and A Garscadden 1976 *Phys. Rev. A* **13**, 471.

Lopantseva G B, Pal' A F, Persiantsev I G, Polushkin V M, Starostin A N, Timofeev M A and Treneva E G 1979 *Fiz. Plazmy* **5**, 1370.

Lozansky E D and Firsov O B 1975 *Theory of the spark* (Moscow: Atomizdat).

Moselhy M 2003 *Pulsed operation of microhollow cathode discharges* (*dissertation*) (*Old Dominion University*).

Moselhy M and Schoenbach K H 2004 *J. Appl. Phys.* **95**, 1642.

Moselhy M, Stark R H, Schoenbach K H and Kogelschatz U 2001 *Appl. Phys. Lett.* **78**, 880.

Muller I, Punset C, Ammelt E, Purwins H –G and Bouef J P 1999 *IEEE trans. Plasma Sci.* **27**, 20.

Nagumo J S, Arimoto S and Yoshizawa S 1962 *Proc. IRE* **50**, 2061.

Nasuno S 2003 *Chaos* **13**, 1010.

Nigham W L and Wiegand W J 1974 *Phys. Rev. A* **10**, 922.

Nishiura Y 2003 *Pattern Dynamics of self-reproduction and self-destruction* (Tokyo: Iwanami) (In Japanese).

Pack J L and Phelps A V 1961 *Phys. Rev.* **121**, 798.

Radehaus C, Willebrand H, Dohmen R, Niedernostheide F -J, Bengel G and Purwins H – G 1992 *Phys. Rev. A* **45**, 2546.

Radehaus C, Dohmen R, Willebrand H and Niedernostheide F -J 1990 *Phys. Rev. A* **42**, 7426.

Radehaus C, Kardell K, Baumann H, Jager D and Purwins H -G 1987 *Z. Phys. B* **65**, 515.

Raizer Y P 1991 *Gas Discharge Physics* (Berlin: Springer).

Robertson A G 1977 *Aust. J. Phys.* **30**, 39.

Roth J R 1995 *Industrial plasma engineering: Principles* (Philadelphia: Institute of Physics Publishing).

Sakai O, Sakaguchi T and Tachibana K 2007 *Contrib. Plasma Phys.* **47**, 96.

Schoenbach K H, Moselhy M and Shi W 2004 *Plasma Sources Sci. Technol.* **13**, 177.

Shaw M P, Mitin V V, Scholl E and Grubin H L 1992 *The physics of Instabilities in Solid State Electron Devices* (New York and London: Plenum Press).

Shaw M P, Grubin H L and Solomon P R 1979 *The Gunn-Hilsum Effect* (New York: Academic Press).

Shi W and Schoenbach K H 1999 *IEEE Trans. Plasma Sci.* **27**, 16.

Shintani Y, Ahn J-C, Tachibana K, Sakai T and Kosugi N 2003 *J. Phys. D: Appl. Phys.* **36**, 2928.

Shirafuji T, Kitagawa T, Wakai T and Tachibana K 2003 *Appl. Phys. Lett.* **83**, 2309.

Strümpel C, Purwins H-G and Astrov Yu A 2001 *Phys. Rev. E* **63**, 026409-1.

Sugawara T and Kaneko K 2005 *Nonlinear Sci. nlin.* PS/0503034.

Tachibana K, Shojun F and Sakai T 2000 *J. Appl. Phys.* **88**, 4967.

Takano N and Schoenbach K H 2006 *Plasma Sources Sci. Technol.* **15**, S109.

Ushio AMERICA, Inc. www.ushio.com/files/CiMAX200.pdf.

Varney R N 1952 *Phys. Rev.* **88**, 362.

v Engel A and Steenbeck M 1934 *Elektrische Gasentladungen, ihre Physik u. Technik* Vol. 2 pp 72 (in Germany).

v Engel A 1924 *Ionized Gases* (New York: Plenum Press).

Wehrli M 1928 *Helv. Phys. Acta*. **1**, 323.

Wieme W and Lenaerts J 1981 *J. Chem. Phys.* **74**, 483.

Zhu W, Takano N, Schoenbach K H, Guru D, McLaren J, Heberlein J, May R and Cooper J R 2007 *J. Phys. D: Appl. Phys.* **40**, 3896.

APPENDIX A. CALCULATIONS OF REACTION DIFFUSION EQUATIONS FOR THE SECOND MECHANISM

Radehaus *et al.* (1990) have modeled kinetics at the interface between a resistive layer and a nonlinear plasma layer where two kinds of charge carriers play a principal role (see figure 4.3b). Equations for variations of the current density and the voltage at the interface between the resistive and the nonlinear layer are derived from continuity equations and Poisson's equation. The governing equations start with

$$\frac{\partial n^-}{\partial t} = R(n^-, n^+, |E|) + (1/e)\nabla_{xz} \cdot j^-, \tag{A.1}$$

$$\frac{\partial n^+}{\partial t} = R(n^-, n^+, |E|) - (1/e)\nabla_{xz} \cdot j^+, \tag{A.2}$$

$$\nabla_{xz} \cdot E = (e/\varepsilon\varepsilon_0)(n^+ - n^-) \tag{A.3}$$

where ε is the relative dielectric constant, R is the reaction term including ionization and recombination, e is the elementary charge. The current densities obey the following equations

$$j^- = en^-\mu^- E + eD^-\nabla_{xz} n^-, \tag{A.4}$$

$$j^+ = en^+\mu^+ E - eD^+\nabla_{xz} n^+ \tag{A.5}$$

with μ^+ and μ^- designating mobilities of the ion and electron, D^+ and D^- diffusion coefficients of the ion and electron, respectively. In order to find the local current density j_z, which is directed in the z direction in the nonlinear layer, we take z components of A.4 and A.5 and obtain

$$j_z = j_z^- + j_z^+ = -e(n_0^- + n_1)(v_{0z}^- + v_{1z}^-) + e(n_0^+ + n_1)(v_{0z}^+ + v_{1z}^+) \tag{A.6}$$

where n_0^- and n_0^+ denote the constant component of the number density of electrons and ions, respectively, and for the variation component, $n_1 = n_1^- = n_1^+$ is met due to quasineutrality. Similarly, v_0^- and v_0^+ represent the constant component of the velocity, and v_1^- and v_1^+ the deviation. The z component j_z is expanded as

$$j_z = -e(n_0^- v_{0z}^- + n_0^- v_{1z}^- + n_1 v_{0z}^- + n_1 v_{1z}^- - n_0^+ v_{0z}^+ - n_0^+ v_{1z}^+ - n_1 v_{0z}^+ - n_1 v_{1z}^+) . \tag{A.7}$$

With $v_z^+ = \mu^+ E_z = \alpha\mu^- E_z = -\alpha v_z^-$ we get

$$\begin{aligned} j_z &= -e(n_0^- v_{0z}^- + n_0^- v_{1z}^- + n_1 v_{0z}^- + n_1 v_{1z}^- + \alpha n_0^+ v_{0z}^- + \alpha n_0^+ v_{1z}^- + \alpha n_1 v_{0z}^- + \alpha n_1 v_{1z}^-) \\ &= j_0 + j_{01} + j_{10} + j_2 \\ &= j_0 + j_{Nz} \end{aligned} \tag{A.8}$$

where

$$j_0 = -e(n_0^- + \alpha n_0^+) v_{0z}^-$$

$$j_{01} = -e(n_0^- + \alpha n_0^+) v_{1z}^-$$

$$j_{10} = -e(1+\alpha) n_1 v_{0z}^-$$

$$j_2 = -e(1+\alpha) n_1 v_{1z}^-$$

$$j_{Nz} = j_{01} + j_{10} + j_2 . \tag{A.9}$$

The variation of the current density in the nonlinear layer can be represented by j_{10} which has the largest amplitude.

The evolution of variation of the current density, j_{10}, is expressed by

$$\frac{\partial j_{10}}{\partial t} = D_0 \Delta j_{10} - \mu_0 j_{10} \frac{\partial U}{\partial x} + g_0(j_{10}, U) \tag{A.10}$$

where U is the variation of the potential from a normal value U_0, g_0 is the reaction term determined by j_{10} and U. μ_0 is the mean value of modified mobility as

$$\mu_0 = \frac{\mu_x^+ \mu_x^- (n_0^+ - n_0^-)}{\mu_x^+ n_0^+ + \mu_x^- n_0^-}, \tag{A.11}$$

and D_0 the modified diffusion coefficient:

$$D_0 = \frac{\mu_x^+ D_x^- n_0^+ + D_x^+ \mu_x^- n_0^-}{\mu_x^+ n_0^+ + \mu_x^- n_0^-}. \tag{A.12}$$

As for the variation of the voltage U, an approximation is assumed where the distribution of the potential is linear in the nonlinear layer, and obeys Laplace's equation in the linear layer (Radehaus *et al.* 1987). The equation, as for the continuity of the current density at the interface, takes the form

$$\left(\varepsilon_0 \varepsilon_L \frac{\partial}{\partial t} + \frac{1}{\rho}\right) E_{Lz}(x,0,t) = j_{Nz} + \varepsilon_0 \varepsilon_N \frac{\partial E_{Nz}(x,0,t)}{\partial t} \tag{A.13}$$

with the second term in the right hand side denoting the displacement of the current. E_{Lz} is the electric field in the z direction in the linear layer, and the E_{Nz} in the nonlinear layer. ρ is the conductance of the linear layer. ε_{L} and ε_{N} denote the relative permittivity in linear and nonlinear medium, respectively. Using an approximation $E_{\mathrm{Nz}}=U(x)/a$ where a is the thickness of the nonlinear layer, we get the following expression:

$$\left(\varepsilon_0 \varepsilon_L \frac{\partial}{\partial t} + \frac{1}{\rho}\right)\left(\frac{U_v - U}{b} + c\frac{\partial^2 U}{\partial x^2}\right) = \frac{a_0 U}{a} + j_{10} + j_{10}\frac{U}{U_0} + \frac{\varepsilon_0 \varepsilon_N}{a}\frac{\partial U}{\partial t}. \tag{A.14}$$

The variations of current and voltage are scaled as $v = j_{10}/j_{10}^*$ and $w = -U/U^*$, respectively, and the equations A.6 and A.10 write in an autonomous form

$$\frac{\partial v}{\partial \tau} = \sigma \Delta v + \mu(\nabla v)(\nabla w) + f(v) - w \tag{A.15}$$

$$\delta \frac{\partial w}{\partial \tau} = \Delta w + v(1 + \vartheta w) + -w - \kappa + \frac{r}{1+r}\frac{1}{\chi l'}\int_0^{l'} w(\xi')d\xi' \tag{A.16}$$

with the definitions of the coefficients shown as $w = -U/U^*$, $v = j_{10}/j^*$,

$\tau = (\rho b)/(\chi l t)$, $\xi = x/d_\omega^{1/2}$, $j^*/U^* = \chi/(\rho b)$, $\chi = 1 + (\rho a_0 b)/a$, $\vartheta = -U_*/U_0$,

$\sigma = d_v/d_w$, $\delta = \dfrac{\varepsilon_0 \varepsilon_N b^2 \rho^2}{a \chi^2 l}$, $d_v = \dfrac{D_0 \chi \ell}{\rho b}$, $\kappa = \dfrac{U_s}{(1+r)\chi U^*}$, $r = \dfrac{R_s l}{\rho b}$, $f(v) = \dfrac{-h(j^* v)}{U^*}$,

$$\mu = \frac{26 \mu_0 \ell \chi^2 U^*}{5 \rho b^3}. \tag{A.17}$$

Defining $T = \kappa - \dfrac{r}{1+r}\dfrac{1}{\chi l'}\int_0^{l'} w(\xi')d\xi'$ and setting μ = 0 for simplicity, the final form of equations 4.3 and 4.4 are obtained. In section 7.5, we have utilized equations A.6 and A.10 and developed them into the following equations:

$$\frac{\partial j}{\partial \tau} = D_j \Delta j + \mu(\nabla j)(\nabla \upsilon) + \upsilon - f(j) \tag{A.18}$$

$$\frac{\partial \upsilon}{\partial \tau} = D_\upsilon \Delta \upsilon - pj - q\upsilon - \theta j \upsilon + sU_s/U^* + s\frac{x^* r}{l}\int_o^{l'} \upsilon d\xi' \tag{A.19}$$

with the coefficients and variables defined as $j = j_{10}/j^*$, $\upsilon = U/U^*$, $\dfrac{t^* U^*}{l j^*} = 1$,

$D_\upsilon = \dfrac{5bat^*}{26 x^{*2} \rho \varepsilon_0 \varepsilon_N}$, $p = \dfrac{aj^* t^*}{\varepsilon_0 \varepsilon_N U^*}$, $q = \dfrac{at^*}{\varepsilon_0 \varepsilon_N}\left(\dfrac{1}{\rho b} + \dfrac{a_0}{a}\right)$, $s = \dfrac{at^*}{(1+r)\rho b \varepsilon_0 \varepsilon_N}$, $D_j = \dfrac{t^* D_0}{x^{*2}}$,

$\mu = \mu_0 \dfrac{U^* t^*}{d'}$, $r = \dfrac{R_s l}{\rho b}$, $f(\upsilon) = \dfrac{-h(j^* j)}{U^*}$, $\theta = \dfrac{aj^* t^*}{U_0 \varepsilon_0 \varepsilon_N}$, $l' = \dfrac{l}{x^*}$, $X = \dfrac{x}{x^*}$, $\Delta = \dfrac{\partial^2}{\partial X^2}$,

$$\nabla = \frac{\partial}{\partial X}. \tag{A.20}$$

The approximations $\mu = \theta = 0$ would be appropriate because these terms consist of a product of two derivatives. Assuming that the operating point (I_0, U_0) is fixed, satisfying

$U_s = U_0$-$I_0 R_s$, the two terms $sU_s / U^* + s\frac{x^* r}{l}\int_o^{l'} \upsilon d\xi'$ can be neglected. Thus we reach the final form,

$$\frac{\partial j}{\partial \tau} = D_j \Delta j + \upsilon - f(j) \tag{A.21}$$

$$\frac{\partial \upsilon}{\partial \tau} = D_\upsilon \Delta \upsilon - pj - q\upsilon . \tag{A.22}$$

APPENDIX B. LINEARIZATION ANALYSIS OF THE REACTION-DIFFUSION EQUATIONS FOR THE SECOND MECHANISM

For more concrete understanding, linearization of the FHN model is attempted. Consider linearized equations of 7.13 and 7.14:

$$\dot{\mathbf{u}} = A\Delta\mathbf{u} + R\mathbf{u} \tag{B.1}$$

where

$$\mathbf{u} = [j, \upsilon]^T,\ A = \begin{bmatrix} D_j & 0 \\ 0 & D_\upsilon \end{bmatrix} \text{ and } R = \begin{bmatrix} f_j & f_\upsilon \\ g_j & g_\upsilon \end{bmatrix} = \begin{bmatrix} -a_1 & 1 \\ -p & -q \end{bmatrix}.$$

In order to provide insight into the spatiotemporal development of instability with a growth rate λ and the wave number k, the vector $\mathbf{u}$ is assumed to have the form:

$$\mathbf{u} = [j, \upsilon]^T = [j_0, \upsilon_0]^T \exp(\lambda t + i\mathbf{k}\cdot\mathbf{r}). \tag{B.2}$$

Substituting this into equation B.1, we get

$$\begin{bmatrix} \lambda j \\ \lambda \upsilon \end{bmatrix} = \begin{bmatrix} f_j - D_j k^2 & f_j \\ g_j & g_\upsilon - D_\upsilon k^2 \end{bmatrix} \begin{bmatrix} j \\ \upsilon \end{bmatrix} \equiv B\mathbf{u}. \tag{B.3}$$

We can obtain non-trivial solutions for λ when the determinant of matrix B is zero, that is

$$\lambda^2 - T\lambda + S = 0,$$

where

$$T = T(k^2) = f_j + g_\upsilon - k^2(D_j + D_\upsilon) \tag{B.4}$$

$$S = S(k^2) = f_j g_\upsilon - f_\upsilon g_j - k^2(D_\upsilon f_j + D_j g_\upsilon) + k^4 D_j D_\upsilon. \tag{B.5}$$

i) In the case with diffusion neglected (D_j = D_υ = 0), the quadratic equation for λ is simplified to

$$\lambda^2 - (f_j + g_v)\lambda + (f_j g_v - f_v g_j) = 0\,. \tag{B.6}$$

Solving this equation,

$$\lambda = \frac{(f_j + g_v) \pm \sqrt{(f_j + g_v)^2 - 4\left(f_j g_v - f_v g_j\right)}}{2}. \tag{B.7}$$

If $f_j + g_v > 0$, an instability is driven. In order for the system to be stable, $f_j + g_v < 0$ is a necessary condition, and $f_j g_v - f_v g_j > 0$ is also required. Consequently, the stability conditions are summarized as

$$f_j + g_v = -a_1 - q < 0, \tag{B.8}$$

$$f_j g_v - f_v g_j = a_1 q + p > 0. \tag{B.9}$$

ii) Taking into consideration the case with diffusion coefficients, diffusion may drive the system away from equilibrium even if the stability condition B.8 and B.9 are fulfilled. Consider the case $f_j + g_v < 0$ and $f_j g_v - f_v g_j > 0$ where stability conditions are met for a non-diffusional system described above in i). Equation B.7 can be expressed as

$$\lambda = \frac{T \pm \sqrt{T^2 - 4S}}{2}, \tag{B.10}$$

where $T = f_j + g_v - k^2(D_j + D_v) < 0$. The growth rate λ may be a positive number depending on the value of S. The behavior of the growth rate is classified into the following three cases:

(a) $S \le 0$ ($\lambda_1 \ge 0$, $\lambda_2 \le 0$)

(b) $0 < S < T/2$ ($\lambda_1 < 0$, $\lambda_2 < 0$) (B.11)

(c) $T/2 \le S$ (λ_1, $\lambda_2 = R$ +- iC where $R \le 0$).

Case (a) has an eigenvalue with a positive sign, so instability can develop. At the onset of the instability, $dS/\mathrm{d}h = 0$ is satisfied where $h = k^2$. Solving these equations gives the wave number of the instability as

$$k = \left(\frac{f_j g_v - f_v g_j}{D_j D_v} \right)^{1/4} . \tag{B.12}$$

VITA

Nobuhiko Takano

Education:

Doctor of Philosophy (Electrical Engineering), Old Dominion University, Norfolk, Virginia December 2007

Master of Science (Material Science and Engineering), Kyoto University, Kyoto, Japan, March 2002

Bachelor of Science (Electrical and Electronic Engineering), Kyoto University, Kyoto, Japan, March 2000